Localisation, Hall Effect and Electron-Phonon Decoupling in GaAs and Graphene

Edward Robert Carroll

Thesis submitted for the degree of

Doctor of Philosophy

Department of Electronic and Electrical Engineering

University College London

June 2025

Declaration

I, Edward Robert Carroll, confirm that the work presented in this thesis is my own. Where information has been derived from other sources, I confirm that this has been indicated.

Abstract

In the context of electron transport in two-dimensional disordered systems, an Arrhenius Hall carrier density has never been observed alongside an Arrhenius conductivity when the Fermi level is below a mobility edge. An Arrhenius quantity decreases exponentially with inverse temperature. For over half a century, it is the Hall mobility that has been consistently reported as being activated as opposed to the Hall carrier density. This has historically been a significant issue with respect to claiming transport via activation to a mobility edge. In this work, for the first time, an Arrhenius Hall carrier density and an Arrhenius conductivity have been observed together. The system used is a two-dimensional electron gas hosted in a gated GaAs/$Al_{0.33}Ga_{0.67}As$ heterostructure. Furthermore, the Hall mobility is shown to be independent of Fermi level. This itself is striking and strong evidence of transport via activation to a mobility edge. A transition between carrier density and mobility dominating the conductivity temperature dependence has also been observed in this work. This could explain the historical results in the literature. Additionally, transport within disorder broadened Landau levels has been investigated. The breakdown of the quantum Hall effect is shown to agree well with a phenomenological electron overheating model and is subsequently ascribed to electron-phonon decoupling. This decoupling manifests itself as large, hysteretic current jumps in current-voltage characteristics. The overheating model has previously been applied to transport in disordered thin

films. The work presented in this thesis is the first in which it has been successfully applied to the breakdown of the quantum Hall effect. Finally, an unusual low temperature Arrhenius resistivity regime has been observed in helium focused ion beam damaged graphene. It is suggested that current theories in the literature cannot explain the behaviour.

Impact Statement

There has been a significant renewal of interest in the field of localisation in recent years. This, in the main, has centred around the concept of many-body localisation. This exotic state of matter, as yet unobserved in an electronic system, resists thermalisation and has zero conductivity at finite temperature. The discovery of such a state in an electronic system, would be highly significant with respect to prevention of quantum decoherence and therefore quantum computing. The main obstacle is that of the electron-phonon interaction.

In this thesis, the breakdown of the quantum Hall effect has been studied in the context of electron-phonon decoupling. It is argued that such a decoupling manifests itself as large, hysteretic current jumps in a given sample's current-voltage characterstics. Such characteristics are shown to agree well with an overheating model. This indicates the electron system and phonon system have different temperatures and are thus decoupled. Furthermore, secondary currents jumps have been observed. It is suggested, within this thesis, that such observations could be related to a non-uniform spatial distribution of electron temperature. Work of this nature is highly relevant to the aforementioned goal of observing many-body localisation in an electronic system.

Numerous localised transport regimes have been studied in this work. Strong evidence of transport via activation to a mobility edge has been found. Significantly, an Arrhenius carrier density has been observed in a system in which

the Fermi level is below a mobility edge. Separately, an unusual low temperature Arrhenius transport regime has been observed in focused ion beam damaged graphene. Such works are important in understanding disordered electronic systems in general and will hopefully contribute to achieving many-body localisation.

In addition to its relevance to the prevention of quantum decoherence, the work presented in this thesis has other potential non-academic impact. Specifically, it is also relevant to the understanding of disorder and its impact in high quality materials, which is important for the semi-conductor industry as a whole. Insight into how disorder affects both transport and energy dissipation could help to improve performance and reliability when carrying out chip fabrication. Furthermore, the observed hysteretic current-voltage characteristics could be applied to novel electronic switches based on electron-phonon decoupling. The sharp transitions in conductivity could be used to produce switching devices in nano-scale electronic systems.

Publications In Preparation

The Hall effect and localised transport

R. Carroll, G. H. Auton, S. N. Holmes, C. Chen, D. A. Ritchie and M. Pepper

Physical Review Letters (under review)

Electron-phonon decoupling in the quantum Hall regime

R. Carroll, G. H. Auton, J. Gough, S. N. Holmes, C. Chen, D. A. Ritchie and M. Pepper

To be submitted

Acknowledgements

I would first like to thank my supervisor Prof. Sir. Michael Pepper for giving me the opportunity to work within his group. His passion, knowledge and support have been invaluable. I am also grateful to the group as a whole. In particluar, I wish to thank Dr. Gregory Auton. His help with fabrication, cryogenics and transport measurements has been deeply appreciated. Likewise, I also wish to thank Dr. Stuart Holmes and Dr. Yilmaz Gul. for offering thoughtful guidance and support whenever they were called upon. My fellow students within the group have provided a supportive and welcoming working environment. For this I am grateful and I of course wish them all well with their studies. I also wish to thank Dr. Chong Chen for providing GaAs/$Al_xGa_{1-x}As$ material and for her help at the start of my project. Finally, I would like to end by thanking Bethany, Grace and my parents for always supporting me.

Contents

Chapter 1

Introduction

Anderson's seminal 1958 work arguably founded the field of localisation within condensed matter physics [1]. It was in this work that, using a disordered tight binding model, the concept of localisation due to disorder was first introduced. Diffusive behaviour was shown to be lost. Although the initial motivation was that of electron or spin transport, Anderson localisation is now synonymous with single particle localisation, regardless of the specific system. See [2–7] for examples of Anderson localisation using photons, matter waves, ultrasound and spin waves. At the time of publication, and indeed during the proceeding decade, Anderson's work was not truly appreciated and in many cases not accepted. As a result, progress in the field was initially slow. It was not until over two decades later, in 1979, that the so-called "Gang of Four", meaning Abrahams, Anderson, Licciardello, and Ramakrishnan, established the scaling theory of localisation. The theory regards the conductance of a general disordered electronic system [8]. By using a scaling parameter that is dependent only on the conductance of a given sample, it was shown that in one and two dimensions all single electron eigenstates are localised given arbitrary disorder. This is a striking statement and was also not without controversy.

Mott was responsible for much in the field, in particular concepts such as variable range hopping [9] and the mobility edge [10]. Over half a century later, there still remain numerous unanswered issues related to both of these concepts. For example, in the variable range hopping transport regime, the experimental observation of a quantised conductivity prefactor has no explanation [11,12]. Likewise, in the context of transport in a disordered system, an Arrhenius Hall carrier density has never been observed alongisde an Arrhenius conductivity. If, as is often claimed, transport is via activation to a mobility edge, it is anticipated that the Hall carrier denisty should take on such a temperature dependence. Instead, while the conductivity is Arrhenius, it is the Hall mobility that has been consistently reported as being activated and not the carrier density [13–16]. This issue will be addressed in this thesis.

In recent years, the field of localisation has undergone somewhat of a renaissance. This is in part due to work from 2006 by Basko, Aleiner and Altshuler [17]. They showed, theoretically, that the electron-electron interaction alone does not guarantee thermalisation. A system which fails to thermalise is said to be many-body localised. Such a concept can be thought of as the many-body generalisation of Anderson localisation. Anderson himself, in his 1958 work, noted that in a localised system there is no path to equilibrium. Due to the absence of thermalisation, the concept of temperature breaks down within a many-body localised system. A fundamental property of such a system is that of zero conductivity at finite temperature. The many-body localised state is therefore considered a perfect insulator. Although many-body localisation has been reported in ultracold atomic systems [18,19], it is yet to be observed in an electronic system. The dominant obstacle is that of phonons, which act as an external bath and allow for thermalistion. Recent research has focused on experimental signatures of many-body localisation [20] and electron-phonon decoupling [21,22], the latter being a

necessary requirement to experimentally achieve the many-body localised state. In this thesis, electron-phonon decoupling will be explored in the context of the breakdown of the quantum Hall effect [23]. The quantum Hall effect, a topological effect discovered in 1980 [24], is itself dependent on disorder and localisation. By measuring in a Corbino geometry, transport via edge states can be avoided and instead the bulk localised states of the disorder broadened Landau levels can be probed.

There exists a substantial body of work in the literature in which disorder and localisation are studied using gated two dimensional electron gases, see [14,25,26]. In such systems, a metal insulator transition can be observed by using the gate to manipulate the Fermi level below a mobility edge. Furthermore, by pushing the Fermi level further below the mobiltiy edge, a systematic study of the localised states that form the band tail of the system is possible. See [27,28] for examples of transitions between different forms of localised transport as Fermi level is varied beneath a mobility edge. In this thesis, a two-dimensional electron gas, hosted in a gated GaAs/$Al_{0.33}Ga_{0.67}$As heterostructure is used to study the Hall effect in various localised transport regimes. The aforementioned issue regarding the historical lack of an Arrhenius carrier density in the literature is considered.

The layout of the thesis is as follows. The theoretical background, which is necessary in order to understand and contextualise the results, is presented in chapter 2. The materials used in this work are discussed in chapter 3, namely GaAs/Al_xGa_{1-x}As heterostructures and graphene. How the Fermi level is manipulated to lie beneath a mobility edge and thus within localised states will also be considered here. The three techniques that have been employed are the aforementioned use of gating and disorder broadened Landau levels, as well as the damging of graphene devices using a helium focused ion beam. Following this, how the fabrication of devices was carried out is presented in chapter 4. Chap-

ter 5 also discusses experimental methods, specifically how cryogenic transport measurements were performed. In the following three chapters, the results of this work are given. Firstly, in chapter 6, the Hall effect study is discussed. Specifically, how the Hall effect is altered as both Fermi level and temperature are varied in the cases of transport via activation to a mobility edge and Efros-Shklovskii hopping. In chapter 7 the breakdown of the quantum Hall effect is considered in the context of electron-phonon decoupling. Chapter 8 considers focused ion beam damaged graphene devices and ultra low temperature Arrhenius behaviour. Finally, in chapter 9, the results are summarised and potential areas of future work are raised.

Chapter 2

Disorder and Localisation

In this chapter, the relevant theoretical background concerning localisation is given. Initially, in order to introduce fundamental concepts such as the density of states and effective mass, disorder free systems are considered. Here electron states are referred to as being extended and there is no localisation. Then the discussion moves onto metallic systems in which the amount of disorder is small and transport is considered diffusive. Charge carriers can be thought of as moving at the Fermi velocity of the disorder free system, between scattering centres which are separated by distances greater than the Fermi wavelength. This treatment is semi-classical and ignores the effect of interference. When taking this into account it can be shown that backscattering processes are enhanced, leading to a quantum correction to a given sample's resistance. This is known as weak localisation. It relies on time reversal symmetry and is thus lost under application of a magnetic field. The disorder level is then increased and single particle localisation, otherwise known as Anderson localisation, is introduced. In an Anderson insulator, there exist states which are no longer extended and are considered localised. Such states have spatial extent characterised by their localisation length. Anderson himself, in 1958, commented that an Anderson localised system has no possible path to

equilibrium. This was more than 30 years before the eigenstate thermalisation hypothesis was theorised in order to deal with thermalisation of isolated quantum systems. After single particle localisation is discussed, finite temperature effects are considered. In particular, activation to a mobility edge and hopping transport. Systems displaying these transport mechanisms are considered insulators and exhibit an increase in resistivity as temperature decreases. Electron-electron interactions are then introduced in order to consider many-body localisation. As discussed in the introduction to this thesis, a many body localised state has yet to be observed in an electronic system. In such a system there is no thermalisation, conductivity vanishes below a finite temperature and it is thus considered a perfect insulator. Finally, the quantum Hall effect is discussed. This topological effect is dependent on disorder and localised states.

2.1 Periodic Potentials

Before introducing disorder and localisation, it is useful to first consider systems without disorder. Electrons in crystalline material, by definition, reside in a periodic potential. The purpose of this section is twofold. Firstly, to introduce the concept of a band structure. This is necessary when discussing how to create two-dimensional electron systems via band structure engineering. Secondly, to demonstrate that electrons in crystalline material can often be considered as free electrons but with a modified mass. As a result of this, throughout this thesis, the periodic potential of the relevant material is essentially ignored.

Bloch's theorem states that the wavefunction, $\psi(\mathbf{r})$, of an electron in a periodic potential can be expressed as a plane wave multiplied by a function that has the same periodicity as the potential [29]. That is to say,

$$\psi(\mathbf{r}) = u_{n,\mathbf{k}}(\mathbf{r}) \exp(i\mathbf{k} \cdot \mathbf{r}). \tag{2.1}$$

Here n is a band index, $\mathbf{k}$ is a wavevector and $u_{n,\mathbf{k}}(\mathbf{r})$ has the same periodicity as the potential. To see this, consider the following Hamiltonian which describes an electron in a periodic potential,

$$\hat{H} = \sum_{\mathbf{k}} \left[\frac{\hbar^2 k^2}{2m} |\mathbf{k}\rangle \langle \mathbf{k}| + \sum_{\mathbf{G}} V_{\mathbf{G}} |\mathbf{k}+\mathbf{G}\rangle \langle \mathbf{k}| \right]. \tag{2.2}$$

Here $|\mathbf{k}\rangle$ is a plane wave state with wavevector $\mathbf{k}$ and the second sum is over all reciprocal lattice vectors, including the zero vector. The $V_{\mathbf{G}}$ values are the values of the fourier transform of the periodic potential, evaluated at reciprocal lattice vector $\mathbf{G}$. This Hamiltonian is applicable to any periodic potential. The application of this general Hamiltonian to a plane wave state results in

$$\hat{H} |\mathbf{k}\rangle = \frac{\hbar^2 k^2}{2m} |\mathbf{k}\rangle + \sum_{\mathbf{G}} V_{\mathbf{G}} |\mathbf{k}+\mathbf{G}\rangle . \tag{2.3}$$

No matter the details of the periodic potential, the Hamiltonian maps between plane wave states that differ by the reciprocal lattice vectors only. It is therefore the case that a general solution can be written as

$$|\psi\rangle = \sum_{\mathbf{G}} c_{\mathbf{G}} |\mathbf{k}+\mathbf{G}\rangle \tag{2.4}$$

where $c_{\mathbf{G}}$ are constants to be determined. The associated wavefunction of this general solution, $\langle \mathbf{r}|\psi\rangle$, is

$$\psi_{\mathbf{k}}(\mathbf{r}) = \exp(i\mathbf{k}\cdot\mathbf{r}) \sum_{\mathbf{G}} c_{\mathbf{G}} \exp(i\mathbf{G}\cdot\mathbf{r}). \tag{2.5}$$

The general wavefunction is therefore a plane wave, $\exp(i\mathbf{k}\cdot\mathbf{r})$, multiplied by a function that has the same periodicity as the lattice: $\sum_{\mathbf{G}} c_{\mathbf{G}} \exp(i\mathbf{G}\cdot\mathbf{r})$. This is Bloch's theorem. It is typical to restrict the wavevectors of Bloch states to only

exist in the first Brillouin zone. This is the primitive unit cell of the reciprocal lattice. By definition of the primitive lattice, all wavevectors outside the first Brillouin zone are equal to the sum of a reciprocal lattice vector and a unique wavevector from within the first Brillouin zone. Because of this, Bloch states need only be associated with a wavevector from within the first Brillouin zone. The remainder of the plane wave term can be absorbed into the function which shares the periodicity of the lattice.

A dispersion relation is shown in Fig. 2.1 for a one-dimensional periodic potential. The potential has period a. The band gaps arise due to plane wave states at the edges of each Brillioun zone undergoing Bragg reflection and forming standing waves. In the case of Fig. 2.1, the boundary of the first Brillioun zone is at $|k| = \pi/a$. The Bragg reflection arises due to the crystal imparting momentum equal to the reciprocal lattice vectors. At the Brillioun zone boundary the reflected component exactly cancels the forward component. One of the resultant standing waves has a probability density in phase with the maxima of the potential, while the other is out of phase. Hence the energy splitting and resultant gap. Pertubation theory can also be used to see that states closer to the Brillioun zone boundary are altered more than states further from the boundary. Figure 2.1b shows the same dispersion relation as Figure 2.1a, but with wavevectors shifted by a reciprocal lattice vector so as to reside in the first Brillion zone. Two bands are shown. If the Fermi level lies within a band, the material is expected to be metallic. Otherwise, depending on the size of the gap, the material is considered either a semiconductor or an insulator. As shall be discussed in section 3.1.3, band structure engineering can be used to create metallic two-dimensional electron systems from three-dimensional semiconductors.

By considering their response to external forces, electrons in a given band can

be thought of as free electrons with a modified mass, known as an effective mass

$$\frac{1}{m^*} = \frac{1}{\hbar^2}\nabla^2_{\mathbf{k}}\epsilon_{\mathbf{k}}. \tag{2.6}$$

Here $\epsilon_{\mathbf{k}}$ is the energy of the state with wavevector $\mathbf{k}$.

In free space, the density of states, N, is found by applying periodic boundary conditions. This leads to only discrete values of wavevector being permissible. The same reasoning applies to the wavevectors associated with the Bloch states. The denisty of states is therefore the same as in free space, but with a modified effective mass. In two dimensions, the dimension of interest within this thesis, the density of states is a constant,

$$N = m^*/\pi\hbar^2. \tag{2.7}$$

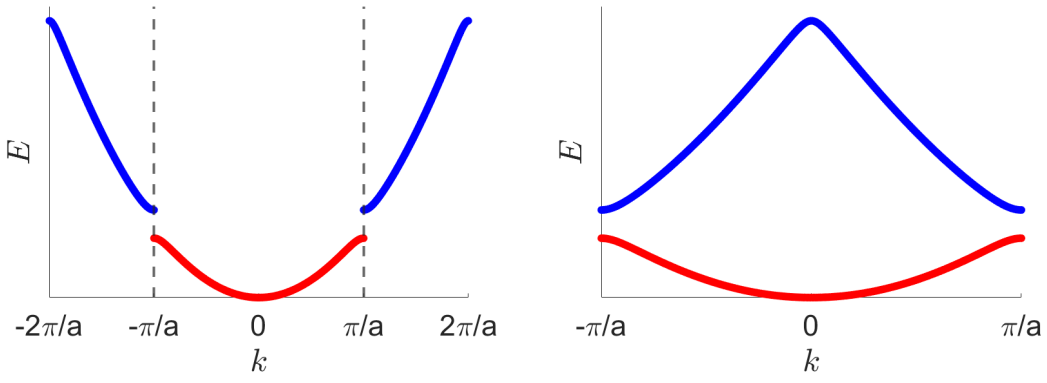

Figure 2.1: Dispersion relation for a particle in a one-dimensional periodic potential. The first two bands are shown in the a) extended zone scheme and b) reduced zone scheme.

2.2 Diffusive Conduction

Having established that electrons in a periodic potential can be considered as being essentially in free space, but with an effecective mass, disorder is now considered for the first time. Initially, the disorder will be considered weak, such that the material is still considered metallic.

The scattering time, τ, is the time it takes for an electron's initial momentum to be lost as it scatters within the material. If $f(\theta)$ is the rate of scattering into a state which has a wavevector at an angle θ from the current state, the scattering time is given by

$$\frac{1}{\tau} = \int_0^{2\pi} [1 - cos(\theta)]\, f(\theta) d\theta. \tag{2.8}$$

Here scattering events have been weighted by how significantly they affect momentum [30]. The mean free path, l, is defined as the length scale associated with τ, so-called because between scattering events the electron appears free. When considering transport, it is the states at the Fermi level that are of particular interest. It is these states that are responsible for the the net current. Thus both τ and l are defined at the Fermi level. Given the electron appears free between scattering events, $\tau = l/v_F$ where $v_F = \hbar k_F/m^*$ is the Fermi velocity and k_F is the Fermi wavevector.

In principle, the Schrödinger equation for a given realisation of disorder could be solved. Although this is typically impractical, it is instructive to consider properties of the solutions. Consider the case in which the the disorder is a random array of delta function spikes in potential energy. Each spike is referred to as a scattering centre. It is assumed that the the distance between the scattering centres is much greater than the Fermi wavelength, $\lambda_F = 2\pi/k_F$. This ensures that $l \gg \lambda_F$. The Ioffe-Regel condition [31] concerns the boundary between

metallic and insulating behaviour, known as a metal-insulator transition [32]. Using the Ioffe-Regel condition, the transition is said to occur when $k_F l \approx 1$. Hence disorder is considered weak if $l \gg \lambda_F$. Consider the case in which between the delta function scattering centres, there is simply free space. The solution of the Schrödinger equation is therefore made up of a linear combination of plane wave states, which all have wave vectors of equal magnitude. At the scattering centres, the necessary jump conditions associated with delta functions must be satisfied. An electron in such a state will appear to be undergoing Brownian motion. Between the scattering centres it appears as a free electron but, due to the disorder, the direction of its wave vector changes throughout the crystal. If the states that linearly combine to form the solution have wave vectors of magnitude k, the magnitude of the electron velocity between scattering sites will simply be $\hbar k/m^*$. The interference of the various plane wave states that linearly combine to form the new states has not been considered. This leads to the phenomenon of weak localisation and is covered in section 2.3.

A current, due to this diffusive behaviour, is now derived. Consider a voltage, V, applied between two reservoirs on either side of a two dimensional sample. The difference in electrochemical potential between the two reservoirs is eV, where e is the electron charge. One reservoir injects eVN more electrons per unit area than the other, where N is the density of states at the Fermi level. The result is a carrier density concentration gradient, $\nabla n = -eVN/L$, where n is the two-dimensional electron density and L is the length of the sample. The current density can thus be expressed as,

$$J = -eD\nabla n = \frac{e^2 DVN}{L} \tag{2.9}$$

using Fick's first law [33] and where $D = l^2/2\tau$ is the the diffusion constant. Using

$v_F = \hbar k_F/m^* = l/\tau$, $N = m^*/\hbar^2\pi$ and $n = k_F^2/2\pi$ results in,

$$J = \frac{ne^2\tau V}{m^* L} = \frac{ne^2\tau}{m^*}E, \tag{2.10}$$

with $E = V/L$ being the applied electric field. This results in the conductivity taking the form,

$$\sigma = \frac{ne^2\tau}{m^*}. \tag{2.11}$$

The same conductivity also follows from the classical Drude model [34, 35]. This model assumes that all carriers contribute to the conductivity. These carriers are all randomly scattered, with scattering time τ, while being accelerated by the electric field. This results in a mean drift velocity of all carriers of $eE\tau/m^*$. Mobility, often used as a parameter of material quality, is defined as the ratio of this drift velocity to the applied electric field, therefore $\mu = e\tau/m^*$ within the Drude model. Using (2.11), $\mu = \sigma/ne$.

2.3 Weak Localisation

While discussing diffusive transport, quantum interference was neglected. The analysis was essentially classical. In order to consider quantum interference, the concept of time-reversal symmetry is first introduced. Consider the single particle time-dependant Schroedinger equation in the position basis,

$$i\hbar\frac{\partial\psi(\mathbf{r},t)}{\partial t} = -\frac{\hbar^2}{2m}\nabla^2\psi(\mathbf{r},t) + V(\mathbf{r})\psi(\mathbf{r},t). \tag{2.12}$$

Taking its complex conjugate and making a change of variables such that $t \to -t$ results in,

$$i\hbar\frac{\partial\psi^*(\mathbf{r},-t)}{\partial t} = -\frac{\hbar^2}{2m}\nabla^2\psi^*(\mathbf{r},-t) + V(\mathbf{r})\psi^*(\mathbf{r},-t). \tag{2.13}$$

Hence it can be seen that if $\psi(\mathbf{r}, t)$ is a solution to the Schrödinger equation, then so is $\psi^*(\mathbf{r}, -t)$. Such a system is said to display time-reversal symmetry. By taking the complex conjugate of the time independent Schrödinger equation, it can be shown that both solutions have the same energy eigenvalues. It is important to note that if a magnetic field is present this logic does not apply. One can easily check this by replacing $-\frac{\hbar^2}{2m}\nabla^2$ with $\frac{1}{2m}(-i\hbar\nabla + e\mathbf{A})^2$, where $\mathbf{A}$ is the magnetic vector potential. The Hamiltonian is no longer real in the position basis. Magnetic fields break time reversal symmetry. As shall be seen in section 2.8.2 this is crucial to the quantum Hall effect.

Systems which are time reversal symmetric display a phenomenon known as enhanced backscattering. A central quantity, when considering such a phenomenon is the propagator,

$$A(\mathbf{r}_0, \mathbf{r}_{end}, t) = \langle \mathbf{r}_{end} | \, e^{-i\hat{H}t} \, | \mathbf{r}_0 \rangle \, . \tag{2.14}$$

This is the probability amplitude that an electron moves from $\mathbf{r}_0$ to $\mathbf{r}_{end}$ in time t. As shown in appendix A, the propagator is the sum of the probability amplitudes associated with each possible path the electron can take between $\mathbf{r}_0$ and $\mathbf{r}_{end}$. Consider two paths, which both go from one point back to itself but in opposite directions. An example is shown in Fig. 2.2. In a time reversal symmetric system these paths can be shown to have the same associated probability amplitudes. They will thus interfere coherently. See section A for details. To see why this leads to weak localisation, consider adding all of the probability amplitudes, denoted α_i, associated with different paths for a particle going from $\mathbf{r}_0$ to some other point $\mathbf{r}_x$ in time t. The probability, $P(\mathbf{r}_0, \mathbf{r}_x, t)$, the particle moves from $\mathbf{r}_0$ to $\mathbf{r}_x$ in this time is simply the square of the magnitude of the sum.

$$P(\mathbf{r}_0, \mathbf{r}_x, t) = |\sum_i \alpha_i|^2. \tag{2.15}$$

For $\mathbf{r}_x \neq \mathbf{r}_0$ no correlation between the phases of the various paths is assumed, which leads to the classical result,

$$P(\mathbf{r}_0, \mathbf{r}_x, t) = \sum_i |\alpha_i|^2 \text{ for } \mathbf{r}_x \neq \mathbf{r}_0. \tag{2.16}$$

However if $\mathbf{r}_x = \mathbf{r}_0$, each α_i value will be equal in magnitude and phase to another, associated with the same path in the opposite direction. Assuming no further correlations,

$$P(\mathbf{r}_0, \mathbf{r}_0, t) = \sum_i \frac{1}{2}|2\alpha_i|^2 = 2\sum_i |\alpha_i|^2. \tag{2.17}$$

This is the essence of weak localisation [36]. In a system that is time-reversal symmetric, the probability of being back scattered is twice the classical value, while other probabilities are not affected.

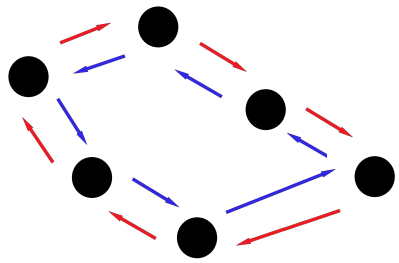

Figure 2.2: Two paths, which are the same just in opposite directions, will interfere constructively in a system with time-reversal symmetry.

In the previous section the concept of a transport lifetime was introduced. This is the timescale over which the transport appears ballistic. Another timescale is now introduced, the phase coherence time, τ_ϕ. This is defined as the time over which a particle retains its phase. Couplings to other degrees of freedom, such as other electrons and phonons, result in the suppression of quantum interference [37]. Associated with the phase coherence time is the phase coherence length, l_ϕ. Over such a length scale, assuming $l_\phi > l$, the electron will appear weakly

localised due to interference effects and the resultant enhanced back scattering. The phase coherence time and length are related by,

$$l_\phi^2 = D\tau_\phi = \frac{l^2\tau_\phi}{2\tau}, \tag{2.18}$$

where D is the diffusion constant defined in section 2.2.

Perhaps counter intuitively, conductivity decreases as phase coherence length increases, assuming a constant mean free path. This is due to the strengthening of weak localisation, which relies on quantum interference and thus on phase coherence. How phase coherence, or lack of, quantitatively affects the conductivity of a material will now be discussed using arguments from [38]. First consider the Landauer conductance formula, see [39] and appendix B,

$$G_{cl} = \frac{2e^2}{h}MT. \tag{2.19}$$

Here M is the number of modes and $T = 1 - R$ is the transmission coefficient which is assumed to be the same for all modes, for simplicity. The reflection coefficient is R. This conductance formula however, ignores quantum interference. As previously discussed, the probability of an electron being back-scattered to its initial position is twice its classical value. Likewise it can also be shown that the probability an electron in a given mode is reflected back into this same mode is twice its classical value. Thus the value of R, when quantum interference terms are considered, should increase by R/M. This results in,

$$G_q = \frac{2e^2}{h}M(1 - R - \frac{R}{M}) = G_{cl} - R\frac{2e^2}{h} \tag{2.20}$$

where G_q is the conductance considering quantum interference while G_{cl} ignores

it. If the reasonable assumption that $R \approx 1$ is made then,

$$G_q = G_{cl} - \frac{2e^2}{h}. \tag{2.21}$$

Note that this only holds for phase coherent materials, meaning the phase coherence length must be larger than the sample size. Now consider piecing together blocks of width $W < l_\phi$ and length l_ϕ to form a sample with width W and length $L >> l_\phi$. As the resistance of the blocks will add in series, the conductivity of one block is the conductivity of the whole sample. Thus, using (2.21),

$$\sigma_q = \sigma_{cl} - \frac{2e^2}{h}\frac{l_\phi}{W} \tag{2.22}$$

where σ_q is the conductivity considering quantum interference while σ_{cl} ignores it. However, this only holds while the width of the sample is less than the phase coherence length. This is essentially a one dimensional result. To find the two dimensional conductivity of a sample with width greater than this length, a circular geometry should be considered. This is due to diffusion being radial. The conductivity of an annulus of inner radius l and outer radius l_ϕ is considered. It is argued that its conductivity will also be the conductivity of larger samples. Choosing l_ϕ as the outer radius is an obvious choice; the largest possible phase coherent unit is wanted. The inner radius cannot be zero. This is due to the divergence of the current density associated with a current point source. Choosing the mean free path, l, for the inner radius is appropriate as any transport between the centre of the annulus and the inner radius will be ballistic. Thus conductance should not be significantly affected by removing an inner circle of this radius from consideration. As this is a phase coherent unit the conductance between inner

and outer radii is again given by (2.21). Using,

$$V = \int_l^{l_\phi} E(r) \cdot dr = \frac{1}{\sigma_q} \int_l^{l_\phi} J(r) \cdot dr \tag{2.23}$$

and

$$J(r) = \frac{I}{2\pi r}, \tag{2.24}$$

where I is the current between the two radii, V is the voltage between them and $J(r)$ is current density at radius r, it can be seen that

$$G_q = \frac{I}{V} = \frac{2\pi\sigma_q}{\log(l_\phi/l)}. \tag{2.25}$$

Combining (2.25) and (2.21) leads to

$$\sigma_q = \sigma_{cl} - \frac{e^2}{\pi h} \log(l_\phi/l), \tag{2.26}$$

which is applicable when $l < l_\phi$ and by construction holds for larger samples, not just the phase coherent sample considered.

The quantum correction in (2.21) will not be exactly $-2e^2/h$. Variations in the quantum correction value result in the phenomenon known as universal condutance fluctuations. Different realisations of disorder within otherwise identical phase coherent samples will lead to fluctuations in conductance of order $2e^2/h$, see [40,41]. The lengthscale on which these fluctuations can be observed is known as the mesoscopic length scale. These fluctuations can be observed in samples that are larger than the phase coherence length, but they will decrease in magnitude as length increases. The fluctuations over each phase coherent unit are essentially averaged out as the number of phase-coherent units is increased.

Using (2.18), the weak localisation correction given by (2.26), can be expressed

in terms of τ_ϕ and τ,

$$\sigma_q = \sigma_{cl} - \frac{e^2}{2\pi h} \log(\tau_\phi / 2\tau). \tag{2.27}$$

Given that τ_ϕ is typically expected to have a power-law dependence on temperature, $\tau_\phi \propto T^\alpha$, it can be seen that the weak localisation correction should have a logarithmic temperature dependence. In two dimensions it is expected that electron-electron interactions result in $\tau_\phi \propto T^{-1}$ [42].

As previously discussed, a magnetic field breaks the time reversal symmetry that is needed for weak localisation. Hence for small magnetic fields one often observes a decrease in resistance as the magnitude of the magnetic field increases. Coherent back scattering is reduced. For larger magnetic fields this simple description no longer works and one needs to consider the quantum Hall effect, see section 2.8.2. One can also observe weak anti-localisation. See [43] for the magnetic field dependence of the weak localisation correction, applicable to both weak localisation and weak anti-localisation. In the case of weak anti-localisation, quantum interference leads to a reduction in back scattering and a magnetic field thus increases resistance. This can be observed in materials with strong spin-orbit coupling. See [44, 45] for experimental demonstrations.

The temperature dependence of the weak localisation correction is similar to another correction term, namely the Altshuler-Aronov (AA) correction [46]. This correction is due to the combination of disorder and the electron-electron interaction. Spatial charge fluctuations due to the electrons themselves, induced by disorder, are further sources of scattering. The correction takes the form

$$\sigma_{AA} \approx -\frac{e^2}{\pi h} \log(\hbar / \tau k_B T). \tag{2.28}$$

Differentiating between the AA correction and the weak localisation correction is difficult using only a sample's temperature dependence, as they have similar

forms. However, the AA correction is relatively insensitive to low magnetic fields, unlike the weak localisation correction. This is due to weak localisation being dependent on time reversal symmetry.

Finally the conductance of a ring with magnetic flux through its centre is considered; both the Aharonov-Bohm effect [47, 48] and the Altshuler-Aronov-Spivak (AAS) effect [49] are discussed. If there is little disorder within the ring and the mean free path is of similar magnitude or larger than that of the ring, the transport can be considered ballistic. If the phase coherence length also meets this criteria, then oscillations in conductance as flux through the ring is varied will be observed. Paths going opposite ways around the ring interfere. The magnetic vector potential affects the phases of the interfering paths. The flux period will be h/e. This is known as the Aharonov-Bohm effect. The effect can be used to measure phase coherence lengths. See [50] for an example concerning the temperature dependence of the phase coherence length and [51,52] for similar measurements utilising weak localisation. Note that the ring does not have to be on the expected classical current path to observe the oscillations, see [53] for an experimental example of this. If however the transport is no longer ballistic, but still phase coherent, one can observe oscillations of period $h/2e$. Conduction is diffusive and it is instead paths that go all the way around the ring which interfere, which halves the flux period. This is the AAS effect.

2.4 Mott Insulators

In 1937 de Boer and Verwey discovered that numerous transition metal oxides, such as NiO, disagree with the predictions of band theory. The materials were experimentally found to be insulators, but were predicted to have partially filled valence bands and should therefore, by the logic of band theory, be metallic [54]. Mott proposed that the disagreement between theory and reality was due to

electron-electron interactions [55]. A Mott insulator is a material that band theory would predict as being a conductor, but electron-electron interactions result in it being an insulator. Mott insulators are not reliant on disorder. A classic example of a Mott insulator is the Hubbard model [56]. In this model, electrons can hop between neighbouring sites but an energy penalty must be paid if two electrons occupy the same site, due to Coulomb repulsion. The Hamiltonian is,

$$\hat{H} = -t \sum_{<i,j>,\sigma} \hat{c}^{\dagger}_{i,\sigma} \hat{c}_{j,\sigma} + U \sum_{i} \hat{n}_{i,\downarrow} \hat{n}_{i,\uparrow}. \tag{2.29}$$

Here the first sum is over nearest-neighbour sites, t parameterises the hopping, U is the energy cost to have two electrons occupy the same site, $\hat{c}^{\dagger}_{i,\sigma}$ is the creation operator for spin σ on site i and $\hat{n}_{i,\sigma} = \hat{c}^{\dagger}_{i,\sigma} \hat{c}_{i,\sigma}$. If $U = 0$ this is simply a tight binding model, which is a simple to solve single particle Hamiltonian. In this case, if there are N sites which are regularly spaced in one dimension with spacing a, the eigenstates are

$$|\psi_k\rangle = \frac{1}{\sqrt{N}} \sum_{n} \exp(ikna) \, |n\rangle \, . \tag{2.30}$$

Here spin has been ignored, $|n\rangle$ is the state associated with site n and the wavenumber, k, is such that $k \in [-\pi/a, \pi/a)$ and is quantised in units of $2\pi/aN$ when periodic boundary conditions are imposed. There are thus N solutions. They have energies

$$E(k) = -2t \cos(ka). \tag{2.31}$$

The resultant band has bandwidth $4t$. Unless this single band is completely filled, the system will be metallic.

When U is finite, the problem is no longer a trivial single particle problem. Without offering a many-body solution, it is still instructive to consider what properties the dispersion relation of the many-body eigenstates will have. In-

cluding spin, there will be $2N$ many-body eigenstates. If there are N electrons in the system, all with same spin, one can imagine filling up all states of the aforementioned spinless tight binding Hamiltonian. This corresponds to having one electron per site. If one wanted to add an additional electron, of opposite spin to the N electrons in the system, it would cost energy U even if the energy associated with its wavenumber was as low as possible. This energy is measured relative to the bottom of the first fully occupied band. Given the bandwidth of the first fully occupied band is $4t$, if $U > 4t$ the system will be gapped. Two bands, known as Hubbard bands, are formed. In this case, if there is one electron per site, the system will be an insulator. This would not have been predicted by band theory and is a result of electron-electron repulsion. This is the essence of a Mott insulator. In d dimensions the requirement becomes $U > 4dt$, as the bandwidth in d dimensions is $4dt$. Note that a Mott insulator is not many-body localised as it will have non zero conductivity at any finite temperature due to excited states within the upper Hubbard band.

2.5 Single-Particle Localisation

The discussion of section 2.2, regarding diffusive metallic conduction, considered the situation in which $l \gg \lambda_F$. This allows one to consider that electrons travel as free particles between scattering events, leading to the discussed diffusive transport. In this section, much greater levels of disorder are considered meaning that this is no longer the case. The previously discussed Ioffe-Regel criterion essentially states that when $l \approx \lambda_F$, the disorder is large enough to form localised states at the Fermi level. These states are fundamentally different from the extended plane wave states previously discussed. The natural starting point for a discussion of such a system is Anderson's seminal 1958 work [1].

2.5.1 1958 Anderson Result

In 1958 Anderson considered the following single particle Hamiltonian which models the superposition of disorder onto on a perfect crystalline lattice,

$$\hat{H} = \sum_i E_i \hat{c}_i^\dagger \hat{c}_i - t \sum_{<i,j>} \hat{c}_i^\dagger \hat{c}_j. \tag{2.32}$$

Here $< i, j >$ denotes nearest neighbour sites, t is the hopping integral between these nearest neighbours and $\hat{c_i}^\dagger$ is the fermion creation operator for site i. Disorder is incorporated by asserting that the E_i values are uniformly distributed between $-W$ and $+W$. This is essentially a tight binding Hamiltonian but with the addition of disorder.

In one and two dimensions, any finite value of W results in all eigenstates being localised. Thus arbitrary disorder is enough to prevent the existence of any extended states. An example of such a localied state in two dimensions, itself the result of solving (2.32) numerically, is shown in Fig. 2.3. The wavefunction of a localised state decays exponentially with distance from its centre. The rate of decay is $1/\xi$, where ξ is known as the localisation length and ultimately characterises the spatial extent of the state. However, due to finite sample size, localised states can appear extended. This is the case if $\xi > L$, where L is sample size. Furthermore, if $\xi > l_\phi$ states will again appear extended. Phase coherence, as with weak localisation, is necessary to form localised states. If phase coherence is not preserved over the localisation length, Anderson localisation will break down. Due to the temperature dependence of electron-electron scattering and phonon scattering rates, this is a finite temperature effect. At zero temperature, phase coherence length diverges. Both finite sample size and finite temperature effects explain the existence of two-dimensional metallic systems.

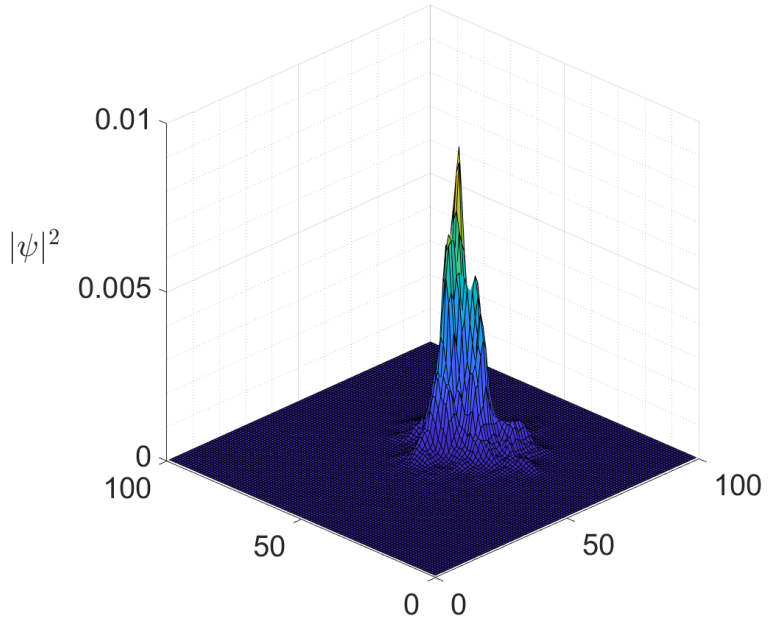

Figure 2.3: Two-dimensional numerical solution of Anderson's model, (2.32), demonstrating a localised state.

The situation is qualitatively different in three dimensions. Not all eigenstates are localised under the influence of arbitrary disorder. In other words, a small degree of disorder will not prevent the existence of extended states. With respect to the Anderson Hamiltonian (2.32), the value of $\gamma = t/W$ can be used to quantify this statement. On a Bethe lattice, equivalent to an infinite regular Cayley tree, with branching number K the critical value,

$$\gamma_c = \frac{1}{K \log K} \tag{2.33}$$

determines if all states are localised or not. For $\gamma < \gamma_c$ all eigenstates are indeed localised [57]. A cubic lattice in three dimensions can be approximated as a Bethe lattice with $K = 6$.

Extended states and localised states cannot share the same eigenvalues [58]. Otherwise, any perturbation in the disorder potential will hybridise the states

formerly of the same energy, leading to them all becoming extended. There would then be no localised states. The boundary, in energy, between the two is known as a mobility edge [10]. Localised states exist in band tails [59]. Figure 2.4 depicts the density of states of a band tail, with the mobility edge labelled. If the Fermi level is below the mobility edge, transport is no longer metallic. In two dimensions, due to finite temperature, a quasi mobility edge exists. This separates localised states and states that, as previously discussed, appear extended and support metallic transport.

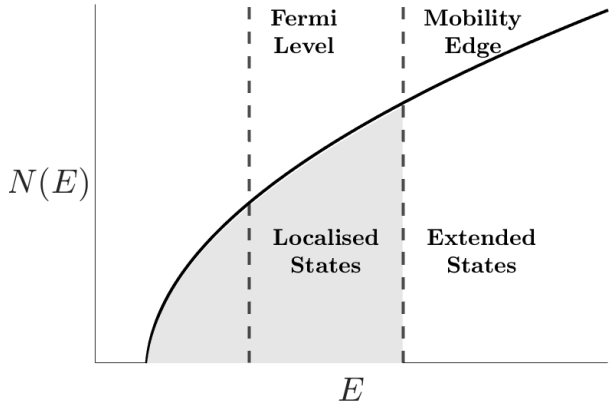

Figure 2.4: Density of states within a disordered materal. The energy at which states become extended is known as the mobility edge. In two dimensions a quasi mobility edge exists due to finite temperature or finite sample size effects.

There are numerous methods that can be used to differentiate between localised and extended states. One such method involves the spectral statistics of the eigenenergies [60]. The normalised energy level spacings are defined as

$$s_i = \frac{E_i - E_{i-1}}{\langle E_i - E_{i-1} \rangle}, \tag{2.34}$$

where the E_i values are the ordered eigenenergies. The s_i values exhibit a Poisson distribution if the eigenstates are localised. Due to the finite spatial distibution of localised states and resultant lack of energy level repulsion, there is no correlation

between neighbouring E_i values. The maximum of the probability density function, $P(s)$, is therefore found at $s = 0$. However, if the eigenstates are extended, due to energy level repulsion, $P(0) = 0$ and the s_i values are Wigner-Dyson distributed [61]. A second method involves the spatial distribution of the eigenstates [62]. If $|n\rangle$ denotes the site associated with the nth lattice site, the inverse participation ratio (IPR) of a general state $\sum_n c_n |n\rangle$ is defined as

$$I = \sum_n |c_n|^4. \tag{2.35}$$

For a system of N lattice sites, $1/N \leq I \leq 1$. A fully localised state has $I = 1$, whereas $I = 1/N$ corresponds to an extended state which has spatially uniform probability density. A general extended state has $I = O(1/N)$. The IPR can thus be used to differentiate between localised and extended states.

2.5.2 Scaling Theory of Localisation

In 1979 the so-called 'Gang of Four' proposed a scaling theory of localisation. As with Anderson's earlier work, they concluded that arbitrary disorder in both one and two dimensions results in all states being localised [8]. The fundamental assumption upon which their work lies, is that the conductance of a sample, g, can be expressed purely as a function of the sample's conductance on a smaller length scale. That is to say

$$g(2^d L^d) = f\left[g(L^d)\right], \tag{2.36}$$

where L is sample size and d is dimensionality. Here $g = (h/e^2)/R$ denotes dimensionless conductance, where R is resistance. To provide necessary context underlying this reasoning, work by Thouless which considered the possibility of a maximum metallic resistance of a thin wire [63], is first discussed.

Consider a wire of length L and cross sectional area A. Assuming the wire is metallic, meaning states are extended and conduction is thus diffusive, conductivity has the form

$$\sigma = e^2 DN, \tag{2.37}$$

where D is the diffusion constant and N is the density of states per unit volume, as discussed in section 2.3. The time taken to diffuse through the wire is given by L^2/D and the associated energy uncertainty is thus,

$$\epsilon = \frac{\hbar D}{L^2}. \tag{2.38}$$

If $R = L/\sigma A$ is the resistance of the wire,

$$\epsilon = \frac{\hbar\sigma}{L^2 e^2 N} = \frac{\hbar}{Re^2 LAN}. \tag{2.39}$$

The average spacing between energy levels at the Fermi level, $\Delta = 1/LAN$, can be used to rewrite this as,

$$\epsilon = \frac{h}{Re^2}\Delta. \tag{2.40}$$

Consider joining two of these wires, resulting in the wire length doubling. If the energy uncertainty, ϵ, is greater than the level spacing, Δ, the difference in energies between states in the first wire and the states in the second wire are not resolved with respect to the energy uncertainty of the electrons. Electrons will continue to be able to diffuse through the wire. Whereas if the energy uncertainty is less than the level spacing, this will not be the case. The ratio of the two energies is simply the dimensionless conductance of the first wire,

$$g = \frac{\epsilon}{\Delta} = \frac{h}{Re^2}. \tag{2.41}$$

If $g > 1$, diffusive conduction is expected meaning extended states at the Fermi level. Whereas if $g < 1$ the opposite is true, meaning localised states. This results in the, perhaps surprising, conclusion that for a one dimensional wire, its resistance can simply determine whether or not the states at the Fermi level are localised or not. Furthermore, the maximum metallic resistance, using this reasoning, is $R = e^2/h$. This analysis, of course, lacks rigour, but it is expected to be indicative of what is happening with states at the Fermi level when $g \ll 1$ or $g \gg 1$. Furthermore, it provides the motivation for (2.36) which asserts that the conductance of a sample of size $2L$ depends only on the conductance of a sample with size L, generalised to d dimensions. It follows from (2.36) that the change in g with L can be expressed via a dimensionless scaling function which itself only depends only on g,

$$\frac{d \log g}{d \log L} = \beta(g). \tag{2.42}$$

Assuming extended states and Ohm's law for large conductances, $g = (h/e^2)\sigma L^{d-2}$, results in

$$\lim_{g \to \infty} \beta(g) = d - 2. \tag{2.43}$$

Likewise, assuming transport via localised states at low conductances, $g = Ce^{-\alpha L}$, results in

$$\lim_{g \to 0} \beta(g) = \log g - \log C. \tag{2.44}$$

Based on these limits, Fig. 2.5 displays plots of $\beta(g)$ against $\log(g)$. Crucially, in one and two dimensions, $\beta(g)$ is always less than zero. Using (2.42), it can be seen that the system will always flow towards localised behaviour. As the amount of disorder has not been specified, the conclusion is that arbitrary disorder will cause localisation. This is not the case in three dimensions. If $\beta(g)$ is greater than zero, this will stay the case and conductance will always increase as sample size

increases. Extended states will be present. Arbitrary disorder does therefore not necessarily cause localisation in three dimensions. It should also be noted that the assumption of a one parameter scaling function, $\beta(g)$, is controversial. See [64] for experimental work arguing against it.

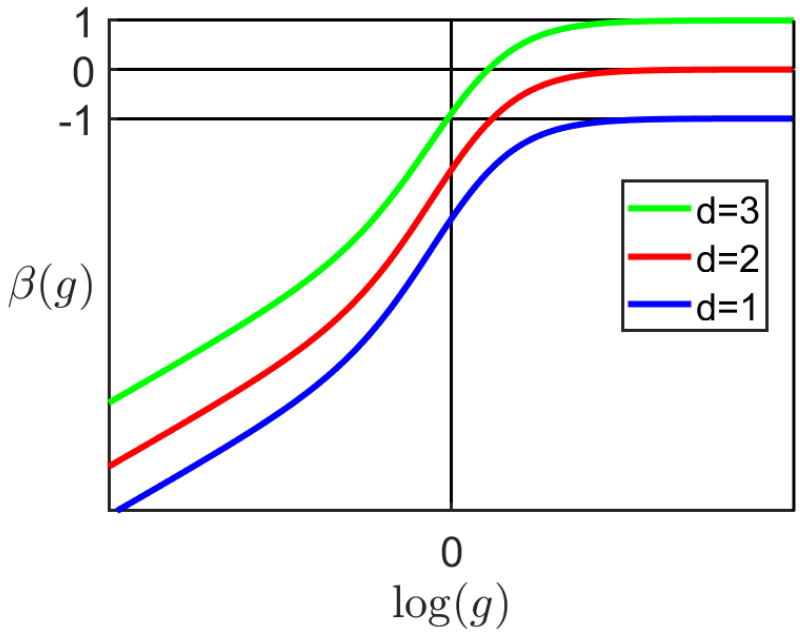

Figure 2.5: Plot of $\beta(g)$ against $\log g$. The high and low limits of g were used to find the limits of $\beta(g)$.

2.6 Finite Temperature Effects

The effect of a finite temperature typically decreases the strength of quantum interference, due to phase breaking scattering events [65]. This can reduce weak localisation and even prevent the formation of Anderson localised states, as discussed in sections 2.3 and 2.5 respectively. Additionally, as shall be discussed in this section, finite temperature effects result in a finite conductivity while the Fermi level resides within localised states. The two most common mechanisms, and the two which are studied within this thesis, are transport via activation to a mobility edge and via hopping between localised sites. These mechanisms,

and how they can be detected via their different conductivity temperature dependences, are discussed within this section.

2.6.1 Activation to a Mobility Edge

When the Fermi level is below a mobility edge, conduction can occur via activation from the Fermi level to the extended states above the mobility edge. The expected form of the conductivity is thus Arrhenius,

$$\sigma = \sigma_0 \exp\left(-\frac{T_0}{T}\right). \tag{2.45}$$

In this instance, $T_0 = (E_\mu - E_F)/k_B$, where E_μ is the mobility edge energy and E_F is the Fermi energy. See [13–16, 25, 26] for experimental examples of such behaviour in silicon inversion layers and Ge-Sn quantum wells . The value of σ_0 has been predicted to take on a universal value known as the minimum metallic conductivity, the reasoning being that conduction is taking place just above a mobility edge. Here the conductivity is necessarily metallic, but the extended states hosting the transport are on the boundary of a metal insulator transition. Hence the concept of a minimum metallic conductivity. The Ioffe-Regel condition can be used to predict the value of σ_0. As previously discussed in section 2.2, the condition states that a metal-insulator transition is expected when $k_F l \approx 1$. Inserting this approximation into the diffusive conductivity expression, (2.11), results in a two-dimensional minimum metallic conductivity of $\sigma_0 \approx e^2/h$. Mott predicted a minimum metallic conductivity of $\sigma_0 = 0.7e^2/h$ [66]. The value of σ_0 should not be affected by movement of the Fermi level, assuming it stays below the mobility edge. This is due to σ_0 being purely dependent on the states above the mobility edge. See [14, 25, 26] for examples of this, in which gate voltages are used to manipulate the Fermi level and σ_0 remains constant. The measured

values of σ_0 in these works are close to Mott's predicted value.

If the mechanism of transport is via activation to a mobility edge, it is anticipated that the carrier density of the sample should also have an Arrhenius temperature dependence. Assuming the temperature dependence of the conductivity of the states above the mobility edge is negligible in comparison, the carrier density should have the same characteristic temperature as the conductivity. That is, the carrier density takes the form,

$$n(T) = n_0 \exp\left(-\frac{T_0}{T}\right) \tag{2.46}$$

where n_0 is a function of the density of states above the mobility edge. Using (2.45) and (2.46), the mobility, given by $\mu = \sigma/ne$, will simply be a temperature independent constant, $\sigma_0/n_0 e$. However, an Arrhenius carrier density, in which carriers are activated to a mobility edge, has never been reported in the literature. If it was observed, it would be strong evidence in support of the conduction via activation to the mobility edge model. Ignoring issues related to the finite lifetime at the mobility edge, an Arrhenius carrier density is a necessity of the model. In this work, such behaviour has been observed and will be presented in chapter 6.

Carrier density is typically measured via the Hall effect. See section 2.8 for a simple description of the effect. There are many instances of temperature dependent Hall measurements being made, in order to investigate activated transport, dating back to the 1960s. Instead of an activated carrier density, a temperature independent carrier density and an activated mobility have consistently been reported. See [13–16]. This is not compatible with the activation to mobility edge model. The physical picture behind this is not clear and an accepted model describing this effect does not exist. A viscous liquid model was proposed in [67]. In this model, carriers are strongly correlated and groups of them move as one

between differing configurations. The potential energy barriers between such configurations is responsible for the activated conduction. Not all carriers move at the same time, but the carriers as a whole are considered as being a viscous fluid which can transmit pressure. The Lorentz force acting on a group of instantaneously moving carriers is thus transmitted to the whole of the fluid, meaning it is spread between all carriers. The resultant Hall voltage is thus what it would be if all carriers were moving at the same velocity independently of each other. Such a Hall voltage is independent of temperature, leading to a temperature independent carrier density. This, combined with the activated conductivity, leads to an activated mobility being measured. However, the model is essentially classical and fails to account for interference effects.

2.6.2 Nearest Neighbour Hopping

Unlike conduction via activation to a mobility edge, in which transport takes place in extended states, conduction can also occur via localised states. Such transport is referred to as hopping; carriers are said to hop between localised states. Hopping is typically considered to be phonon-assisted. That is, each hop is associated with the emission, or absorption, of a phonon. However, as shall be discussed, hopping can also take place due to the electron-electron interaction. In either case, as with activation to a mobility edge, hopping is a finite temperature effect.

Miller and Abrahams calculated transition rates of electron hops using the deformation potential approximation of the electron-phonon interaction. Under this approximation, the energy change of a given localised site varies linearly with the strain, due to phonons, at that site [68]. The rate at which an electron hops

from an occupied site i to an unoccupied site j was shown to be,

$$\Gamma_{ij} = \begin{cases} \lambda_0 \exp\Big(-2R_{ij}/\xi - (E_j - E_i)/k_B T \Big) & \text{for} \quad E_j > E_i \\ \lambda_0 \exp(-2R_{ij}/\xi) & \text{for} \quad E_i > E_j, \end{cases} \tag{2.47}$$

where R_{ij} is the distance between sites i and j, E_i is the energy of site i and λ_0 is a constant that depends on the phonon system. For $E_j > E_i$, the exponent contains both a distance term and an energy difference term. The distance term is related to the overlap of two localised sites which have localisation length ξ. The factor of two is due to taking the square of the matrix element when considering the electron-phonon interaction as a perturbation. It can be shown that (2.47) is applicable in general, regardless of the hopping mechanism, be it electron-phonon or electron-electron interactions. See appendix C and [69]. At high temperatures the upward energy jumps, meaning $E_j > E_i$, are dominated by the distance term, $-2R_{ij}/\xi$. In this case, smaller distances are greatly favoured and hops predominately occur between nearest-neighbour sites. Considering only these hops, the distance term is then effectively a constant and can be absorbed into the prefactor of the exponent. This leads to a nearest-neighbour hopping conductivity

$$\sigma_{NN} = \sigma_0 \exp(-T_0/T) \tag{2.48}$$

where σ_0 is the prefactor of the conductivity and $T_0 = k_B E_{NN}$ is a characteristic temperature where E_{NN} is the energy difference between nearest neighbour sites. Like activation to a mobility edge, nearest neighbour hopping results in an Arrhenius conductivity. See [28, 70] for experimental examples. How the form of the hopping conductivity varies with both temperature and the electron-electron interaction will now be discussed.

2.6.3 Mott Variable Range Hopping

Mott considered hopping at temperatures lower than the nearest-neighbour regime. At such temperatures, hopping will be less likely to occur via nearest-neighbour sites. Hops between sites separated by greater distances and, crucially, smaller energies will be favoured. The result is known as Mott variable range hopping [9]. Mott's original analysis involved maximising the rates given by (2.47). This can be done by simply minimising the argument of the exponent. Before doing so, the distance covered by a hop must be related to the energy jump of a hop. In d dimensions the distance between localised states within an energy interval ϵ around the Fermi level is given by

$$r \approx \left(\int_{E_F}^{E_F+\epsilon} N(E) dE \right)^{-1/d}. \tag{2.49}$$

Assuming a constant density of states,

$$r \approx (N\epsilon)^{-1/d}. \tag{2.50}$$

As hopping takes places around the Fermi level, a hop between sites separated by energy ϵ will be separated spatially by approximately the distance given by (2.50). Using (2.47), the hopping rate between two sites separated by a distance r is thus

$$\Gamma_r = \lambda_0 \exp\Big[-2r/\xi - 1/(r^d N k_B T) \Big]. \tag{2.51}$$

Only upward energy jumps have been considered as only their rates vary with temperature and thus only they will affect the temperature dependence of the hopping conductivity. Maximising the rate with respect to r results in an optimal

hopping distance of

$$r_{VRH} = \xi \left(\frac{d}{2N\xi^d k_B T} \right)^{\frac{1}{d+1}} . \tag{2.52}$$

Due to the exponential term, the reasonable assumption is made that hops over this distance dominate the transport. The conductivity can therefore be expressed as

$$\sigma_{VRH} = \sigma_0 \exp\left[- \left(T_0/T \right)^{\frac{1}{d+1}} \right] . \tag{2.53}$$

Here T_0 is a characteristic temperature. A more rigorous analysis using percolation theory is given in [69], see appendix C. This results in $T_0 = \alpha_d / N k_B \xi^d$, where α_d is a dimensional dependent constant. A Monte Carlo procedure was used to find $\alpha_2 = 13$ in [71]. Regardless, the extra rigour does not change the general form of the conductivity temperature dependence. Unlike nearest-neighbour hopping and activation to a mobility edge, the transport is not Arrhenius. Thus, by measuring a given material's conductivity temperature dependence, variable range hopping can be detected straightforwardly.

Note that as temperature increases the variable range hopping distance decreases, see (2.52). The transition to nearest neighbour hopping will occur when $r_{VRH} \approx r_{NN}$, due to the impossibility of $r_{VRH} < r_{NN}$. See [27, 28] for an example of a transition between the two regimes. As anticipated, the variable range regime occurs at lower temperatures. The effect of electron-electron interactions on hopping transport will be discussed next.

2.6.4 Efros-Shklovskii Hopping

When discussing Mott variable range hopping, a central assumption is that the density of states is constant around the Fermi level. Efros and Shklovskii considered electron-electron interactions and argued that this is not the case [72]. They argue that the density of states is zero at Fermi level, $N(E_F) = 0$. This is known

as the Coulomb gap and results in a modification to the temperature dependence of variable range hopping transport.

The Coulomb gap was first considered by Pollak [73], with Efros and Shklovskii determining its form. Before considering the quantitative form of the Coulomb gap, a qualitative argument, from [74], justifying its existence is first given. Consider adding an electron to a system of localised electrons in their ground state. Prior to the addition the Fermi level is E_F. Let the electron be added at position $\mathbf{x}$. No matter where the electron is inserted it will interact with all of the electrons within the system. To achieve the new ground state, some of the other electrons must move in order to minimise this additional Coulomb energy. The energy saving associated with rearrangement is denoted $W(\mathbf{x})$. This new ground state's Fermi level is equal to or infinitesimally greater than E_F. Before relaxation to this new ground state, the additional electron must have been added at energy $W(\mathbf{x}) > 0$ above the Fermi level. No matter where the electron is inserted, it can never be inserted at the Fermi level. The density of states, therefore, at the Fermi level must be zero.

To find the form of $N(E)$, the argument is made quantitative. To add an electron at site j to the ground state of a system of localised electrons, the additional energy will be

$$M_j = E_j + \sum_{j \neq k} \frac{c}{R_{jk}}. \tag{2.54}$$

Here E_j is the site energy ignoring Coulomb energy, k are the indices of already occupied sites and $c = e^2/4\pi\kappa\epsilon_0$, where κ is the dielectric constant. The M_j values are the effective single particle energy levels, considering Coulomb energy. If, instead of adding an electron, an electron is transferred from site i below the Fermi level to an unoccupied site above the Fermi level, site j, the change in

system energy will be

$$M_j - M_i - \frac{c}{R_{ij}} > 0. \tag{2.55}$$

This inequality will hold for all states where i is below the Fermi level and j is above. Efros and Shklovskii argued that $M_j - M_i \approx \frac{c}{R_{ij}}$. If not, either (2.55) is violated or it is trivially satisfied. By trivially it is meant that the Coulomb energy is negligible and the whole analysis is unnecessary. The distance between two states, separated by energy ϵ around the Fermi level, therefore satisfies

$$r \propto 1/\epsilon. \tag{2.56}$$

Using (2.49) it therefore follows that

$$\left(\int_{E_F}^{E_F+\epsilon} N(E) dE \right)^{-1/d} \propto 1/\epsilon. \tag{2.57}$$

In turn this leads to

$$N(E_F + \epsilon) \propto |\epsilon|^{d-1}. \tag{2.58}$$

This is true for $d > 1$. The dependence is logarithmic for $d = 1$. As anticipated, $N(E_F) = 0$. Note that the Coulomb gap is a soft gap. The density of states is finite at all values except the Fermi energy.

Mott's original analysis can now be applied again, using this modified density of states. The equivalent of (2.51) is now

$$\Gamma_r = \lambda_0 \exp\Big(-2r/\xi - c/(r k_B T) \Big). \tag{2.59}$$

Maximising this rate, in an analagous fashion to the previous variable range hop-

ping analysis, results in an Efros-Shklovskii conductivity of

$$\sigma_{ES} = \sigma_0 \exp\left[-\left(T_0/T\right)^{\frac{1}{2}}\right]. \tag{2.60}$$

Using percolation theory the same temperature dependence is found. Such an analysis results in $T_0 = \beta_d e^2/4\pi\kappa\epsilon_0\xi k_B$, where $\beta_2 \approx 6$ [69, 75]. Significantly, the temperature dependence of Efros-Shklovskii hopping is independent of dimension. Furthermore, in two and three dimensions, conductivity temperature dependences can be used to straightforwardly differentiate between Mott variable range hopping and Efros-Shklovskii hopping.

In [11] such temperature dependences were used to observe transitions from Mott variable range hopping to Efros-Shklovskii hopping as both temperature and carrier density were varied. Due to the sharpening of the Fermi surface, lower temperatures favoured Efros-Shklovskii hopping. Likewise, as carrier density was decreased Efros-Shklovskii hopping was again favoured. Significantly, the pre-factors of the conductivity were quantised. In the MVRH regime $\sigma_0 = 2e^2/h$ and in the ES regime $\sigma_0 = e^2h$. It was suggested that the factor of two difference could be due to spin, whereby in the ES regime the spin degeneracy is lost. The conductivity pre-factor of phonon-assisted hopping is expected to be material dependent and is certainly not predicted to take on a quantised value. The authors suggested that this highly unexpected, and as yet unexplained, behaviour could provide evidence of phononless hopping. Note that in a similar work, [12], the pre-factor within the ES regime took on multiple quantised values. As carrier density was increased the conductivity pre-factor, starting at e^2/h, increased in units of $2e^2/h$.

Finally, see [70] for a transition from nearest neighbour hopping to ES hopping as temperature is decreased. As expected, the ES regime occurs at the lower tem-

peratures when hops of distances greater than those between nearest neighbours are favoured.

2.7 Many-Body Localisation

Many body localised systems are systems which fail to thermalise, that is they fail to reach thermal equilibrium. Anderson himself, in his seminal 1958 paper [1], noted that in a localised system there is no path to equilibrium. The concept of temperature thus breaks down within a many-body localised system. They are also characterised by having zero conductivity at finite temperature. In this sense, they can be considered perfect insulators. Many-body localisation (MBL) can be thought of as the many-body generalisation of the Anderson insulator. Instead of having localisation in real space, one has localisation in the Fock space of the many-body system [17]. See [76, 77] for reviews. This insulating state is fundamentally different to any other insulating state, due to it having zero conductivity at finite temperature. The Mott insulator, for example, is a many-body insulator but has finite conductivity at all finite temperatures. The implication, therefore, is that it will thermalise at any finite temperature.

2.7.1 Eigenstate Thermalisation Hypothesis

What thermalisation means in a quantum system is not as obvious as in a classical system. In an isolated, ergodic and classical system one considers that the system explores all possible available states. All states are regarded as having equal occupation probability. Whether a state is accessible or not depends on a small number of conserved quantities, such as energy and particle number. The collection of these available states is known as the micro-canonical ensemble. The time-averaged observable quantities of the system are thus the averages over this ensemble. However if a quantum system, with Hamiltonian $\hat{H}$, is prepared in an

initial quantum state $|\psi(0)\rangle = \sum_\alpha c_\alpha |\alpha\rangle$ its time evolution is deterministic,

$$|\psi(t)\rangle = \sum_\alpha c_\alpha e^{-iE_\alpha t} |\alpha\rangle , \tag{2.61}$$

where $|\alpha\rangle$ is an eigenstate of $\hat{H}$ with energy E_α. The probability of occupation of an eigenstate $|\alpha\rangle$ is $|c_\alpha|^2$ and is time invariant. To negate the effect of possible thermalisation time, one considers the infinite-time average of an observable quantity with operator $\hat{A}$. This is equal to

$$\lim_{t\to\infty} \frac{1}{t} \int_0^t \langle\psi(t')| \hat{A} |\psi(t')\rangle \, dt' = \sum_\alpha |c_\alpha|^2 \langle\alpha| \hat{A} |\alpha\rangle , \tag{2.62}$$

as terms such as $e^{i(E_\beta - E_\gamma)t} \langle\beta| \hat{A} |\gamma\rangle$, where $\beta \neq \gamma$, average to zero. The reasonable assumption that the system is non-degenerate has been made. Thus such a quantity is also time invariant. The observable quantities of the system are dependent on the initial state of the system. This is apparently at odds with the classical view of thermalisation, whereby, given a small number of conserved quantities, the initial state has no bearing on the state of the system given sufficient time has passed.

The eigenstate thermalisation hypothesis (ETH) aims to resolve this quandary. The term is due to Srednicki [78], building on work by Deutsch [79]. The ETH essentially states that individual eigenstates have observable values equal to the microcanonical ensemble value. That is,

$$\langle\alpha| \hat{A} |\alpha\rangle = \mathcal{A}(E_\alpha), \tag{2.63}$$

where $\mathcal{A}(E)$ is the microcanonical ensemble value of the observable A associated with energy E. It is a requirement of the ETH that $\mathcal{A}(E)$ is a smoothly varying

function of energy. Thus, provided that the initial state of the system is made up of a linear superposition of energy eigenstates which are sufficiently close in energy, observables of the system will evolve in time to their microcanonical expected values. Note that the ETH also contains conditions related to the off-diagonal matrix values, $A_{\beta\gamma} = \langle\beta|\,\hat{A}\,|\gamma\rangle$, which are necessary if one wishes to consider fluctuations and times other than infinite time, [80]. In a many-body localised system, eigenstates break the ETH. In such a system, local pertubations result only in local effects.

2.7.2 BAA Result

Aside from considering the effect on the single-particle density of states and the resultant hopping transport, the discussion regarding disorder and resultant localisation has so far neglected electron-electron interactions. Their inclusion greatly complicates the study of the now many-body system. In 2006 Basko, Aleiner and Altshuler (BAA) considered such a problem [17]. They showed that for a system of weakly interacting electrons, in the absence of coupling to an external bath, with disorder such that the single particle eigenstates are localised, there exists a finite temperature, T_{MBL}, below which the DC conductivity vanishes. Moreover, they also showed that there is finite temperature for which conduction is finite, implying a finite temperature metal-insulator transition. They described the system below T_{MBL} as being Anderson localised in the many-body Fock space. To justify this, they used perturbation theory to show that the probability of a finite escape rate from a given many-body state is zero. Such a system does not thermalise and is considered many-body localised. When coupling to an external bath is added the conductivity becomes non-zero below T_{MBL}. The presence of phonons is thus a major obstacle in searching for experimental realisations of many-body localisation in an electronic system.

2.7.3 Experimental Manifestations

MBL has been reported in ultracold atomic systems, [18, 19]. In both of these works, an optical trap was used to create a periodic lattice. A disordered potential was superimposed on top of this lattice. Using another periodic lattice, of twice the period of the first, the initial state of the many body system was prepared. This was done so that, initially, the atoms occupied every other lattice site of the first periodic lattice. After removing the second periodic lattice, the system was then allowed to evolve. If the disorder was high enough, the system was shown to fail to thermalise. This was done by demonstrating that after sufficient time, there was still an imbalance in occupation of initially occupied and initially unoccupied sites. When disorder was reduced, the imbalance was lost.

MBL is yet to be observed in an electronic system. As previously discussed, the dominant obstacle is that of phonons, which act as an external bath. Ultimately, they will thermalise the system and destroy the MBL phase. As cooling to absolute zero is not possible, phonons can never be completely removed from an experimental system. The phonon induced conductivity will thus be finite below T_{MBL}. However, according to [20], a qualitative signature of the metal-insulator transition can still be identified. Specifically, under application of certain electric fields, two electron temperatures will be stable. This manifests itself as an S-shaped current-voltage characteristic which exhibits hysteretic and discontinous jumps in current when voltage is swept across across the bistable region.

Following the analysis of [20] one can make a self consistent estimate of the electron temperature, T_{el}, by using

$$k_B(T_{el} - T_{ph}) \approx eEL_{ph}(T_{el}), \tag{2.64}$$

and

$$L_{ph}(T_{el})^2 = D(T_{el})\tau_{ph}(T_{el}). \tag{2.65}$$

Here T_{ph} is the phonon temperature and E is the applied electric field. $D(T_{el})$ is the electron diffusion constant, $\tau_{ph}(T_{el})$ is the time taken for an electron to emit a phonon and $L_{ph}(T_{el})$ is the distance travelled in this time. These three quantities are all functions of the electron temperature. The justification for (2.64) is that the difference in electron and phonon temperatures must be balanced by the energy gained from the field between phonon emissions; (2.65) simply states that the mean square of diffusion length is proportional to diffusion time. Figure 2.6, reproduced from [20], shows plots of L_{ph} against T_{el}, at constant T_{ph}. The dotted line is simply due to (2.64) and the continuous lines are possible variations of L_{ph}, given different electron-phonon coupling strengths. At the lowest values of T_{el}, L_{ph} is large due to variable range hopping dominating the transport. It then decreases greatly, as hopping becomes between nearest neighbour sites. As temperature further increases, L_{ph} increases towards a metallic value. Following this, it then decreases due to the higher number of phonon emission events. The lower the phonon coupling strength, the higher the resultant local maximum in L_{ph} is. As can be seen in Fig. 2.6, for high electron-phonon coupling strengths, there will only be one possible self-consistent value of T_{el}, which is very close in value to T_{ph}. However, as the coupling reduces, two further solutions become possible. Only the larger of these two new solutions is stable. If the system finds itself in this state, the electrons can be considered decoupled from the phonon bath.

Another way of deriving the same effect involves an overheating model in which

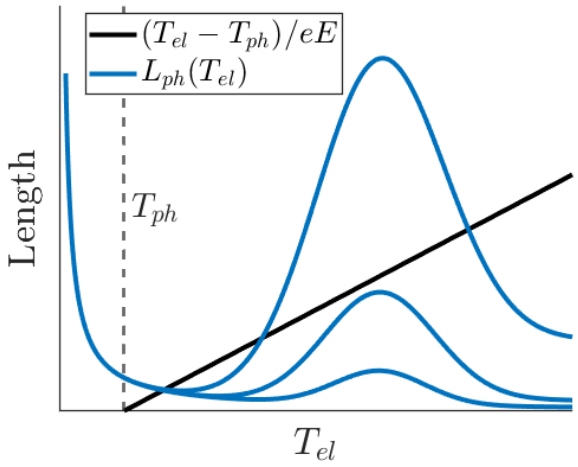

Figure 2.6: Self consistent T_{el} reproduced from [20]. The three blue lines are due to three different electron-phonon coupling strengths.

the power dissipated by a sample when applying a DC bias is considered [21],

$$\frac{V^2}{R(T_{el})} = \frac{\varepsilon(T_{el})}{\tau_{ph}(T_{el})} - \frac{\varepsilon(T_{ph})}{\tau_{ph}(T_{ph})}. \tag{2.66}$$

Here V is the applied bias, $R(T_{el})$ is the resistance of the sample and $\varepsilon(T_{el})$ is the temperature dependent part of the electron system energy. This is a phenomenological equation which is motivated by the fact that the power is zero when the electron system is in thermal equilibrium with the phonon bath and it prevents the electron system being cooled below the phonon temperature. It can be shown, [21, 22], that both ε and τ_{ph} are power law dependent on T_{el} resulting in,

$$\frac{V^2}{R(T_{el})} = \Gamma\Omega(T_{el}^{\beta} - T_{ph}^{\beta}), \tag{2.67}$$

where Γ is the electron-phonon coupling strength and Ω is the area of the sample. Typically, β is expected to be close to five in two dimensions [22]. It has been assumed that the non-linearity in a given sample's current response is explained purely by the increase in electron temperature. Note that a heat balance equation

of the form (2.67) can also be derived due to contact cooling using the Wiedemann–Franz law, in this case $\beta = 2$. Given a temperature dependence of the form

$$R(T_{el}) = R_0 \exp[(T_0/T_{el})^\gamma], \tag{2.68}$$

the applied bias can be expressed as

$$V^2 = R_0 \Gamma \Omega (T_{el}^\beta - T_{ph}^\beta) \exp[(T_0/T_{el})^\gamma]. \tag{2.69}$$

While the right hand side of (2.69) is a monotonic function of T_{el} there will only be one possible solution for T_{el} for any given bias. However when the right hand side becomes non-monotonic in T_{el}, there will exist a range of bias values for which there are three possible solutions for T_{el}. Whether or not this region exists depends on T_{ph}. To find the critical phonon temperature, T_{ph}^c, below which there exists a bistability, the derivitive with respect to T_{el} of the right hand side of (2.69) is set to zero. The largest T_{ph} value for which this is possible is T_{ph}^c. For particular values of β, γ and T_0 it follows that

$$T_{ph}^c = T_0 \left(1 + \frac{\beta}{\gamma}\right)^{-(\frac{1}{\gamma}+\frac{1}{\beta})}. \tag{2.70}$$

Figure 2.7 depicts this analysis. In Fig. 2.7a the right hand side of (2.69) is plotted against T_{el} for various values of T_{ph}. The parameters used are $\gamma = 1$, $T_0 = 10$ K, $\beta = 5$ and $R_0\Gamma\Omega = 1$ V^{2}K^{-5}. When $T_{ph} > T_{ph}^c$ there is only one solution for T_{el} for any given bias. When $T_{ph} < T_{ph}^c$ there are three. The unphysical branch which has electron temperature decrease with an increase in bias voltage is not stable. The $T_{ph} < T_{ph}^c$ plot is also shown in 2.7b. Here the inaccessible region of electron temperature is highlighted. Consider increasing the bias from zero. At a critical bias, $V_c^\uparrow$, the electron temperature will discontinuously and suddenly increase. T_{el}

will jump from around to 1 K to around 3 K. Likewise, when decreasing the bias back down to zero, the electron temperature will suddenly jump down in value at $V_c^{\downarrow}$. These critical voltages are marked in Fig. 2.7b. Note that the jumps occur at different critical voltages and between different temperatures, depending on sweep direction. Ultimately, if there exists a bistability, there exists a region of experimentally inaccessible electron temperatures as well as hysteretic jumps in electron temperature as bias is varied.

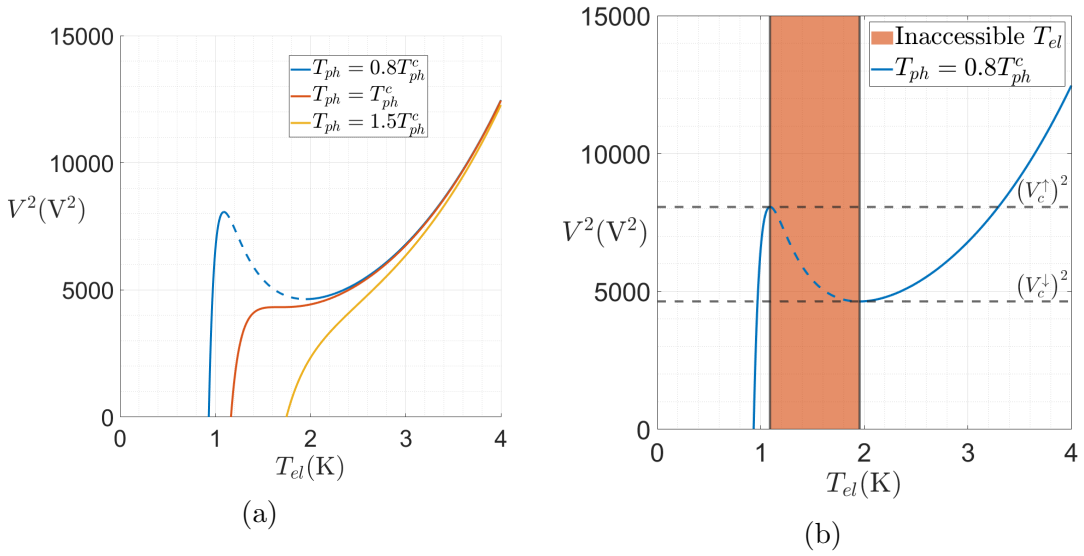

Figure 2.7: Solutions of the overheating model for $\gamma = 1$, $T_0 = 10$ K, $\beta = 5$ and $R_0\Gamma\Omega = 1$ V^{2}K^{-5}. a) Applied bias against electron temperature for three phonon temperatures. Below the critical phonon temperature there exists a bias region in which there are three electron temperature solutions. Only two are stable. The unstable branch is dotted. b) The inaccessible values of electron temperature are highlighted on a plot of bias against electron temperature. The critical bias values are shown.

Figure 2.8a shows how T_{ph}^c varies with γ and β, using (2.70). The ratio of T_{ph}^c to T_0 is higher for Arrhenius resistivity dependences, compared to variable range hopping and Efros-Shklovski hopping. Thus for a given T_0, the bistability is more experimentally accessible if conduction is Arrhenius. Figure 2.8b emphasises the point that if the electron system is on the lower temperature solution branch,

it is very close in temperature to the phonon bath. In this case the electron system and phonons are considered coupled. The higher temperature branch is at much higher temperature than that of the phonons, here the electrons are considered decoupled from the phonons. The specific heat of the electron system is assumed to be larger when decoupled from the phonon system, due to the associated increase in electron temperature.

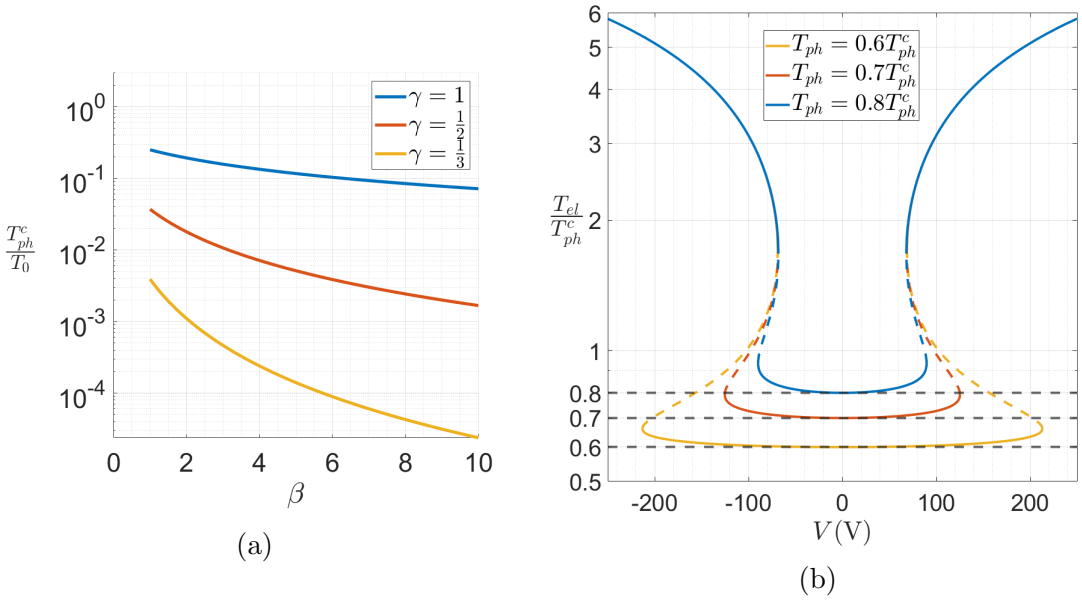

Figure 2.8: a) Critical phonon temperature against β for different values of γ, using (2.70) b) Electron temperature against applied bias. How electron temperature will exhibit jumps is evident. Unstable branches are dotted. Parameters are the same as in Fig. 2.7, $\gamma = 1$, $T_0 = 10$ K, $\beta = 5$ and $R_0\Gamma\Omega = 1$ V^{2}K^{-5}.

Note that, due to the electron temperature being pinned to the phonon temperature within the sample contacts, there will be a non-uniform distribution of electron temperature throughout the sample; electron temperature will be larger further from the sample contacts. As a result of the exponential dependence of sample resistivity on electron temperature, it is possible for the regions closest to the contacts to dominate sample resistance. This can negatively impact measurements which are designed to probe electron-phonon decoupling. Working with large samples, in which the regions of low electron temperature are small

compared to sample size, can help negate the impact of contact cooling.

Just as the electron temperature undergoes hysteretic jumps as applied bias is swept, so does current. This is to be expected given that the resistance, $R(T_{el})$, is a function of electron temperature. This can be explicitly seen by using $I = V/R(T_{el})$ to numerically produce current-voltage characteristics. First, (2.69) is used to produce bias values for given T_{el} values. The associated current values are then produced by dividing these bias values by $R(T_{el})$, given by (2.68). Figure 2.9 depicts such characteristics for various phonon temperatures. The parameters used are $\gamma = 1$, $T_0 = 10$ K, $\beta = 5$ and $R_0\Gamma\Omega = 1$ V^{2}K^{-5}. Figure 2.9a shows characteristics for phonon temperatures both above and below T_{ph}^c. Above this critical temperature the current is a well-behaved singe-valued function of bias voltage. At the critical temperature there exists a voltage for which the derivative of current with respect to voltage diverges. Below the critical temperature there exists a region of bias voltages for which there are three possible current values. The highest and lowest values are stable; the branch of negative differential resistance is not stable. Figure 2.9b shows only characteristics below the critical phonon temperature. Arrows indicate the jumps in current that would be experimentally observed when sweeping the bias voltage. When increasing the bias, the jumps will be from low to high values of current and vice versa when decreasing the bias. Note that the critical voltage, $V_c^{\downarrow}$, at which the current jumps down is largely independent of phonon temperature, whereas the critical voltage at which the current jumps up, $V_c^{\uparrow}$, is heavily dependent on phonon temperature. As discussed, when the electron system is in the high current state its temperature is much greater than that of the phonon system. It thus makes sense that the transition when leaving this state should be largely independent of phonon temperature. However, when the system is in the low current state, the electron temperature is very close to the phonon temperature. Thus it also makes sense

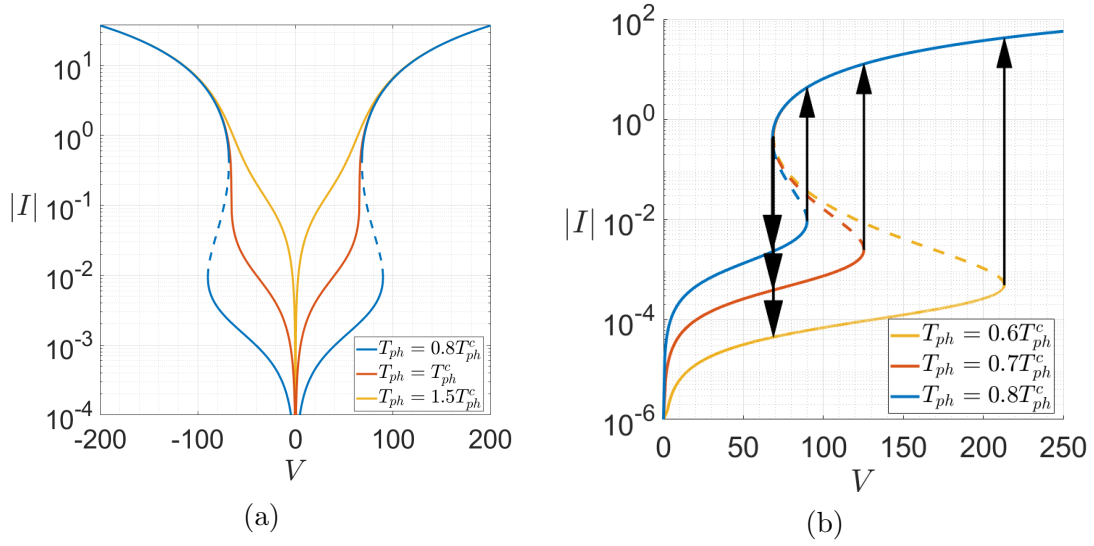

Figure 2.9: Current-voltage characteristics in the overheating model, $\gamma = 1$, $T_0 = 10$ K, $\beta = 5$ and $R_0\Gamma\Omega = 1$ V^{2}K^{-5}. a) Three different phonon temperatures. Unstable branches are dotted. b) Critical voltages are shown. In this case, unlike a), all values of T_{ph} are less than T^c_{ph}.

that the transition out of this state should depend on phonon temperature. This point is emphasised in Fig. 2.10 where critical bias voltages are plotted against phonon temperature. The parameters used here are the same as in Fig. 2.9.

An example of such behaviour can be seen in [81]. Here superconducting indium oxide films were induced into an insulating state using high magnetic fields. Under such conditions the samples displayed large, hysteretic jumps in current as bias voltage was swept. Unlike the down jump critical voltage, the up jump critical voltage was dependent on lattice temperature. The overheating model, (2.67), was successfully applied. The authors also utilised the same material to present evidence of a possible finite temperature insulator [82]. Similar current jumps can be seen in [83–85].

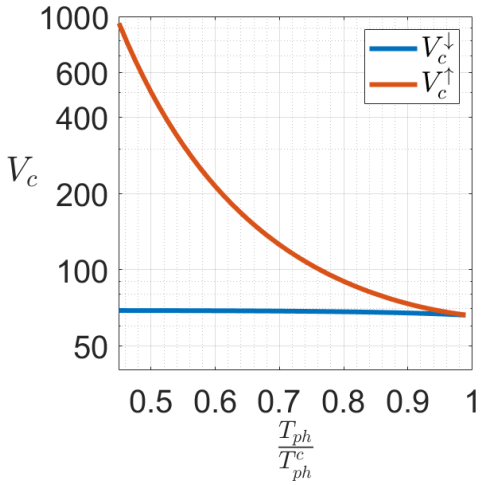

Figure 2.10: Critical voltages against T_{ph}/T_{ph}^c, $\gamma = 1$, $T_0 = 10$ K, $\beta = 5$ and $R_0\Gamma\Omega = 1$ V^{2}K^{-5}.

2.8 The Hall Effect

The Hall effect, discovered in 1879 [86], involves the generation of a Hall voltage under application of a magnetic field. The Hall voltage, V_{xy}, is perpendicular to both current, I, and applied magnetic field. The effect is commonly used to characterise samples, in particular to determine carrier densities. In two dimensions, it can be shown that the Hall resistance, $R_{xy} = V_{xy}/I$, is given by

$$R_{xy} = \frac{B}{ne}, \tag{2.71}$$

where B is the magnetic field perpendicular to the plane of transport and n is the two dimensional carrier density. A simple derivation involves the Drude model, itself discussed in section 2.2, whereby all electrons move with mean drift velocity v, so that the current is $envW$. Here W is the width of the sample, assuming a simple Hall bar geometry. The classical Lorentz force on each electron is Bev. The set up is demonstrated in Fig. 2.11. The argument goes that an equal and opposite force is required to cancel the Lorentz force, which is perpendicular to

current flow. An electric field of Bv in this direction, and thus a Hall voltage of BvW, will do just this. Dividing the Hall voltage by the current, the Hall resistance of (2.71) follows. One can then simply measure this resistance to find the carrier density. Typically one measures the Hall resistance as a function of field, with the slope being equal to the Hall coefficient,

$$R_H = \frac{1}{ne}. \tag{2.72}$$

The carrier density is then,

$$n = \frac{1}{eR_H}, \tag{2.73}$$

while the mobility, $\mu = \sigma/ne$, is

$$\mu = \sigma R_H. \tag{2.74}$$

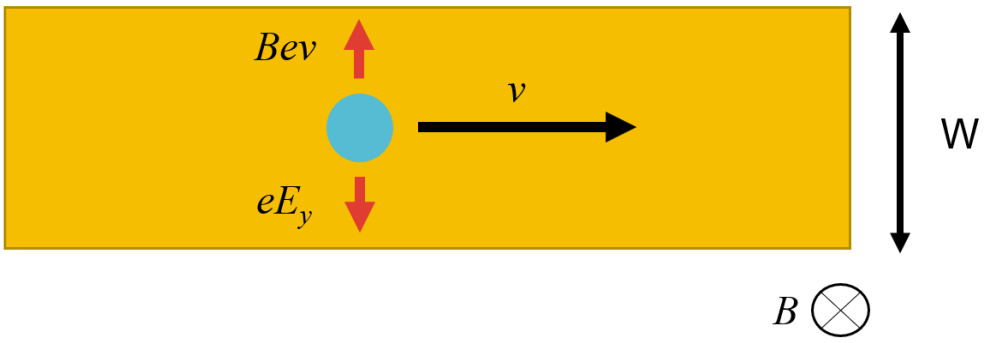

Figure 2.11: Schematic depicting the Hall effect.

2.8.1 Hopping and the Hall Effect

An accepted model describing the Hall effect in which the transport mechanism is that of hopping does not exist. It is common for proposed models to assume that hopping is a phase-coherent process. Such models consider the interference between the various different paths, between localised sites. The change

in phase acquired by a path due to the magnetic vector potential is central to these models. It was Holstein who first introduced such ideas [87]. In [88], these ideas were built on and a percolation approach was considered. In the case of three dimensional Mott variable range hopping, meaning that conductivity has the form $\sigma = \sigma_0 \exp\left[-(T_0/T)^{1/4}\right]$, a Hall mobility of the same form was derived. However the value of T_0 was shown to be less than that of the conductivity, by approximately a factor of three. In [89] a similar theoretical relationship between the Hall mobility and conductivity was found. In this instance, Efros-Shklovski hopping was considered, meaning $\sigma = \sigma_0 \exp\left[-(T_0/T)^{1/2}\right]$. Here the value of T_0 associated with the Hall mobility was altered by a factor of 0.09, when compared to the conductivity T_0. Also in this work, experimental results were compared to the derived theory. A Ge/Si quantum dot array which demonstrated Efros-Shklovski hopping was used. The experimental ratio of the two characteristic temperatures was found to be $T_0^{\mu}/T_0^{\sigma} = 0.31$. Further experimental work, involving Efros-Shklovski hopping hosted in reduced graphene oxide, found a ratio of 0.49 [90]. In contrast, the Hall constant, $R_H = R_{xy}/B$, is predicted to exhibit a non-monotonic dependence on temperature in the Mott variable range hopping regime in [91]. At high temperatures, $R_H \sim \sqrt{T}$, while for low temperatures, $R_H \sim T\exp(T_0/T)$. Experimental temperature dependences of R_H were also considered and compared to the theory in [91]. However, the material used was doped bulk ZnO. This meant that in addition to conduction via hopping, the transport also included conduction within the conduction band. The case for the so-called double sign anomaly has been argued by others. In this case, electrons can have a positive Hall constant when hopping and holes can have negative [92].

It is important to note that all of the aforementioned works make the assumption that hopping is a phase coherent process. The evidence in support of this is, however, limited. See [93] for potential evidence in the Mott variable range

hopping regime hosted in PbTe antidots. Specifically, Altshuler-Aronov-Spivak (AAS) oscillations are claimed. It is therefore argued that phase is retained over a considerable distance.

It can instead be assumed that hopping is an incoherent process. If this is done, in the case of transport being via both hopping and activation to a mobility edge, a compensated Hall effect is predicted. Carriers in extended states experience a Lorentz force, while the magnetic field has negligible impact directly on the localised carriers. This leads to a reduced Hall voltage, relative to purely extended state transport, in order to compensate for the effect of the Hall voltage itself on the localised carriers. A detailed discussion and experimental comparison is given in [94]. The case of purely hopping transport is, however, not considered.

2.8.2 Integer Quantum Hall Effect

At higher magnetic fields, the classical treatment of the Hall effect presented at the beginning of this section is no longer applicable and a quantum mechanical treatment is necessary. The striking result is that the reciprocal of the Hall resistance is quantised in units of e^2/h. Furthermore, the longitudinal resistance along the edge of the sample, R_{xx}, drops to zero. This is shown in Fig. 2.12. As shall be discussed, disorder is crucial to the existence of the quantum Hall effect. The first observation of the effect is presented in [24].

A derivation of the quantum Hall effect is now given. Aside from the magnetic field, the electrons are initially considered as being in free space. Disorder, which will prove crucial, will be added later. Spin is also initially ignored. Electron-electron interactions will not be considered, but are discussed in appendix D, which covers the fractional quantum Hall effect. The single particle Hamiltonian is,

$$\hat{H} = \frac{1}{2m}(\hat{\mathbf{p}} + e\mathbf{A})^2, \tag{2.75}$$

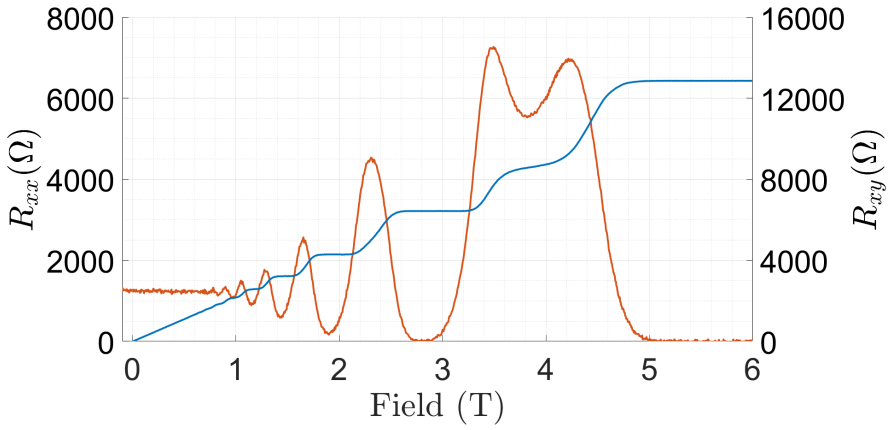

Figure 2.12: The integer quantum Hall effect.

where $\hat{\mathbf{p}}$ is the two-dimensional single particle momentum operator and $\mathbf{A}$ is the magnetic vector potential. Electrons are constrained to the x-y plane, meaning that the perpendicular magnetic field, $\mathbf{B}$, is $(0, 0, B)$. The Landau gauge is used, meaning that

$$\mathbf{A} = (0, Bx, 0). \tag{2.76}$$

The Schrödinger equation in the position basis is therefore,

$$\frac{1}{2m}\left[-\hbar^2\frac{\partial^2}{\partial x^2} + (-i\hbar\frac{\partial}{\partial y} + eBx)^2\right]\psi(x,y) = E\psi(x,y) \tag{2.77}$$

where $\psi(x, y)$ is the single electron wavefunction. Using a trial wavefunction $\psi(x, y) = \exp(ik_y y)\phi(x)$ this can be written as

$$\left[-\frac{\hbar^2}{2m}\frac{\partial^2}{\partial x^2} + \frac{e^2B^2}{2m}(\frac{\hbar k_y}{eB} + x)^2\right]\phi(x) = E\phi(x). \tag{2.78}$$

This is just the Schrödinger equation for a one-dimensional simple harmonic oscillator centred on $x = -\hbar k_y/eB$ with angular frequency $\omega_B = eB/m$. Letting $f_{k_y,n}(x)$ be the nth lowest energy wavefucntion of such a one dimensional oscillator, the wavefunctions and associated energies of the original Schrödinger equation

(2.77) are

$$\psi_{k_y,n}(x,y) = \exp(ik_y y) f_{k_y,n}(x) \tag{2.79}$$

and

$$E_{k_y,n} = \hbar\omega_B(n + \frac{1}{2}) \tag{2.80}$$

respectively. Note that the energies do not depend on k_y. States which have the same n are said to be in the same Landau level and, ignoring edge effects for now, all have the same energy. Landau levels are separated by the cyclotron energy, $E_c = \hbar eB/m$. By considering a two-dimensional sample of length L_x in the x direction and L_y in the y direction, the capacity of each Landau level can be found. A state with a given k_y will have its wavefunction centred on $x = -\hbar k_y/eB$. Hence the upper and lower bounds on k_y are $\pm eBL_x/2\hbar$, else states will be centred outside of the sample. The possible values of k_y are evenly spaced with separation of $2\pi/L_y$. Thus the number of states in a given Landau level is simply $(eBL_x/\hbar)/(2\pi/L_y) = eBA/h$. This is the magnetic flux through the rectangle divided by the magnetic flux quanta.

Spin is now considered. This involves adding a Zeeman energy term to the Hamiltonian. Each Landau level is simply split into two Landau levels, each with the same number of states as the original. The number of states in a given Landau level stays the same. The energy difference between two spin-split Landau levels is the Zeeman energy, E_z.

The filling factor, ν, is defined as the number of electrons in the system divided by the capacity of a single Landau level. Thus

$$\nu = \frac{nh}{eB}, \tag{2.81}$$

where n is the number of electrons per unit area. When ν is an integer, exactly ν

Landau levels are fully occupied.

Edge effects are now considered. Recall that a state with wavevector k_y will have its wavefunction centred on $x = -\hbar k_y/eB$. The states centred on x values near the edge of the sample have their energies increased as their effective one dimensional potential is tightened as a result of their proximity to the edge. This removes the degeneracy within a given Landau level and there will be an unusual dispersion relation in k_y, as shown in the schematic of Fig. 2.13a. The associated velocity dependence, given by $v_y = \frac{1}{\hbar}\frac{\partial E(k_y)}{\partial k_y}$, is shown in Fig. 2.13b. Note that one could replace k_y with $\pm x$ in both of these schematics, depending on the sign of B, where x is the central point of each wave function in the x direction. There is a clear chirality to the system. The wavefunctions on opposite sides of the sample have velocities in opposing directions. This is only possible due to the lack of time-reversal symmetry, as discussed in section 2.3.

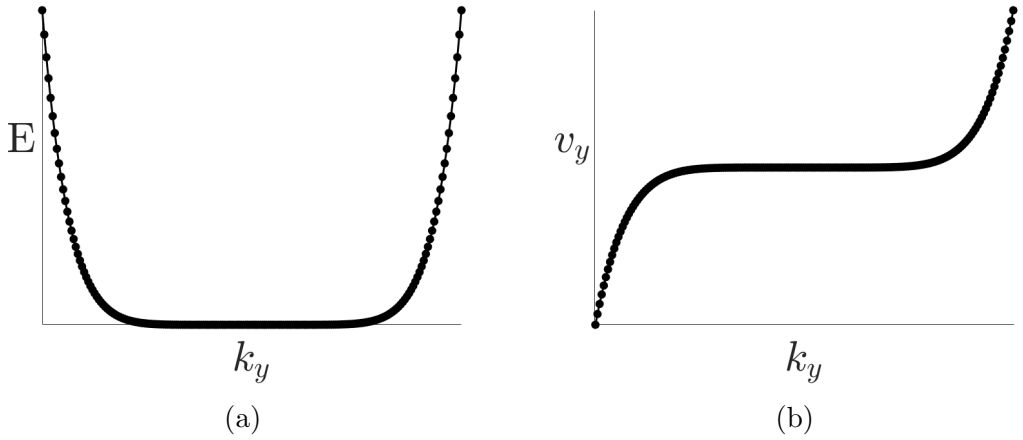

Figure 2.13: a) Schematic of a dispersion relation of a single Landau level, ignoring disorder but including edge effects. b) Velocity in the y direction, given the dispersion relation of a). In both a) and b), k_y is interchangeable with x.

The states considered so far have all been extended states. They are plane wave states in the y direction and extend along the length of the sample. With disorder added to the system, many of these states will become localised around

local maxima or minima of the random potential. The extended states at the edges of the sample, known as edge states, will in the main remain extended due to the local potential associated with the sample edge dominating the disorder potential. The large number of these localised states will, crucially, pin the Fermi level between Landau levels meaning that almost regardless of filling factor the Fermi level should be within the edge states. The density of states of the quantum Hall system is shown in Fig. 2.14. The Zeeman energy and cyclotron energy splittings are shown. Edge states are not shown.

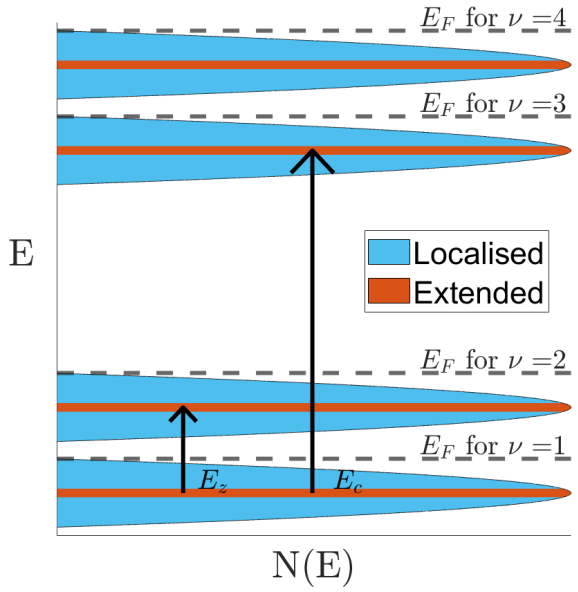

Figure 2.14: Landau level density of states. Cyclotron energy, E_c, and Zeeman energy, E_z, are labelled. The Fermi level, E_F, for different filling factors, ν, is also shown. Edge states are not shown.

Consider a current flowing along the sample edge in the y direction. If the Fermi level is between two Landau levels, meaning it is within the extended edge states, the voltage along the edge of the sample will be zero. Scattering between edge states is irrelevant as any scattering will be into another chiral edge state moving in the same direction. There is thus no voltage drop between two voltage probes along the sample edge. Conduction is ballistic along the edges of the

sample. This explains the longitudinal resistance falling to zero when the Fermi level is between Landau levels.

Consider next the Hall voltage, V_{xy}. As the edge states on either side of the sample are chiral, one side must be at a higher chemical potential than the other. The chemical potentials on either side are denoted μ_L and μ_R. Only then is a net flow of current possible, as otherwise the current contribution from one side will cancel the other. Still assuming that the Fermi level is between two Landau levels, and thus within the extended edge states, the current at zero temperature is given by

$$I = \sum_{LL} \int e v_y(k_y) g(k_y) dk_y \tag{2.82}$$

where the sum is over filled Landau levels and the integral over all states below the local chemical potential. Figure 2.15 displays a schematic of two Landau levels where the states contributing to the current integral are represented by filled black circles. The density of states in k_y space, per unit length, is denoted by $g(k_y)$ and is equal to $1/2\pi$. Using this and the fact that $v_y = \frac{1}{\hbar}\frac{\partial E(k_y)}{\partial k_y}$, (2.82) can be rewritten as

$$I = \frac{e}{\hbar} \sum_{LL} \int \frac{\partial E(k_y)}{\partial k_y} \frac{1}{2\pi} dk_y = \frac{e}{h} \sum_{LL} \int_{\mu_R}^{\mu_L} dE = M \frac{e^2}{h} V_{xy} \tag{2.83}$$

where the Hall voltage, V_{xy}, is equal to $(\mu_L - \mu_R)/e$ and M is the number of filled Landau levels. Thus the Hall resistance, V_{xy}/I, is equal to

$$R_{xy} = \frac{1}{M} \frac{h}{e^2} \tag{2.84}$$

when the chemical potential is between the M and $M+1$ Landau levels. The fact that localised states pin the Fermi level between Landau levels explains the precise quantisation in Hall resistance. Remarkably, it is disorder that is necessary for this precise quantisation. As either chemical potential or magnetic field are

varied, very well defined jumps in Hall resistance will be observed as the number of filled Landau levels changes.

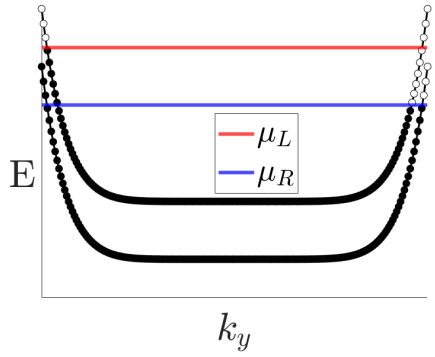

Figure 2.15: Schematic to aid the calculation of current. Note that k_y is interchangeable with x. Only two Landau levels are shown for simplicity. The chemical potential differs on either side of the sample. V_{xy} is given by $(\mu_L - \mu_R)/e$. Note that disordered states have been excluded for simplicity, but it is these states that pin the Fermi level between Landau levels. The filled black circles represent states that are below the local chemical potential and only they contribute to the current integral at zero temperature.

Finally, for completeness, the first explanation of the effect is discussed [95]. Laughlin considered a Corbino ring geometry and used a pumping argument. The gauge is chosen such that the obvious solutions are extended states that wrap around the ring. Each eigenstate is centred on a particular radius. If a flux, which is not related to the magnetic field the electrons are in, is varied through the ring then the single particle eigenstates will shift radius and map onto one another with period h/e. Thus for each filled Landau level, when the flux is varied by h/e, it is as if one electron has moved between the outer and inner radius of the ring. The direction depends on the sign of the change in flux. The variation of the flux induces a voltage around the ring. If it takes time T and happens at a constant rate the induced voltage is just h/Te. As each Landau level pumps one electron across the ring, the current is equal to Me/T where M is the number of filled Landau levels. Thus the Hall resistance is again given by (2.84). The same

disorder argument ensures the Fermi level is always within extended edge states.

2.8.3 Breakdown of the Quantum Hall Effect

The breakdown of the quantum Hall effect is commonly defined as the onset of a finite longitudinal resistance, R_{xx}, measured along the edge of a sample, due to the applied current exceeding a critical value. This occurs while the filling factor, ν, is an integer. At the same time, the Hall resistance, R_{xy}, deviates from its quantised value of $h/\nu e^2$. See [96–100] for experimental works. A review is presented in [23]. The breakdown is typically reported as being sharp. In [97], the longitudinal voltage is described as increasing by a factor of 10^4 when the current is increased by less than 1%, at the critical current. Various models have been proposed based on mechanisms such as intra-Landau level transitions [101] and inter-Landau level transitions [102].

However, the sudden fall in two terminal resistance, when measuring in a Corbino geometry, is also referred to as the breakdown of the quantum Hall effect [97, 103, 104]. In such a geometry, conduction is via the bulk localised sites of the disorder broadened Landau levels. Edge states are avoided. In fact, it is argued in [104] that the breakdown is a bulk state phenomenon and a Corbino geometry is necessary to study the effect. It is not a given that the breakdown described in the standard Hall geometry, in which conduction is via ballistic edge states, has the same physical reasoning as the effect described in the Corbino geometry. In any case, the physical reasoning behind the breakdown of the quantum Hall effect is disputed.

In [103], large jumps in current of four orders of magnitude, with $\nu = 4$, were observed as applied bias was varied, using a Corbino geometry. Hysteresis and temperature dependence were not investigated, but the presented current-voltage characteristics are reminiscent of those discussed in section 2.7.3. Phenomeno-

logical descriptions involving electron overheating have been proposed, [105, 106]. In these experimental works standard Hall bar geometries were used and plots of diagonal conductivity, σ_{xx}, against Hall field, E_y, produced S-shaped curves at the lowest measured temperatures. Here E_y was essentially used in place of current. Fittings were made using a similar phenomenological heat balance model to (2.67). In this case, the power per unit area was given by $\sigma_{xx}E_y^2$. This is a reasonable assumption for a homogeneous material in which $|E_y| >> |E_x|$. However, in the quantum Hall regime the conductivity is not homogeneous. There are both ballistic edge states and bulk localised states. The suitability of applying such a model to the values of E_y and σ_{xx} derived from resistance measurements using a Hall bar geometry is not obvious. The authors of both works noted significant issues when fitting to the heat balance model. Significantly, a systematic test of the overheating model (2.67), in a quantum Hall system using a Corbino geometry is absent from the literature. Such work will be presented in chapter 7.

The possibility of electron avalanche in the Corbino geometry was investigated in [104]. This was done by analysing current noise. Specifically the Fano factor, F, was estimated. For a counting process this is defined as the ratio of the variance of the quantity being counted to its mean. For a Poisson process in which there is no correlation between events being counted, $F = 1$. When discussing transport measurements, the quantity being counted is typically the number of electrons entering a current drain. If the electrons can be described as bunching, then $F > 1$. In a standard diffusive system $F < 1$ due to the Pauli exclusion principle. In [104] the Fano factor was shown to become very large in the breakdown regime. This was provided as evidence of electron avalanche. That is, electrons ionise each other resulting in a cascade effect. If true, this would not be at odds with a heating model but instead indicates what is happening at a microscopic level.

Chapter 3

Materials

In this chapter the two materials used in this work, GaAs/$Al_xGa_{1-x}As$ heterostructures and graphene, are introduced. Their basic properties are first presented before a discussion covering how disorder can be systematically introduced into both systems is given.

3.1 GaAs/$Al_xGa_{1-x}As$ Heterostructures

A heterostructure is simply multiple layers of different semiconductors. The boundary between two different layers is known as a heterojunction and these interfaces are typically the areas of interest within the structure. The practice of varying layer composition and depth is known as band structure engineering. Here the aim is to control the band structure which will ultimately determine where the electrons, or holes, will reside. The heterostructures in this work were grown by molecular beam epitaxy (MBE) and were composed of multiple layers of $Al_xGa_{1-x}As$, with the molar fraction x varying from layer to layer. Upon cooling samples down to cryogenic temperatures, a single two-dimensional electron gas (2DEG) was formed. It was these 2DEGs that were investigated, typically after manipulating the Fermi level below a mobility edge in some way.

3.1.1 GaAs, AlAs and $Al_xGa_{1-x}As$

Gallium arsenide is a direct band gap semiconductor with a band gap of 1.42 eV. It has a crystal structure known as zinc blende. This means it has a face-centred cubic (fcc) lattice with a two atom basis. Due to translational invariance one atom, either gallium or arsenic, is at (0,0,0) while the other is at $(\frac{1}{4},\frac{1}{4},\frac{1}{4})$. The crystal structure is shown in Fig. 3.1, taken from [107]. The lattice constant, the length of one side of the conventional fcc unit cell, is 5.65 Å.

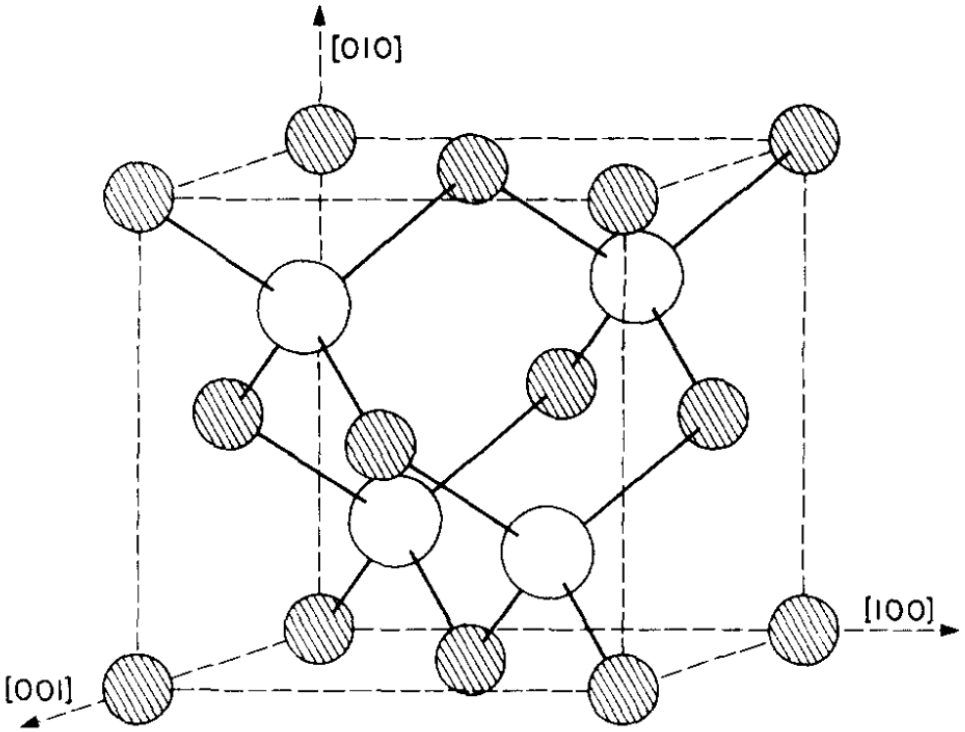

Figure 3.1: The crystal structure of both GaAs and AlAs, known as zinc blende. The conventional face-centred cubic unit cell is shown, which contains four primitive unit cells. Taken from [107].

Aluminium arsenide, whilst also having a zinc blende crystal structure, is an indirect band hap semiconductor. Its lattice constant is 5.66 Å, which is very close to that of gallium arsenide. This lattice matching of the two compounds is very useful when growing heterostructures as the strain at the various interfaces

between layers is minimised.

$Al_xGa_{1-x}As$ is an alloy of gallium arsenide and aluminium arsenide. Arsenic atoms sit on the same sites that they would have done in galium arsenide and aluminium arsenide. Gallium and aluminium atoms are distributed randomly over the sites they would have occupied in galium arsenide and aluminium arsenide respectively. The fraction of aluminium atoms distributed over these sites is given by x, while the fraction of gallium atoms is $1-x$. If one were to label gallium and aluminium atoms as being the same, one would again see a zinc blende crystal structure.

Key properties of $Al_xGa_{1-x}As$ can be described as a function of the molar fraction, x. The lattice constant, a, can be linearly interpolated between the gallium arsenide lattice constant and the aluminium arsenide lattice constant. It can be written in units of Å as,

$$a = 5.6533 + 0.0078x.$$

The band gap, E_g, can be expressed in units of eV as,

$$E_g = \begin{cases} 1.424 + 1.247x, & \text{if } x < 0.45 \\ 1.900 + 0.125x + 0.143x^2, & \text{if } x > 0.45. \end{cases}$$

For $x < 0.45$, the band gap is direct and takes place at the Γ point in the Brillouin zone, which is the centre point of the Brillouin zone. However, for $x > 0.45$ the lowest energy point in the conduction band changes from Γ to X. The band gap thus becomes indirect. This is depicted in Fig. 3.2, taken from [108].

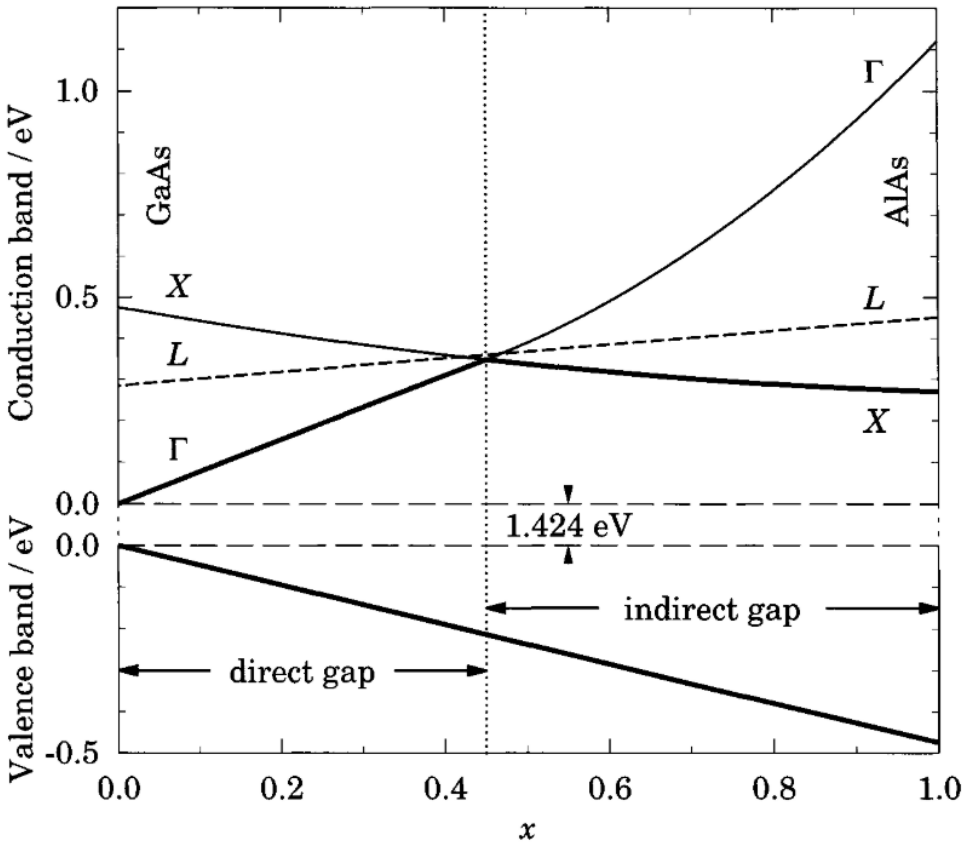

Figure 3.2: The valance band and conduction band energies of $Al_xGa_{1-x}As$ as a function of x. For $x < 0.45$ the band gap is direct and is at the centre of the Brilloin zone, the Γ point. However, for $x > 0.45$ the conduction band minimum is at the X point in the Brilloin zone and the gap becomes indirect. Taken from [108].

3.1.2 Molecular Beam Epitaxy

The heterostructures in this work were grown using molecular beam epitaxy, by Dr. Chong Chen in the Cavendish Laboratory at the University of Cambridge. MBE is a growth technique in which material is evaporated at ultra high vacuum, typically considered as being 5×10^{-11} mbar or lower, onto a substrate. The substrates used in this work were all gallium arsenide. At such low pressures the mean free path is longer than the distance from the cell, where the material is vaporised, to the substrate. This means that the growth material travels ballis-

tically, rather than diffusing. Growth is slow, it can be around one monolayer per second, which allows for sharp heterojunctions and accurate control of layer thicknesses [108].

3.1.3 The Two-Dimensional Electron Gas

Heterostructures were grown in order to form a two-dimensional electron gas (2DEG) at a GaAs/$Al_{0.33}Ga_{0.67}As$ interface, with the majority of the 2DEG resident in the GaAs side of the boundary. The interfaces were always 90 nm below the surface of the wafer. At such depths, control of the 2DEG using a surface gate is typically straightforward. Figure 3.3a shows a schematic of a typical wafer structure while Fig. 3.3b shows the associated band structure, calculated numerically using the Matlab programme Aquila [109]. To see how such a wafer results in such a band structure first consider the divergence of the electric field,

$$\nabla \cdot \mathbf{E} = \frac{\rho}{\epsilon_0}, \tag{3.1}$$

where $\mathbf{E}$ is electric field and ρ is charge density. Both unoccupied dopant sites and electrons in the conduction band contribute to ρ. Using $\mathbf{E} = -\nabla\phi$, where ϕ is the electrostatic potential,

$$\frac{\partial^2\phi}{\partial z^2} = -\frac{\rho}{\epsilon_0}. \tag{3.2}$$

Here convention has been followed that the direction of growth is in the z direction and it has been assumed that the only variation in ϕ is in this dimension. As the electrostatic energy of an electron is $-e\phi$, (3.2) can be used to find the electrostatic contribution to the band structure. To solve for the conduction band, all that must be done is ensure that (3.2) is satisfied and that it jumps by the appropriate band energy differences at each heterojunction, as can be seen in Fig. 3.2. Using (3.2), it is seen that the curvature of the band structure at a given point is proportional to

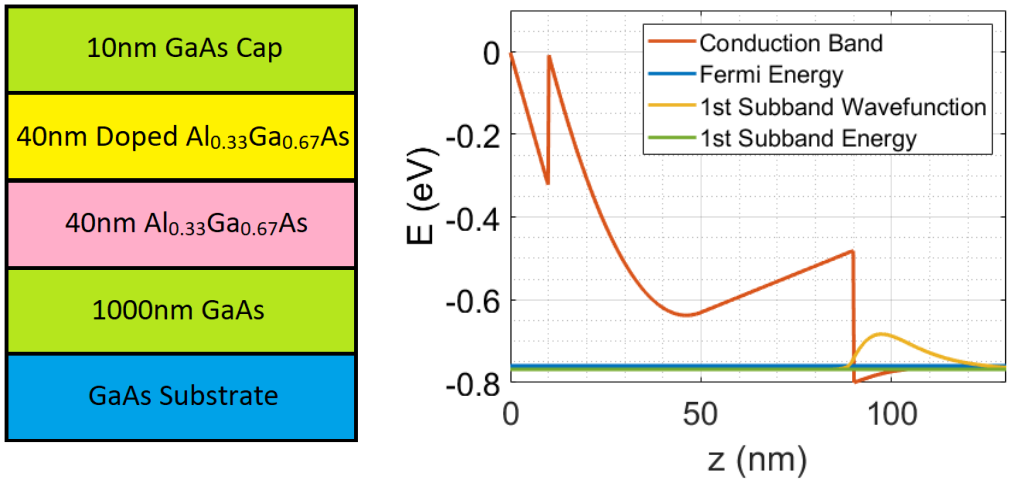

(a) (b)

Figure 3.3: a) Schematic of a GaAs/$Al_xGa_{1-x}As$ wafer grown by molecular beam epitaxy. The two-dimensional electron gas will form at the interface between the spacer layer (pink) and buffer layer (green). b) Conduction band simulation, produced using the Matlab programme Aquila [109]. The top of the GaAs cap corresponds to $z = 0$, while z increases moving down into the wafer. The red conduction band changes gradient wherever there is a non zero charge density, as a consequence of Poisson's equation. It also exhibits abrupt changes when the local material changes. The lowest energy subband wavefunction in shown in yellow while its energy is shown as a horizontal green line. This energy is less than the Fermi energy, shown in blue. All other subbands have energies higher than the Fermi energy and thus will not be occupied at low temperatures.

the charge density at that point. Negative charge causes the band to have negative curvature, while positive charge leads to positive curvature. Also note that (3.2) is a second order differential equation. It requires two boundary conditions. A typical boundary condition is that the electric field is zero deep into the substrate. This means the band should be flat, meaning $\partial\phi/\partial z = 0$. To numerically solve for ϕ, a simple initial value problem solver can be used. Deep in the substrate ϕ is set to an arbitrary constant, which is free to be changed later, and $\partial\phi/\partial z$ is set equal to zero. Once can then integrate along z, using ρ to dictate how much $\partial\phi/\partial z$ should vary at each point in space and ultimately find $\phi(z)$. Then the second boundary condition can be imposed. At a metal and semiconductor

junction, the difference in energy between the chemical potential of the metal and the conduction band energy of the semiconductor is known as the Schottky barrier. Assuming a metal has been deposited onto the surface of the wafer in order to form a gate, discussed in section 4.6, one can simply use the Schottky barrier as the second boundary condition. These values are well documented for GaAs. The band structure is thus shifted in energy so that the difference between the conduction band energy at the top of the wafer and the chemical potential equals the required Schottky barrier. For GaAs this is typically around $0.7eV$ [108]. For a given charge distribution, $\rho(z)$, this band structure satisfies (3.2) and matches the necessary boundary conditions. The one dimensional eigenstates, known as subbands, and eigenenergies of this conduction band are then found. Given an effective mass m^*, the energy of a state comprising of the ith subband and two-dimensional wavevector $\mathbf{k}$ in the $x-y$ plane is,

$$E_i(\mathbf{k}) = \epsilon_i + \frac{\hbar^2|\mathbf{k}|^2}{2m^*}, \tag{3.3}$$

where ϵ_i is the energy of the ith subband. The probability the state will be occupied is found using the Fermi-Dirac distribution. One could assume zero temperature and all states below the chemical potential will be occupied whilst all above will be unoccupied. This information and the spatial distribution of the subband wave functions in z are used to modify the charge density, $\rho(z)$. The electrostatic potential, ϕ, is solved for again which will lead to a new band structure meaning new eigenstates, new eigenenergies and thus a new charge density. This cyle of solving the Poisson equation and then the Schrödinger equation is continued, until ϕ and ρ are self-consistent. Once this is done, the band structure, the energies of the subbands, their spatial distribution and how may electrons they contain are known. If only one subband is occupied, as is the case with the example shown

in Fig. 3.3b, the system simply comprises of a 2DEG in the $x - y$ plane.

Each layer in turn from Fig. 3.3a is now briefly discussed. The bottom layer is the substrate, this is simply the material that MBE growth takes place on. Above this is a GaAs buffer layer. The purpose of this layer is to put distance between the 2DEG and impurities in the substrate. Next is an $Al_{0.33}Ga_{0.67}As$ spacer layer. The 2DEG forms at the interface of the GaAs and $Al_{0.33}Ga_{0.67}As$ layers. The thickness of the 40 nm spacer layer is to put distance between the 2DEG and the ions present as a result of doping in the doped layer. These ions result in scattering and reduce the quality of the transport within the 2DEG. Without this doped $Al_{0.33}Ga_{0.67}As$ layer the 2DEG would not be occupied. Finally, there is a GaAs cap to prevent oxidation of the $Al_{0.33}Ga_{0.67}As$ layer.

Once the wafer is grown, further fabrication takes place in order to allow one to probe the 2DEG. This processing is discussed in section 4.6, while the measurements themselves are discussed in section 5.2.

3.2 Graphene Heterostructures

3.2.1 Monolayer Graphene

Monolayer graphene is a two-dimensional, zero band gap semi-metal and was first experimentally observed in 2004 [110]. Graphene has extraordinary electronic and mechanical properties. In particular, a Young's modulus close to 1 TPa, a room temperature mobility of 2 $\times 10^5$ $cm^2V^{-1}s^{-1}$ and a thermal conductivity close to 3000 WmK^{-1} have been demonstrated [111–114]. There is thus much expectation with regard to graphene's commercial and industrial potential, for example in flexible electronics, transparent barrier films and energy storage [115].

Graphene is formed of carbon atoms in a honeycomb lattice. The lattice

vectors, $\mathbf{a_1}$ and $\mathbf{a_2}$, can be expressed as,

$$\mathbf{a_1} = \frac{a}{2}(3, \sqrt{3}), \qquad \mathbf{a_2} = \frac{a}{2}(3, -\sqrt{3}),$$

where a is the distance between nearest-neighbour carbon atoms and is equal to 1.42 Å. The basis contains two carbon atoms. The reciprocal lattive vectors, $\mathbf{b_1}$ and $\mathbf{b_2}$, are

$$\mathbf{b_1} = \frac{2\pi}{3a}(1, \sqrt{3}), \qquad \mathbf{b_2} = \frac{2\pi}{3a}(1, -\sqrt{3}).$$

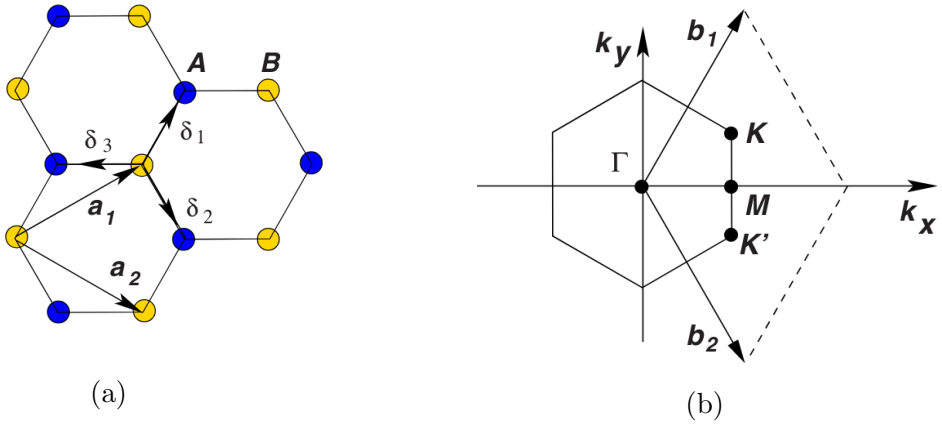

(a) (b)

Figure 3.4: a) The crystal structure of graphene. Lattice vectors are $\mathbf{a_1}$ and $\mathbf{a_2}$. The basis contains two carbon atoms. Taken from [116]. b) The reciprocal lattice. Reciprocal lattice vectors are $\mathbf{b_1}$ and $\mathbf{b_2}$. The first Brillouin zone is shown. Dirac points are at $\mathbf{K}$ and $\mathbf{K'}$. Taken from [116].

The crystal structure is shown in Fig. 3.4a while the reciprocal lattice and first Brillouin zone are shown in Fig. 3.4b, taken from [116]. Using a tight binding model, which allows jumps between nearest neighbour and next nearest neighbour carbon atoms, the following dispersion relation is found,

$$E(\mathbf{k}) = \pm t\sqrt{3 + f(\mathbf{k})} - t' f(\mathbf{k}), \tag{3.4}$$

where the plus and minus signs apply to the upper and lower bands respectively, t is the nearest neighbour hopping energy, t' is the next nearest neighbour hopping energy and

$$f(\mathbf{k}) = 2\cos(\sqrt{3}k_y a) + 4\cos(\frac{\sqrt{3}}{2}k_y a)\cos(\frac{3}{2}k_x a). \tag{3.5}$$

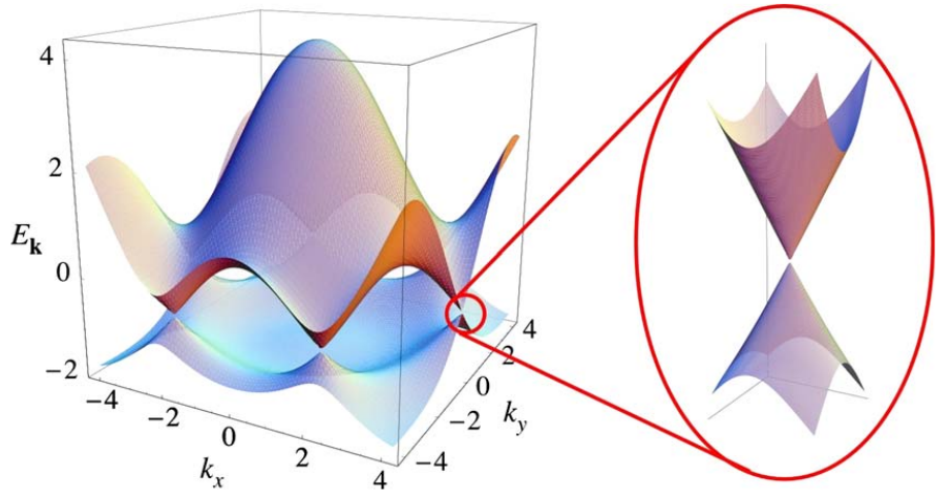

Figure 3.5: The dispersion relation of graphene, using the tight binding model and plotted in units of t. In this instance $t = 2.7$ eV and $t' = -0.2$ eV. The dispersion is linear around the Dirac points, shown in the blown up image. Taken from [116].

The dispersion relation is shown in Fig. 3.5, taken from [116]. Around a Dirac point, **K**, the dispersion relation is linear,

$$E(\mathbf{K} + \mathbf{q}) \approx \nu_F|\mathbf{q}| + O[(\mathbf{q}/\mathbf{K})^2], \tag{3.6}$$

where $\nu_F = 3ta/2$ is the Fermi velocity and is independent of energy and momentum. This linear dispersion relation was predicted in 1947 by Wallace [117], who analysed the band structure of graphite in general, as well as a single layer. This was over half a century before such a single layer, now known as graphene, was

experimentally observed.

3.2.2 Hexagonal Boron Nitride

Hexagonal boron nitride (h-BN) is a large band gap (5.9 eV) semiconductor. Like graphene, it is atomically flat and also has a honeycomb lattice. Its lattice constant is 2.50 Å, which is similar to that of graphene, 2.46Å. Given that it acts an insulator, due to its large band gap, h-BN is an ideal material to encapsulate graphene. The crystal structure is depicted in Fig. 3.6, taken from [118].

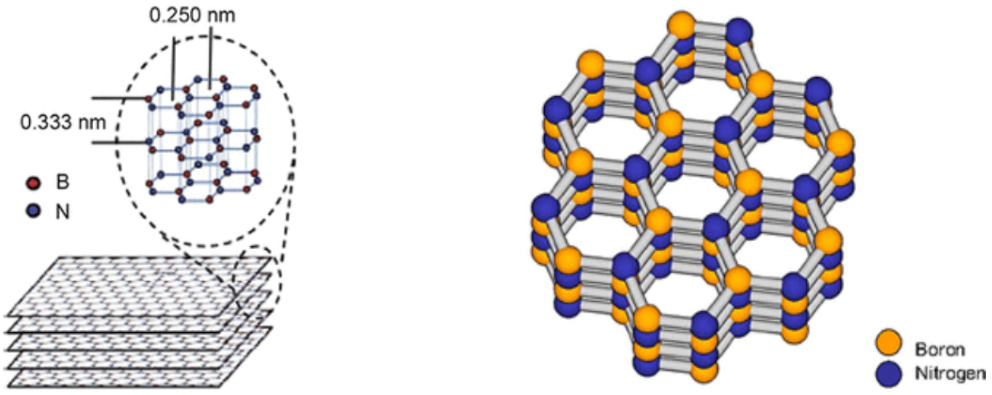

(a) (b)

Figure 3.6: a) Four sheets of h-BN are shown. The zoom-in shows three layers, together with the lattice constant and inter-planar spacing. b) Stacking of hBN sheets in the AAA configuration. Taken from [118]

In this work, graphene flakes were encapsulated in h-BN, before device fabrication took place. This is described in section 4.7.

3.3 Probing Localised States

3.3.1 Gating

Two-dimensional electron gases within GaAs/$Al_{1-x}Ga_xAs$ heterostructures can be depleted using a gate. The 2DEG and the gate metal act as two plates of a parallel plate capacitor. The carrier density of such a device decreases linearly

with negative gate voltage. One can reduce the density to such an extent that the Fermi level falls below a mobility edge, as depicted in Fig. 2.4. In this case, states at the Fermi level are localised and transport will take place via a strongly temperature dependant mechanism such as hopping or activation to the extended states above the mobility edge. See [14, 25–28] for examples of gated 2DEGs, hosted in various materials, being used to carry out localisation studies in the fashion described.

3.3.2 Disorder Broadened Landau Levels

High mobility GaAs/$Al_{1-x}Ga_xAs$ heterostructures exhibit the quantum Hall effect, as described in section 2.8.2. Using a standard Hall bar geometry, transport takes place via ballistic edge states which are topologically protected from backscattering events. However, one can design contacts which are not linked via edge states. For example, contacts placed in the middle of a sample. The most notable example is that of a Corbino ring. Such a device is circular, with one contact along the circumference with the second contact in the centre. Transport between contacts arranged in such a fashion avoids edge states and is instead via the localised states that occupy the bulk of the material and reside in the band tails of the disorder broadened Landau levels. When the filling factor, ν, is an integer, the Fermi level lies within such a band tail. See Fig. 2.14. By applying the necessary perpendicular magnetic field to achieve an integer filling factor, the Fermi level can therefore be manipulated to lie within localised states and localised transport can thus be studied using a suitable geometry.

3.3.3 Focused Ion Beam Damage

In this work, monolayer graphene was damaged by a helium focused ion beam (FIB). This method allowed for systematic addition of disorder. Both the dose

and area that was to be disordered could be carefully controlled. Using a Carl Zeiss Orion NanoFab FIB, 25 keV helium ions at a dose of 1 pCμm^{-2} were used. It was assumed that the disorder was added in the form of carbon vacancies. The FIB exposure was done after the graphene flake had been isolated from the environment and encapsulated in h-BN. In this way, any carbon vacancies which formed as a result of the damage would be prevented from bonding to any unwanted material, such as water. Ultimately, as discussed in chapter 8, exposure to the FIB was successful in creating an insulating flake in which the states at Fermi level were localised.

Chapter 4

Device Fabrication

In this chapter the various processing techniques that have been utilised are presented. They are then discussed with respect to both GaAs/$Al_xGa_{1-x}As$ and graphene devices. In general, each step typically involves a round of lithography followed by either an etch, a deposition or both.

4.1 Chip Cleaning

Before any given fabrication process following wafer growth, the chip being processed must be cleaned. This is to remove any unwanted material on the chip that may interfere with fabrication. This is particularly important following cleaving of the wafer as this typically leaves dust on the surface of the chip. Chips are sonicated in acetone for five minutes. This is then repeated with isopropyl alcohol (IPA). The acetone is to clean the chip, while the IPA is to prevent acetone streaks being left behind on the chip. Chips are then dried with a nitrogen gun.

4.2 Lithography

Once a given chip has been cleaned it is ready for a round of lithography. This is simply a means of transferring a pattern onto the chip. In this work, both

photolithography and electron-beam lithography (EBL) were used. Typically, EBL is used for smaller features due to the greater resolution of an electron beam compared to UV light. In either case, resist is first spun onto the chip and then baked. The resist is then exposed to either a UV laser beam or an electron beam, depending on the type of lithography. If the resist is a positive resist, all exposed areas will become soluble and hence removed once placed in the corresponding developer. The chip is then ready for either an etch, deposition or both.

4.2.1 Photolithography for Etching

Figure 4.1 demonstrates a typical round of photolithography for an etching process. First the chip is spin-coated with a positive photoresist, which becomes soluble once it has been exposed to UV light. In this work the photoresist used was S1805. Resist was spun at 4000 rpm for 30 seconds and baked at 115^{o}C for 1 minute. Spinning is done to produce a uniform layer of resist. Baking is done to remove residual solvent and harden the resist. These two steps produce a uniform resist thickness of 500 nm. Samples were then exposed using a direct laser writer, specifically a Heidelberg DWL 66+. The wavelength of the laser is 375 nm and the limit of resolution is around 1 μm. A digital mask was first created using computer-aided design (CAD) software. A mask used to create large van der Pauw (VDP) devices is shown in Fig. 4.2. In the case of this mask, everywhere but the shaded area will be exposed to the laser. Once the mask has been created and laser parameters set, the sample is aligned and the pattern is written onto the sample. This is depicted in Fig. 4.1a. Then the exposed, and now soluble, resist is removed using a developer. In this work, Microposit Developer MF-319 was used. After being immersed in developer for a given period of time, the chip is rinsed in deionised water and dried with a nitrogen gun. Chips were typically developed for 15 seconds before being checked under a microscope. So as not to

expose the resist whilst checking, a UV filter is used. Development is repeated until the resist is fully developed. One must be careful not to overdevelop, the unexposed resist will be slowly removed by the developer. Once development is complete, an etch can be carried out. After etching, the resist can be cleaned off with a suitable solvent, typically acetone.

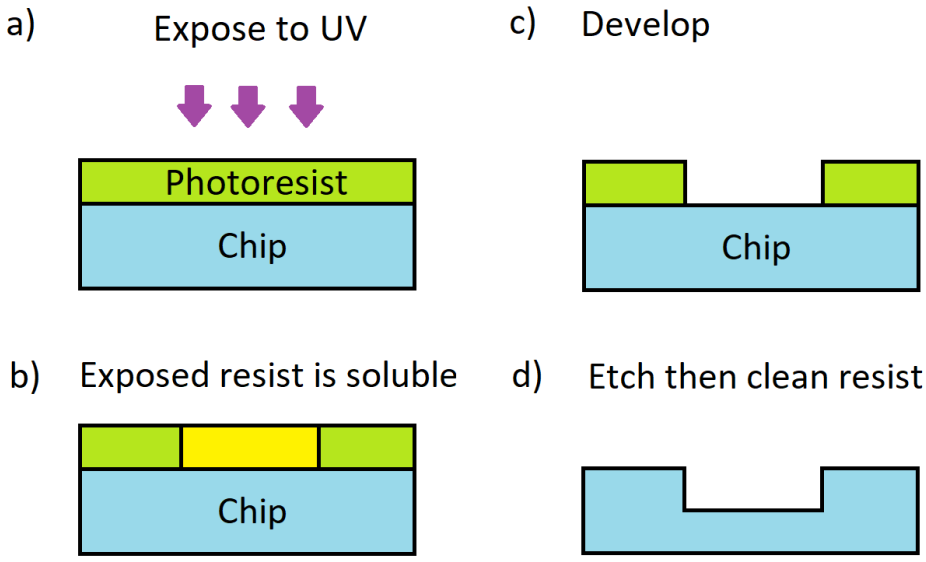

Figure 4.1: Steps when using photolithography to carry out etching. a) A spin coater is used to cover the chip in a uniform layer of photoresist. Parts of the chip are then exposed to a UV light source. b) The exposed resist becomes soluble and can be removed by c) developing. Finally, d) the etch is carried out and the resist cleaned off.

4.2.2 Photolithography for Metal Deposition

When carrying out photolithography for a deposition, using a bilayer resist is preferential, as demonstrated in Fig. 4.3. The procedure is much the same as with a single layer of resist. However, before spin-coating with photoresist, the sample is spin-coated with lift-off resist (LOR). Even without exposure to UV, LOR is soluble in Microposit Developer MF-319. This creates an undercut in the resist profile post development which, in turn, prevents the deposited metal from

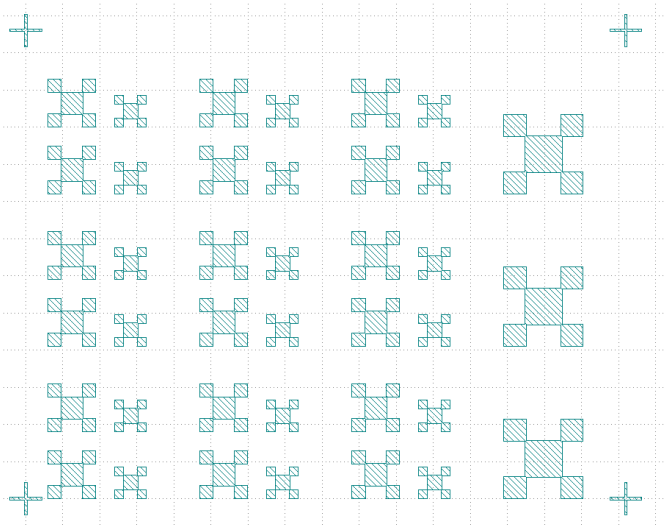

Figure 4.2: An example mask, used to create large van der Pauw devices. Everywhere but the shaded areas will be exposed. Thus, when developed, only these areas will have resist left. Note the alignment crosses in the corners of the design.

forming a continuous film over the sample, as depicted in Fig. 4.3b. This greatly increases the likelihood of a successful lift off.

In this work, LOR 10B was used as the lift off resist. Once the chip has been cleaned, LOR 10B is spun at 4000 rpm for 30 seconds. It is then baked at 190^{o}C for 10 minutes. The process from here on in is as described in section 4.2.1. S1805 is spun and baked, the chip is exposed to the laser writer and development in MF-319 is carried out. One has to be especially careful not to over-develop. If the undercut becomes too great, the top layer of photoresist can collapse.

Once development is complete, the sample is now ready for a deposition. Once this has been carried out, a suitable solvent must be used to clean off the resist and metal on top of it. This is known as lift off. Acetone cannot be used to carry out lift off if LOR has been used. It will cross-link the LOR which will thus become very difficult to remove. Another solvent, Dimethylsulfoxide (DMSO), was used in this work. Chips were heated in DMSO at 65^{o}C for ten minutes. A pipette was then used to create a gentle flow of solvent over the chip. Typically

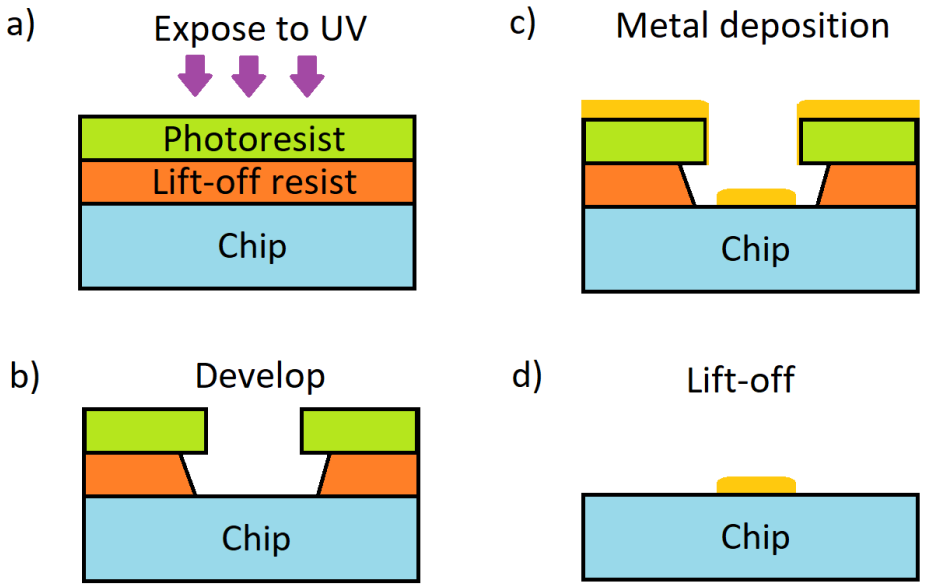

Figure 4.3: Steps when using photolithography to carry out a metal deposition. a) A spin coater is used to cover the chip in a uniform layer of lift-off resist (LOR) followed by photo-resist. Parts of the chip are then exposed to a UV light source. b) The exposed resist becomes soluble and can be removed by developing. The LOR is solvent in the developer, creating an undercut. c) Metal is then deposited. Note how the undercut prevents the metal from forming a continuous film over the sample. Finally, d) the resist is lifted off using a suitable solvent.

this resulted in the unwanted metal peeling back off the chip, leaving only metal in the desired areas.

4.2.3 Electron-Beam Lithography for Etching

The principles of electon-beam lithography (EBL) are the same as photolithography, only now the resist is exposed to an electon beam and not UV light. The resolution that can be achieved with EBL can be as low as a few nanometres, much less than the micrometre resolution of the direct laser writer. Thus this is the preferred lithographic method for devices that have features that need resolution of a few microns or less.

Polymethyl methacrylate (PMMA) is a common postive EBL resist and was used in this work. If etching, PMMA 950A2 was used. The name describes the

average chain length, solvent type and PMMA concentration. With this resist, the average polymer chain has a molecular weight of 950,000. The lower the molecular weight of the chains, the less exposure they need to become soluble. This particular resist has anisole as the solvent and the PMMA chains themselves make up 2% of the solution by mass. As with S1805 photoresist, the solvent is removed by baking. PMMA 950A2 was spun for 45 seconds at 2000 rpm. It was then baked at 180^{o}C for five minutes. This left a uniform resist profile of height 100nm.

As with the laser writer, CAD software was used to produce a mask. The EBL exposure was carried out using an Elionix ELS-G100 system. It has an inbuilt scanning electron microscope (SEM), allowing one to align the sample with the necessary accuracy. It is important to assume that any area of the chip looked at with the SEM will become fully exposed and thus lose resist post development. The beam energy, beam current were first set and the beam focused. A beam energy of 100 keV and beam current 1 nA were used. For GaAs/$Al_xGa_{1-x}As$ samples, the dose was typically around 600 μC/cm^2. However, proximity effect correction (PEC) software was used and the dose would vary throughout the sample area. This software takes into account the backscattering of electrons from the chip back into the PMMA. Gallium arsenide causes a large amount of backscattering. This must be considered when trying to achieve a uniform dose throughout the exposed area. The PEC software uses Monte-Carlo simulations to produce a map between position and local dose. For work involving a silicon substrate, which has significantly fewer issues regarding backscattering, a beam dose of 1000 μC/cm^2 was used.

Once the exposure had been carried out, development took place. In this work, a mixture of three parts isopropyl alcohol (IPA) to one part deionised water was used as the developer. Samples were developed for 30 seconds before being rinsed

in deionised water and checked optically. Further development was carried out if necessary. As PMMA is solvent in acetone, this was used to remove PMMA from samples once the etch was carried out.

4.2.4 Electron-Beam Lithography for Metal Deposition

Analagous to using LOR whilst carrying out photolithography, different PMMA resists can be combined to form a bilayer resist for electron-beam lithography. Specifically, resists of different average PMMA chain length should be used in combination. This technique makes use of the way the electrons travel through the resist during an EBL exposure. Rather than travelling straight through the resist, in a direction perpendicular to its surface, the beam spreads out from the point of incidence. This is due to scattering within the resist. The lower the molecular weight of a given PMMA resist, the more sensitive to a given dose it will be. Thus if a lower molecular weight PMMA is spun beneath a higher molecular weight PMMA, an undercut will be created due to the fanning out of the electron beam. This is depicted in Fig. 4.4. Here PMMA 495 is the lower molecular weight resist, while PMMA 950 is the heavier. Their chains have average molecular weights of 495,000 and 950,000 respectively.

In this work, PMMA 495A2 was spun onto the chip at 1000 rpm for 45 seconds. It was then baked at 180^{o}C for 3 minutes. This produced a 100nm uniform film of resist. This was repeated until the height of the PMMA 495 was greater than the thickness of the metal being deposited. Otherwise, the undercut would be rendered useless. Finally, PMMA 950A2 was spun onto the chip at 2000 rpm for 45 seconds and baked at 180^{o}C for 5 minutes, leaving a 100nm uniform film of PMMA 950. The chip was then exposed and developed as described in section 4.2.3. Lift off was carried out using acetone.

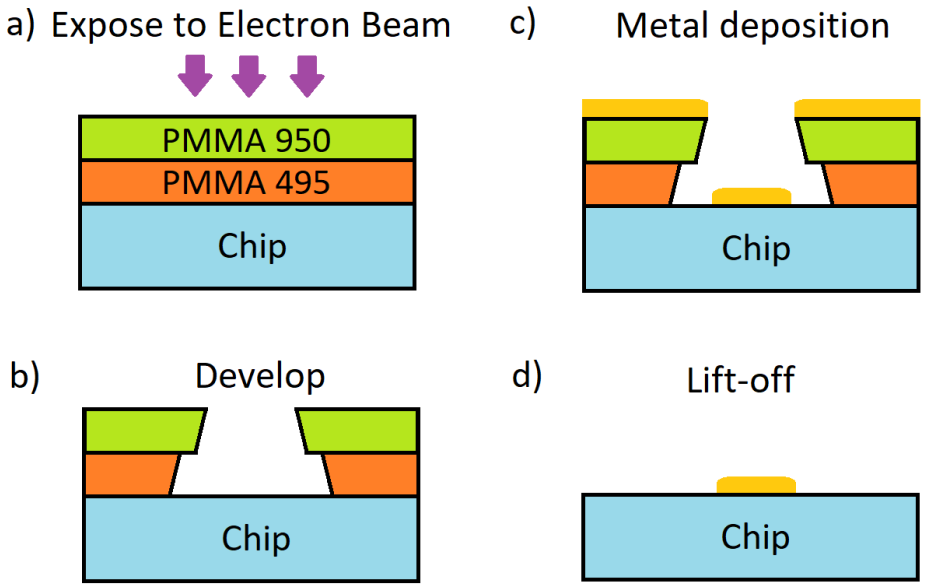

Figure 4.4: Steps when using electron beam lithography to carry out a metal deposition. a) A spin coater is used to cover the chip in a uniform layer of PMMA 495 followed by PMMA 950. The bottom layer of resist, due its shorter PMMA chains, takes less dose to become soluble. Parts of the chip are then exposed to the elctron beam. b) The exposed resist becomes soluble and can be removed by developing. More of the bottom layer is lost than the top, due to the difference in repsonse to the electron beam. This leads to an undercut. c) Metal is then deposited. Note how the undercut prevents the metal from forming a continuous film over the sample. Finally, d) the resist is lifted off using acetone.

4.3 Etching

Once the desired etch pattern has been transferred onto the chip, via lithography, the chip is ready to be etched. Both wet etching and dry etching were carried out throughout this work. The wet etches involved simply immersing the chip to be etched in an etchant, resulting in an isotropic etch. Conversely, dry etches typically tend to be much more anisotropic. As shall be discussed, this can be useful when attempting to etch small features.

4.3.1 Wet Etching

Wet etches should only be used to define relatively large features. Specifically, the etch depth should be less than the feature size. It should be assumed that a wet etch will etch laterally a similar distance to the vertical etch depth. This may not be the case if an etchant acts quicker along one crystal direction than the others. However this was not the case in this work.

As shall be discussed in section 4.6.1, wet etching was used to define the mesas of GaAs/$Al_xGa_{1-x}As$ devices. Here the etch depths were typically around 100 nm, meaning a wet etch would blur the features of the mesas by roughly this distance. This was acceptable in some situations, but not in all, as shall be discussed. Wet etching was also used to open windows through layes of dielectric, to access otherwise covered bonding pads. This shall be discussed in section 4.6.3.

4.3.2 Dry Etching

A shallow reactive ion etcher (SRIE), specifically a Surface Technology Systems ICP, was used to carry out dry etching. This was used to etch both GaAs/$Al_xGa_{1-x}As$ and graphene, see sections 4.6.1 and 4.7.3 respectively.

4.4 Metal Deposition

An Edwards Auto 306 thermal evaporator was used to deposit metal onto samples. Such metal was used either to form ohmic contacts or to gate devices. Using adhesive tape, samples were loaded onto a coppper plate which was hung face down from the top of the evaporator. Metal, travelling from the bottom of the evaporator, would uniformly coat the samples.

Metals were loaded into molybdenum boats. During evaporation current was passed through the boats, heating the metal to such a point that evaporation

took place. Molybdenum was chosen due to its high melting point, high thermal conductivity and lack of contaminant production.

After loading the samples and metals to be evaporated, the evaporator chamber was pumped down. A pressure below 1×10^{-6} mbar was considered sufficient. Such low pressures were necessary for two reasons. Firstly, at such pressures the mean free path of the evaporated metal is larger than the distance between source and samples. Hence ballistic transport and uniform coverage of chips should be achieved. Secondly, the low levels of background gases, such as oxygen and water, will significantly decrease any contamination of the evaporated metal film.

It is common to want to coat the sides of devices features. For example, when gating a device, it may be necessary for the gate metal to climb over the edge of the device mesa. If the metal does not climb over the edge, there may be no continuity between different parts of the gate metal and contact to the gate will be impossible. In order to get around this, the copper loading plate was rotated during evaporation and samples were placed off-centre. In this way, there will always be a point during evaporation where there is an unobstructed path between a given device feature and the metal being evaporated.

Once the chamber was sufficiently pumped down and the loading plate rotating, thermal evaporation could take place. Current was passed through the relevant source boat and increased until the metal to be evaporated melted. This was observed using protective eye-wear. Then a shutter covering the source boat was opened and evaporation took place. A quartz crystal monitor was used during evaporation. The crystal's resonant frequency varies as a function of mass deposited over its surface, allowing the desired deposition rate to be maintained as well as ensuring the correct amount of metal is deposited. A rate of 2-3 Å s^{-1} was typical. The copper loading plate, that the samples were mounted to, acted as a heat sink. This ensured that the chips did not reach too high a temperature. In

turn, this avoided resist defamation and damage to any undercuts, as introduced in sections 4.2.2 and 4.2.4.

Gold, germanium and nickel were deposited to form ohmic contacts for GaAs /$Al_xGa_{1-x}As$ heterostructures. See section 4.6.2 for further details. Gold, due to its corrosion resistance, was deposited to form gates throughout this work. However, gold typically has poor adhesion. A thin layer of either Titanium of Chromium was thus deposited first. See sections 4.6.3 and 4.7.5.

4.5 Packaging

Once the fabrication of a given chip was complete, the chip had to be cleaved. Typically it was cleaved into roughly 2 mm $\times$ 2 mm squares. These smaller chips would fit on the chip carriers which were themselves loaded into cryogenic measuring equipment. The device design shown in Fig. 4.2 should produce 12 chips of this size, arranged in a 4 $\times$ 3 array. Once secured to the chip carriers, the chips had to be bonded to the contact pads of the chip carriers.

4.5.1 Cleaving

First, S1805 photo-resist was spin coated onto the chips at 4000 rpm for 30 seconds. They were then baked at 115^{o}C for 1 minute. This was to protect devices from the wafer dust produced during scribing. Chip were scribed using a Karl Suss RA120 scriber. They were secured to its stage by vacuum and aligned. The stage was manually moved underneath the diamond tipped scribe and scribed from edge to edge. Cleaving was then carried out along these scribes. Chips were held on a glass slide, with a given scribe in line with the edge of the slide. Careful but firm pressure was placed on the side of the chip overhanging the slide, causing the chip to cleave along the scribe. Finally, the finished samples were immersed in acetone and then IPA for five minutes to clean off the resist. After being dried

with a nitrogen gun they were ready for packaging.

4.5.2 Bonding

GE varnish was used to secure chips to chip carriers. It was cured at 150^{o}C. It was important to only use a small amount of varnish, too much and the chip would not lie flat. Not only could this cause issues with bonding, but any magnetic field applied would not be in the wanted direction with respect to the chip. The varnish also served to thermally anchor the chip to the chip carrier.

A wedge bonder was used to bond gold wire between contact pads of devices and chip carriers. Device contact pads were typically designed to be around 100 μm $\times$ 100 μm, which was large enough to successfully bond to. Bonding was done at 150^{o}C using the inbuilt bonder stage heater. Extra care had to be taken when bonding to metal on top of a dielectric. Typically, in such instances, the adhesion between metal and sample was lower and caution was required in order to not to tear the metal from the chip. Test pads were used in order to select suitable bonder settings. The parameters to vary were the force at which the bonder presses into the sample and the power of the ultrasonic mechanism which forms the bonds. Typically, a lower force setting than usual was optimal when bonding on top of a dielectric. Once bonded, devices were ready to be measured.

4.6 GaAs/$Al_xGa_{1-x}As$

4.6.1 Mesa Definition

With GaAs/$Al_xGa_{1-x}As$ devices, the first step is typically to define a mesa. That is, the 2DEG is restricted to only exist in certain areas. This is done by either wet or dry etching of the wafer. A typical etch mask to define such a mesa is shown in Fig. 4.2. Note the crosses in the corners of the design. These are needed

to assist in aligning other designs when carrying out further processes, typically depositions, after etching.

All of the wafers in this work have the GaAs/$Al_xGa_{1-x}As$ interface 90 nm from the surface. This meant that when defining a mesa, etch depths were typically 100 nm. As discussed in section 4.3, wet etches are typically isotropic so not only is 100 nm etched vertically, around 100 nm is etched laterally. For devices that are much larger than this lengthscale, this is not an issue. As dry etches tend to be much more anisotropic, they are favourable for devices of a similar lengthscale.

Wet Etching

Before wet etching, once lithography had taken place, the resist profile was measured using a profilometer, specifically a Bruker DektakXT. Under the preparation conditions described in section 4.2.1, S1805 resist typically had a profile around 500 nm. By measuring again after a period of etching, it could then be determined how far had been etched without removing the resist.

GaAs/$Al_xGa_{1-x}As$ chips were wet etched using a mixture of sulphuric acid, hyrdogen peroxide and deionised water in a ratio of 1:8:120, by volume [119]. The etch rate was $\sim$3 nm/s. The chips were then rinsed in deionised water and dried with a nitrogen gun. After measuring the etch depth, once could etch more if needed. Resist was then cleaned off by immersing in acetone and then IPA, each for five minutes.

Dry Etching

Selective reactive ion etching (SRIE) was used to carry out dry etching. With this technique, a plasma is generated using a large radio-frequency electromagnetic field. It is the ions within the plasma that react with the sample surface and carry out the etching. Because the plasma is directed towards the sample by means of a DC bias, the etch is directional and lateral etching is greatly reduced

when compared to wet etching. In this work, when etching GaAs/$Al_xGa_{1-x}As$, the plasma was generated using chlorine and nitrogen gas.

Dry etching was carried out when faced with the task of defining small features, relative to the etch depth. This also meant that electron-beam lithography (EBL) was used, as opposed to photolithography, meaning that the resist being used was PMMA. The PMMA itself was also attacked by the chlorine plasma etch. This meant it had to be ensured that samples were coated in sufficient resist. Once etching was complete, resist was again cleaned off by immersing in acetone and then IPA.

4.6.2 Ohmic Contacts

Once a mesa had been defined, it was typical to then fabricate ohmic contacts. Such contacts allow the 2DEG to be electrically probed. Ideally their resistance should be as low as possible and, as their name suggests, they should be ohmic.

Again, the necessary lithography was then carried out. Before carrying out evaporation of the necessary ohmic metal, two further processes were carried out. Firstly, samples underwent a two minute oxygen plasma ash to remove any resist not fully removed when developing. A Diener plasma asher was used. Secondly, samples were then immersed in 10% hydrochloric acid for ten seconds and then rinsed in deionised water. This was to remove any oxides on the surface of the chip that would interfere with the production of the contacts.

In this work, when forming contacts to GaAs/$Al_xGa_{1-x}As$ heterostructures, a 400 mg slug of gold, germamium and nickel, in a ratio of 83:5:12 by weight, was thermally evaporated. This produced a 150nm film of metal. Once lift-off was complete, the samples were annealed. This is done so that the ohmic contact material will diffuse down through the chip, at least as far as the GaAs/AlGaAs interface where the 2DEG will form at low temperatures. An 80 s anneal at

430^{o}C produced acceptable ohmic contacts for samples with 2DEGs 90 nm below the wafer surface. A Solaris rapid thermal processor was used to carry out anneals. Because annealing was done at a relatively high temperature, ohmic contacts were fabricated before samples were gated or coated in dielectric.

4.6.3 Gating

If required, metal was thermally evaporated onto chips in order to fabricate gates. The gate metal can be thought of as one plate of parallel plate capacitor, while the 2DEG acts as the second. Hence varying the potential difference between the two, varies the carrier density of the 2DEG.

As with ohmic metal deposition, samples first underwent a plasma ash. A hydrochloric acid dip was not required if the metal was to lie directly on top of the wafer. Any oxides present would actually improve adhesion. However, if depositing onto a dielectric such as silicon dioxide or aluminium oxide, such a dip was carried out to roughen the oxide surface and improve adhesion.

In this work, samples were gated with gold due to its resistance to corrosion and high electrical conductance. However, gold typically has poor adhesion. To resolve this, a 20 nm layer of titanium was deposited first. Titanium has good adhesion to gallium arsenide. Following this, 120 nm of gold was deposited. For mesa depths of 100 nm, a 140 nm film of metal is enough to ensure gate continuity across devices even if the metal has to climb the mesa.

In some instances, multiple overlapping gates were necessary. In such a situation an insulator must be deposited between gate metal evaporations. In this work aluminium oxide was deposited via atomic layer deposition (ALD). This process typically leads to a conformal coating, which helps to minimise the chance of leakage between gates. A deposition of 30 nm was typically carried out. Such a process will cover contact pads that have been fabricated prior to this fabrication

step. In order to access them, the dielectric above them must be etched away. This was done via photolithography and wet etching, using a buffered oxide etch (BOE). The solution used was a mixture of ammonium flouride and hydroflouric acid (HF) in a volume ratio of 7:1. HF will dissolve glass-wear so specialist beakers made of polytetrafluoroethylene (PTFE) had to used. The etch rate of aluminium oxide was 1 nm/s. Just like the wet etching of the mesa, etch progress could be monitored using a profilometer.

4.7 Graphene

Although the fabrication of graphene and GaAs/$Al_xGa_{1-x}As$ devices did involve similar techniques, such as etching and metal deposition, the overall processing did differ considerably. This is primarily due to the fact that when processing with GaAs/$Al_xGa_{1-x}As$, the chip is essentially a large, blank canvas. Many devices can be created simultaneously, by fabricating over the whole of a given chip. However, with graphene, a graphene stack has to first be produced, which itself occupies a fraction of the area of the chip it resides on. Given the differences between different stacks, it is common to have to design a bespoke mask set for a given stack. Typically these stacks are on the micron scale meaning electron-beam lithography has to be used at every stage of fabrication.

4.7.1 Stacking

The first stage of fabricating graphene devices involved sandwiching graphene flakes between hexagonal boron nitride (h-BN), which is atomically flat, has a hexagonal honeycomb lattice and has a similar lattice constant to that of graphene. It is also a large band gap (5.9 eV) semiconductor and thus acts as an insulator. These properties make it an appropriate material to encapsulate graphene.

The graphene flakes themselves were prepared via mechanical exfoliation, us-

ing adhesive tape. First, the tape was firmly pressed against a graphite crystal. Another piece of tape was then placed over the first. The two were then peeled apart and stuck back together. This was repeated multiple times. The tape was then pressed firmly against a silicon wafer which had 290 nm of silicon dioxide grown on it. To allow the graphene to relax and adhere well to the substrate, the tape was left in place for an hour. Following this resting period, the tape was peeled off and the wafer was ready to be examined under an optical microscope for suitable graphene flakes. The graphene preferentially stuck to the silicon dioxide over the tape due to the stronger van der Waals interactions with silicon dioxide.

The same process was undertaken with man-made h-BN crystals. Suitable flakes of h-BN and graphene were then identified. Due to interference effects, the colour of the h-BN flakes on 290 nm silicon dioxide was indicative of their thickness. Likewise, the optical contrast of a given graphene flake was was used to determine its thickness. Once suitable flakes were located, they were picked up and stacked using polymethyl methacrylate (PMMA). The PMMA itself was on top of a layer of polydimethylsiloxane (PDMS). Using a glass slide in a micro-manipulator, the PMMA was used to pick up a wanted h-BN flake. This flake could then be used to pick up a graphene flake. Both flakes could then be placed down on top of another h-BN flake. The h-BN flakes were always larger than the graphene flakes, so as to completely encapsulate them. In this way, graphene/h-BN heterostructures could be produced.

4.7.2 Device Design

Once a stack was complete, device design could take place. The first step was to transfer alignment marks onto the chip, surrounding the stack. After doing this, designs based on optical images containing the alignment marks could be produced. Electron-beam lithography was used to pattern crosses into PMMA.

The profile of the PMMA had to be suitable for the first round of processing to be carried out, as the same PMMA would be used for this process. Typically the first process was a metal deposition, so a bilayer resist was used. Figure 4.5a shows a stack coated in PMMA and surrounded by alignment crosses.

(a) (b)

Figure 4.5: Typical images used when designing a device mask set. a) Example of a graphene/hexagonal boron nitride stack coated in PMMA and surrounded by alignment marks produced by electron-beam lithography. b) The subsequent mask set superimposed onto an image of the stack, surrounded by the alignment marks used to create a coordinate system when carrying out each stage of lithography.

Computer aided design (CAD) software was used to design mask sets, specifically Inkscape and KLayout. Figure 4.5b shows such a mask set superimposed onto an image of a stack, with alignment marks surrounding it. These alignment marks would then be used to define a coordinate system when carrying out each lithography step to ensure patterns were written accurately.

4.7.3 Etching

All etching of graphene devices was carried out using selective reactive ion etching (SRIE). The technique is described in section 4.6.1. To etch boron nitride, a sulphur hexaflouride plasma was used and to etch graphene an oxygen plasma was used. Etching was carried out to both define device shapes and also to expose the graphene in order to make electrical contact with it. When doing the latter, the nature of the electrical contact had to be considered. By being exposed to

the boron nitride etch, the exposed graphene would be damaged. Hence it was not desirable to make contact with this area of graphene, but rather the graphene untouched by the etch. For this reason, the graphene directly under the etched boron nitride was also etched away. In this way, lateral contact could be made to the unexposed graphene. The contact would essentially be one dimensional. As will be discussed in section 4.7.4, it had to ensured that the deposited contact metal coated the side wall of the etched space, in order to make this one dimensional lateral contact.

The reactive ion etch also attacked the PMMA resist. Not only was it important to have enough resist before the etch, it was important to be thorough when removing the resist. Post etch, acetone by itself would no longer completely clean samples. The Diener plasma asher, also used before depositing metal when using photo-resist, was used until all resist residue was removed.

4.7.4 Contacts

Once the relevant layers had been etched away, contact metal was deposited by thermal evaporation into the etched space. Contacts were formed by depositing 40 nm of gold, again chosen due to its high electrical conductivity and corrosion resistance. However, 1 nm of chromium was deposited first due to its greater adhesion to silicon dioxide. As discussed in section 4.7.3, contacts were made laterally and the deposited metal thus had to coat the side walls of the etched space. To do this, samples were rotated during evaporation and placed off centre on the loading plate. In this way, there would always be an unobstructed path between a given side wall and source metal at some point during evaporation. This same technique was used to coat side walls of GaAs/$Al_xGa_{1-x}As$ mesas, as discussed in section 4.4.

4.7.5 Gating

Top Gates

Like with GaAs/$Al_xGa_{1-x}As$ heterostructures, gold metal deposited by thermal evaporation was used to fabricate top gates. The process was the same as when depositing contact metal. Due to its stonger adhesion to silicon dioxide a 1 nm layer of chromium was deposited first. This was followed by 40nm of gold.

The resistance of gold to both the sulphur hexaflouride and oxygen plasma etches, meant that a top gate could be used as part of an etch mask. In this way, the top gate would necessarily completely cover the device being fabricated.

Back Gates

The silicon wafer that devices were fabricated on were heavily doped and thus metallic. The silicon dioxide and boron nitride acted as dielectric. The wafer itself acted as a back gate. Silver paint was used in place of GE varnish when packaging chips. In this way, bonds could be made directly to the metallic chip carrier to establish an electrical connection to the silicon back gate.

Chapter 5

Cryogenic Measurements

In this chapter the cryogenic equipment used to cool samples are introduced. Various cryostats were used, each having a different associated temperature range. Following this, the various pieces of electrical measuring equipment and the different configurations they were used in are discussed.

5.1 Cryogenics

Throughout this work, temperature dependent transport measurements have been at the centre of characterising the physical properties of a given system. The ability to accurately set and measure different temperatures has thus been essential. Further to this, when probing behaviour in the localised regime, it is typically required that the temperature, T, is less than the characteristic temperature associated with the dominant transport mechanism. For example, if measuring activation to a mobility edge, it is preferable that $T < T_0$, where $k_B T_0$ is the difference between Fermi energy and mobility edge. This has often meant that ultra low temperatures have been necessary, meaning temperatures below 1 K.

Three different systems were used to achieve cryogenic temperatures. The first made use of a ^{4}He cryostat and could achieve temperatures as low as 1.5

K. The second made use of the same cryostat to cool to 1.5 K, but could then be subsequently cooled to as low as 300 mK by pumping on ^{3}He. The final, and arguably most useful system, was a ^{3}He/^{4}He dilution refrigerator which had a base temperature of 20 mK. Each system is now discussed in turn.

5.1.1 ^{4}He Cryostat

The ^{4}He cryostat used in this work is a dry system and can achieve stable temperatures between room temperature and 1.5K. The system is a dry system meaning that all cryogens are contained and do not need to be regularly replenished.

Cooling is broken down into multiple stages. The first two stages use ^{4}He pulse tubes to first cool to 30 K and then to 4 K. The 4 K stage in turn cools a separate ^{4}He circuit. Joule-Thomson expansion is then used to cool the helium in this circuit to 1.5 K. The helium is pumped through an orifice, after which it expands and cools. A needle valve is used to manually control the size of this orifice. Via heat exchangers, this low pressure helium is in thermal contact with the outer wall of the sample space. This in turn is in thermal contact with any sample in the sample space via exchange gas, also ^{4}He.

The probe contains a heater and thermometer. These are used together, as well as a PID (Proportional Integral Derivative) controller, to set sample temperatures. It is then assumed that the measured temperature is the same as the sample lattice temperature. The electron temperature, due to electrical over-heating effects, may well be different. Temperatures between 1.5 K and room temperature can be set.

5.1.2 ^{3}He Insert

Using the same cryostat as discussed in section 5.1.1, temperatures as low as 300 mK could be achieved. This was done using a specialist probe, which utilised the cooling power due to pumping on ^{3}He. When a liquid is pumped on, while it is

in equilibrium with its own vapour, the liquid is cooled. The cooling power is a result of the movement of molecules across the phase boundary from liquid to gas, which is an endothermic process.

The ^{3}He insert operation is similar to that of the standard probe described in section 5.1.1. However, the sample is instead loaded into a sealed can which is then pumped down using a turbo pump to a pressure of around 1 x 10^{-6} mbar. A small amount of ^{4}He exchange gas is then admitted to the can. The probe is then loaded into the cryostat as normal and cooled to 1.5 K. Within the can is a roll of activated charcoal which absorbs the ^{4}He exchange gas inside the can, below 8 K. This thermally decouples the sample from the sample space of the main cryostat. The ^{3}He system is a closed system and is weakly thermally coupled to the main cryostat. Over a period of roughly an hour, the ^{3}He is condensed and cooled to 1.5 K. The liquid ^{3}He is thermally coupled to the sample. Once condensation of the ^{3}He is complete, the ^{3}He is pumped on using a sorption pump. The effectiveness of this pump is temperature dependant. The hotter the pump, the less absorbent it is and the less effective it will be. Below 10 K its behaviour is roughly invariant and the liquid ^{3}He will be cooled to 300 mK. At 30 K it effectively stops pumping and the system will reach equilibrium at 1.5 K. Next to the pump is a heater, meaning that the temperature of the sorb can be varied in order to vary the temperature of the liquid ^{3}He and thus the sample.

5.1.3 ^{3}He/^{4}He Dilution Refrigerator

The final system to discuss is the dilution refrigerator. This system uses a mixture of ^{3}He and ^{4}He to cool to temperatures as low as 20 mK. Such a mixture naturally separates into two phases, one which is almost 100% ^{3}He and one which is around 6% ^{3}He. They are known as the concentrated and dilute phases respectively. Analogous to molecules moving across a phase boundary from liquid to gas, ^{3}He

moving from the concentrated to dilute phase is an endothermic process and removes heat from the environment. The crucial difference here is that if a liquid is pumped on to cool it, like is done in pure ^{3}He or ^{4}He systems, eventually the vapour pressure would become too low and it wouldn't be possible to continue pumping. Whereas with a dilution refrigerator, the dilute phase crucially stays at around 6% ^{3}He even as temperature tends to absolute zero. The phase boundary crossing takes place in what is known as the mixing chamber and is the coldest part of the fridge. Samples are placed in thermal contact with the mixing chamber. To drive the ^{3}He across the phase boundary, the dilute phase is pumped on. This takes place in what is known as the still. As ^{3}He has a higher vapour pressure than ^{4}He, effectively only ^{3}He is pumped around the circuit. The mixing chamber and still are shown in the schematic of Fig. 5.1.

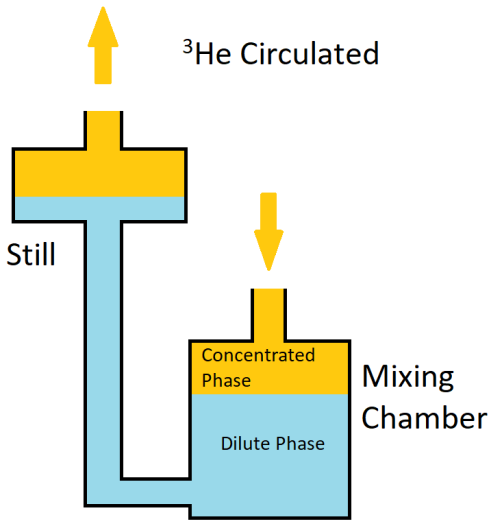

Figure 5.1: Mixing chamber and still of a dilution refrigerator. In the mixing chamber ^{3}He moves across the phase boundary, which provides the cooling power of the fridge, and is pumped around the circuit.

The sample is placed in a puck which is then loaded into the fridge via a load lock. Again, wiring running up through the fridge connects the sample with coax-

ial cable connections at the top of the fridge. The dilution refrigerator contains a 12 T superconducting magnet. By the sample is a heater and thermometer. Just like the other systems, this allowed for temperatures to be measured and set. Samples could only be heated to 1.2 K. Above this there was a risk that the helium would be boiled off and cooling power would be lost. Thus temperatures between 20 mK and 1.2 K could be set.

None of the systems could access the whole temperature range of 300 K down to 20 mK. This meant that samples had to be measured in different systems over different cooldowns.

5.2 Electrical Measurements

All of the measurements made throughout this work were made in order to ascertain a particular resistance or a current-voltage characteristic. In either case, a voltage is applied in some way and the resultant current measured. If a four terminal measurement is appropriate, a voltage is measured too. As is typical within the field of quantum transport, resistances are used to infer physical properties of the system in question. In this section the various techniques to do just this and the motivations behind each technique shall be discussed. All equipment was controlled using scripts utilising the PyVISA python module [120].

5.2.1 Alternating Current Measurement

A lock-in amplifier can be used to output a voltage at a given frequency. When a signal is input back into the lock-in amplifier, it essentially performs a Fourier transform. It does this in order to find the component of the input signal that has the same frequency as the output. It is ultimately a noise reduction technique. A reference frequency can also be input into other lock-in amplifiers, which can then find the component of the same frequency from different inputs. A common set-

up involves using two lock-in amplifiers, one measuring a current and the other a voltage. The output is ideally a small excitation voltage, so as to probe the linear response of a given sample. Typical two terminal and four terminal set-ups can be seen in sections 5.2.3 and 5.2.4 respectively.

Issues can arise when making alternating current (AC) measurements of high resistance samples. The effect of any capacitance or inductance within the measurement circuit, known as parasitic impedance, must be considered. For example, the capacitance of a coaxial cable. At a non-zero frequency the reactance, imaginary part of the impedance, becomes finite. Consider the case of this reactance magnitude becoming comparable to the resistance of the device being measured. The path to ground that the AC current can take via the capacitance of the coaxial cable, instead of going through the device, now cannot be ignored. Instead of measuring just the device, the response of the capacitance which is in parallel with the device is also being measured. It is required that $r << 1/\omega C$ where C is this capacitance, ω is the applied angular frequency and r is the sample resistance. If this is not the case, either the frequency must be reduced or another way of measuring resistance must be found. See Fig. 5.2 for a simple circuit depicting the issue.

Both Zurich MFLI and Signal Recovery 7265 lock-ins were used. The Zurich MFLI had both voltage and current inputs, whereas the Signal Recovery lock-ins were used in conjunction with a current pre-amplifier. The pre-amplifiers converted the current input to a voltage output, which was in turn fed into the appropriate lock-in. Typically a frequency of 33.33 Hz was used when measuring low resistance samples. When dealing with highly resistive samples, a frequency of 4 Hz was found to be the optimal frequency when considering both the effects of noise and parasitic capacitance.

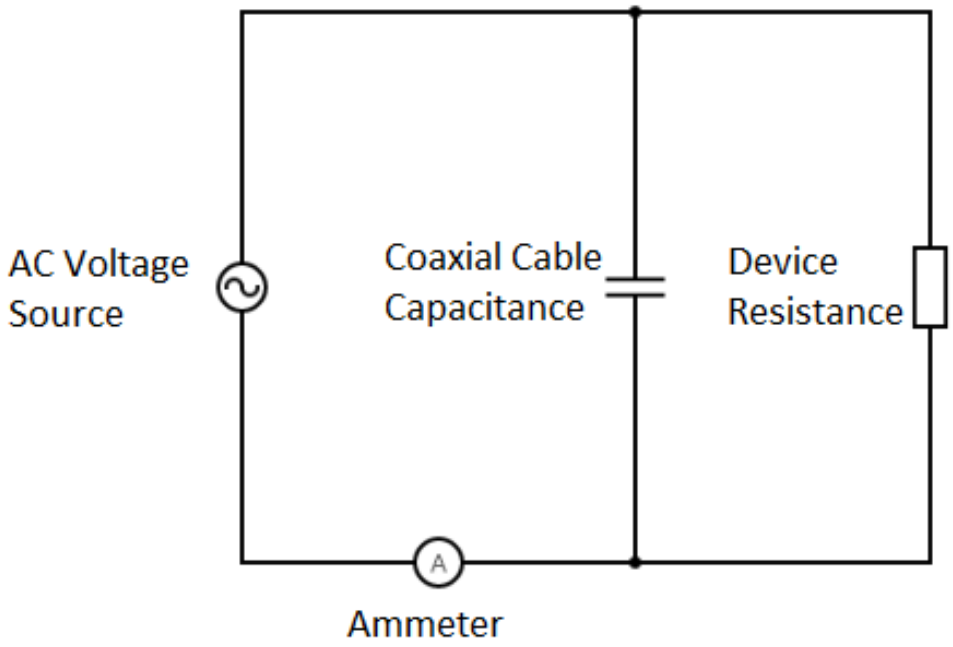

Figure 5.2: Circuit demonstrating the problem of parasitic capacitance when measuring high resistance samples. If the impedance magnitude of the path to ground via the coaxial cable capacitance is no longer much greater than that of the path through the device, one will begin to measure current due to this unwanted path. This is thus an issue when making AC measurements of highly resistive devices.

5.2.2 Direct Current Measurement

To get around the issue of finite reactance within the measurement circuit, direct current (DC) measurements can be made. The main issue with this technique is the increased noise associated with such measurements, when compared to using a lock-in amplifier. For example, any equipment reliant on mains power will introduce noise at 50 Hz. Other electromagnetic sources of noise include radio waves and wifi signals. Physical vibrations, most notably due to pulse tube operation, also introduce noise.

When making a DC measurement it is instructive to measure a current-voltage characteristic, otherwise known as an IV curve. Unlike an AC measurement in which a small excitation voltage is applied to probe the ohmic, meaning linear, re-

sistance, the non-ohmic regime of the material can be probed. Such measurements are critical when investigating samples with significant electron overheating. In such instances, the non-ohmic regime is of great importance. Furthermore, measuring a current-voltage characteristic allows any potential DC offsets within the circuit to be found. The ohmic resistance can be found by taking the linear part of the characteristic, around zero applied bias.

DC measurements were made by applying a bias voltage over a range of values and measuring the resultant currents. The voltages were applied using a Zurich MFLI and currents measured using a Keithley 6514 electrometer which had a noise floor around 1×10^{-13} A. All DC measurements were two terminal owing to the small relative series resistances involved when choosing to make such a measurement, as discussed in section 5.2.3.

5.2.3 Two Terminal Measurement

This measurement involves a voltage being applied between two contacts of a device and measuring the resultant current. The main drawback of such a measurement is that some of the applied voltage is dropped across both the wiring of the circuit and, usually more significantly, the device contacts. Hence the resistance given by simply dividing the applied voltage by the measured current includes this series resistance. A typical set-up, using a lockin to both apply an excitation voltage and measure the resultant current, is depicted in Fig. 5.3.

Such measurements were thus taken when the device resistance was much larger than the parasitic series resistance. In some cases, it was the only option. When measuring transport through localised states in the quantum Hall regime, the relevant resistance was between contacts in the middle of the sample. No other configuration, other than a two terminal measurement, could be used.

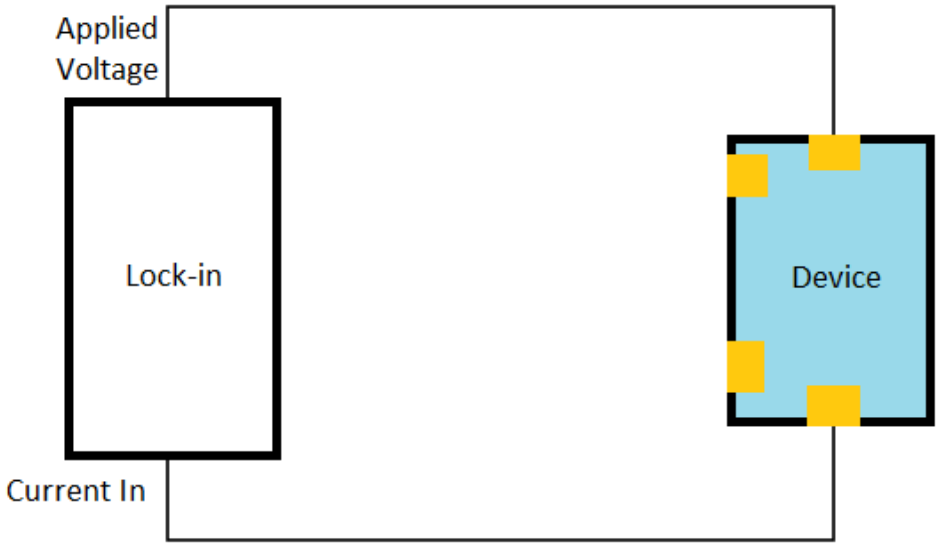

Figure 5.3: A typical two terminal set-up using a lock-in amplifier to both apply an excitation voltage and measure the resultant current.

5.2.4 Four Terminal Measurement

Such a measurement overcomes the issue of a parasitic series resistance. Again a voltage is applied between two contacts and the current measured. However, this time the voltage is also measured between two additional contacts, hence the name. The resistance between these two contacts can be determined by dividing the measured voltage by the measured current. There is no need to worry about series resistance as a voltage measurement should, ideally, draw no current. Thus the potential difference measured will be the same potential difference that is found along the current path between the two contacts. A typical set-up in which one lock-in applies an excitation voltage and measures the resultant current, while another measures the voltage along the device, is depicted in Fig. 5.4. So that the second lock-in has knowledge of the frequency and phase of the first, a reference

signal is passed from the first to second.

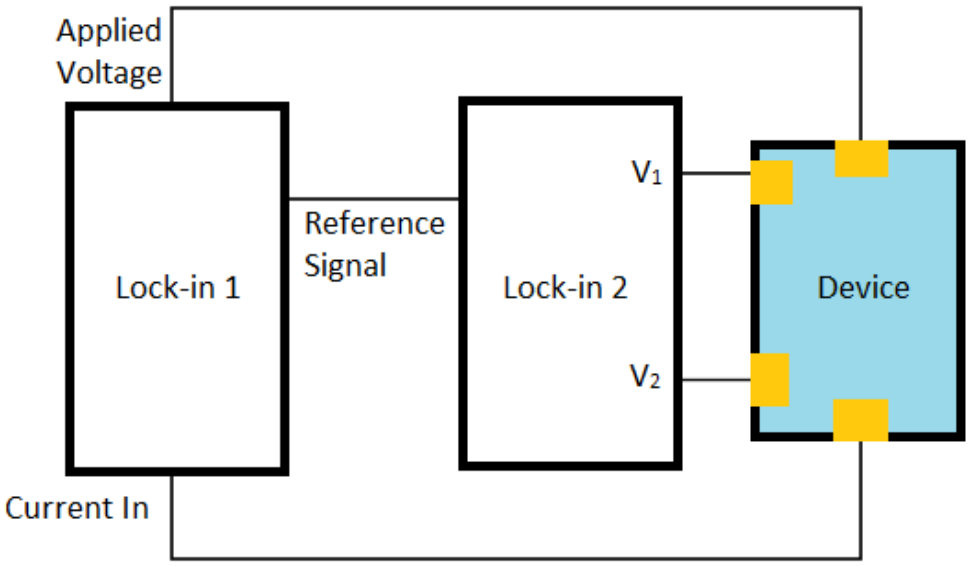

Figure 5.4: A typical four terminal set-up in which one lock-in amplifier applies an excitation voltage and measures the resultant current. The second lock-in amplifier measures the voltage along the device, V_1-V_2. So that the second lock-in has knowledge of the frequency and phase of the first, a reference signal is passed from the first to second.

Often, for low resistance devices, it is not essential to measure the current. An essentially constant current can be applied by placing a large resistor in series with the device. Assuming this resistance is much larger than the device's, the current will be very close to the applied voltage divided by this resistance.

Chapter 6

Hall Effect in Localised GaAs

In this chapter, results regarding the Hall effect in two different localised transport regimes are presented. Specifically, the Hall effect is measured when transport takes either an Arrhenius form or is via Efros Shklovskii hopping. Thus conductivity takes the form,

$$\sigma(T) = \sigma_0 \exp\left[-\left(\frac{T_0}{T}\right)^{\gamma}\right], \tag{6.1}$$

where $\gamma = 1$ and $\gamma = 1/2$ for Arrhenius transport and Efros Shklovskii hopping, respectively. The motivation for this work stems directly from the discussions of the Hall effect in chapter 2. In section 2.6.1 it was asserted that convincing experimental evidence of activation to a mobility edge does not exist in the literature; an observation of Arrhenius Hall carrier density with the Fermi level below a mobility edge has never been reported. Assuming the finite lifetime of states above the mobility edge has no bearing on the Hall effect, one would expect to observe an Arrhenius Hall carrier density if transport is via activation to a mobility edge. In this work, using a 300 μm square van der Pauw device, such behaviour is reported for the first time. Furthermore, and just as significantly, the mobility is shown

to be independent of Fermi level in this regime. As shall be discussed, the Fermi level is manipulated using a gate. This is arguably one of the most important results presented in this thesis and is strong evidence of transport via activation to a mobility edge. A temperature dependent Hall effect will also be presented in the Efros Shklovskii transport regime. The temperature dependences will be compared to current theories, previously discussed in section 2.8.1. However, as shall be seen, the physical picture of the Hall effect in the hopping transport regime is not clear, unlike that of the activated carrier density work.

In addition, the successful development of a gate defined 5 μm square van der Pauw device is demonstrated. By carrying out a focusing type measurement, the two gate system used to define the square is shown to work as intended. A third gate was used to deplete the square and thus carry out localised transport measurements. The motivation behind measuring these smaller devices, relative to the 300 μm devices, was to investigate whether transport properties associated with an activated conductivity vary with sample size. If the Hall effect is dependent on lifetime at the mobility edge, a sample size equal to or less than the associated lengthscale should display different properties compared to a sample size larger than this lengthscale. Given the difficulty in calculating the lifetime at the mobility edge, it is unclear if 5 μm will be less than this lengthscale. However, it is still worthwhile exploring a possible lengthscale dependence of the Hall effect. The 300 μm and 5 μm devices allow for exactly this. Note also that if the phase coherence length exceeds the sample size, universal conductance fluctuations will be observed. See section 2.3 for a full discussion regarding the impact of sample size, mean free path and phase coherence length on quantum coherence effects. The 5 μm devices, close to depletion, suffered with issues related to contacting the central square. This meant that it was not possible to probe as deep into the band tail as was possible with the 300 μm devices. However, a temperature

dependent carrier density was still observed.

6.1 Device Fabrication and Basic Characterisation

The material used in this work was an $Al_{0.33}Ga_{0.67}As$/GaAs heterostructure. The 2DEG resides at the $Al_{0.33}Ga_{0.67}As$/GaAs interface, 90nm below the wafer surface. A schematic of the wafer is shown in Fig. 3.3a. The density of the silicon dopants in the 40 nm doped layer is 1.2×10^{18} cm^{-3}. Square devices were made in order to perform van der Pauw measurements [121]. Such a geometry was chosen due to the reduction of longitudinal signal mixing when making Hall measurements, compared to a standard Hall bar geometry. Gated devices with square side length of 300 μm and 5 μm were fabricated. As shall be discussed, the fabrication of the 5 μm devices was more involved than the 300 μm devices. In both cases, a global top gate allowed application of a gate voltage, V_g, and thus manipulation of the Fermi level below the mobility edge. Mesas, ohmic contacts and gates were fabricated as described in section 4.6.

6.1.1 300 μm Samples

The square of the 300 μm samples was simply defined by a wet-etched mesa. An image of such a device can be seen in Fig. 6.1. This device is suitable for four terminal van der Pauw (VDP) measurements. A gate covers the square in order to deplete the 2DEG and bring the transport into a localised regime.

To carry out basic device characterisation, longitudinal and Hall resistances were measured as a function of magnetic field at $V_g = 0$. This was done at 1.5 K in a four-terminal set up, as depicted in Fig. 5.4, with a 50 μV excitation at 33.33 Hz. Longitudinal resistance against magnetic field is shown in Fig. 6.2a.

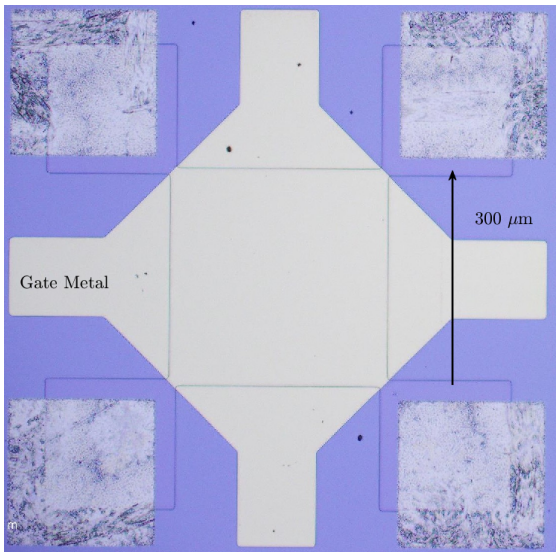

Figure 6.1: 300 μm square device. The gate covers the square. The ohmic contacts are seen in the corners of the device.

The Shubnikov-de Haas oscillations are well behaved, meaning that the minima fall to zero, indicating the absence of parallel conduction. The Fourier transform of this longitudinal resistance is shown in Fig. 6.2b. As the filling factor is given by $\nu = hn/eB$, the period of the Shubnikov-de Haas oscillations, when plotted agsint the reciprocal of magnetic field, should be equal to e/nh if Landau levels are sufficiently spin split. The dominant frequency of the oscillations will therefore be nh/e. However, to produce a meaningful Fourier transform, many periods of oscillation are needed. Using data which only covers the lowest filling factors will not suffice. Therefore, data at low magnetic fields is typically used, in which case the Landau levels are effectively not spin split. In the case of Fig. 6.2b, data used was between 0.001 T - 0.7 T. The dominant frequency will therefore be $nh/2e$. Thus by multiplying the frequencies of the Fourier transform by $2e/h$, the dependent variable of the Fourier transform plot can be carrier density and one can easily determine the carrier density of the device. Note that before Fourier transforming, the derivative of the resistance with respect to $1/B$ was taken so as to remove the zero frequency component. The carrier density was thus found to

be 1.45×10^{11} cm^{-2}.

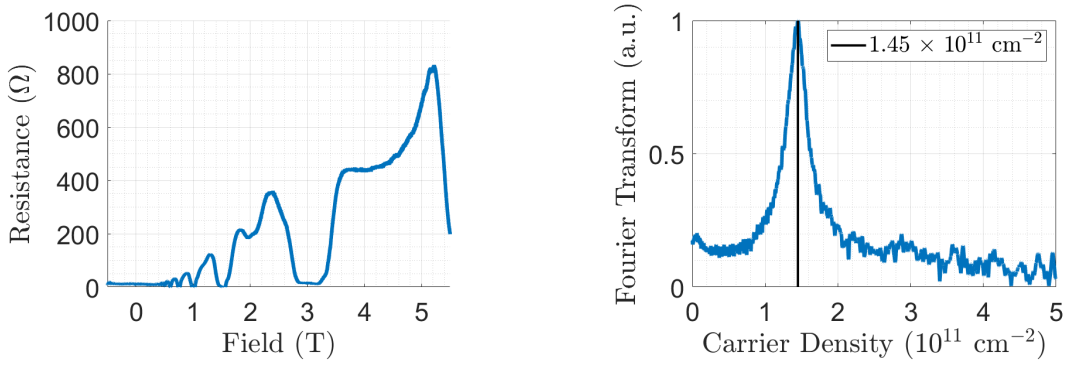

(a) (b)

Figure 6.2: a) Longitudinal resistance of the 300 μm square against magnetic field with $V_g = 0$. b) The associated Fourier transform, demonstrating a carrier density of 1.45×10^{11} cm^{-2}. Data between 0.001 T - 0.7 T was used to produce the Fourier transform.

Hall resistance against magnetic field is shown in Fig. 6.3. The corresponding carrier density found using the slope of this plot is 1.46×10^{11} cm^{-2}, in agreement with the carrier density from Shubnikov-de Haas oscillations. The basic characterisation demonstrated in Fig. 6.2 and Fig. 6.3 shows that this device is well behaved and suitable for localisation studies.

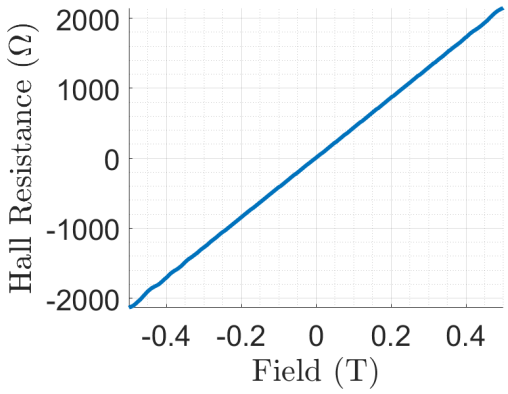

Figure 6.3: Hall resistance of the 300 μm square against magnetic field with $V_g = 0$. The associated carrier density is 1.46×10^{11} cm^{-2}.

6.1.2 5 μm Samples

Square devices of side length 5 μm were initially fabricated in a similar fashion to the 300 μm devices previously discussed. The only major differences being that electron-beam lithography was used and the mesa was defined via a dry etch, as discussed in section 4.6. This was done in order to reduce lateral etching which, unless a given etch is highly anisotropic, is unavoidable with wet etching. This itself was necessary as the width of the mesa attached to the corners of the squares was only 200 nm. With a wet etch of 90 nm, necessary to remove the GaAs/$Al_{0.33}Ga_{0.67}As$ interface, this mesa would have been laterally etched away.

The 5 μm devices, with squares defined by etching, were not able to be successfully measured. The current paths into the squares were most likely depleted due to their narrow width and associated edge effects. A more involved device design was therefore created, which did produce working devices. This design, instead of defining the square via an etched mesa, defined the square using gates. Three gates in total were used. It was necessary for the gates to overlap each other, so between each a 65nm layer of aluminium oxide was deposited via atomic layer deposition (ALD). See section 4.6 for details regarding this technique. Given there were three gates, there were two dielectric layers needed. The top-most gate was used to deplete the square, in an analogous fashion to the single gate of the 300 μm devices, and shall be referred to as the plunger gate. The middle gate defined the square and shall be referred to as the definer gate. Beneath both the definer and plunger gates was a third gate. This gate was necessary to screen the effects of the definer and plunger gates, in order to prevent pinching off at the corners of the squares and thus allow contact to be made with the squares. This gate shall be referred to as the enhancer gate. This gate was simply kept at 0 V. Aside from the enhancer gate in the corners, only the plunger gate covered the

square in its entirety.

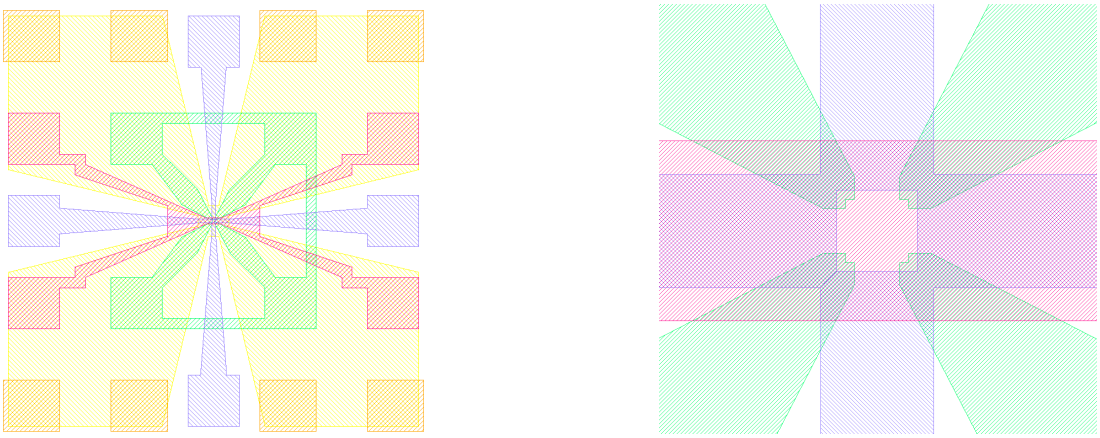

(a) (b)

Figure 6.4: Gate defined van der Pauw square design. a) The mesa is yellow with ohmic contacts orange. The enhancer gate is green, the definer gate is purple and the plunger gate is pink. b) Close up of a) showing the three gates used to define the central square.

The whole device design is shown in Fig. 6.4a. The mesa is shown in yellow. Ohmic contacts are in orange. Only one ohmic contact in each corner of the device was needed. The enhancer gate is in green with the definer gate in purple. The plunger gate is in pink. Four gate bonding pads for each gate were fabricated, in order to mitigate the issues related to bonding on top of a dielectric. A close up of the square itself is shown in Fig. 6.4b.

A processed device is shown in Fig. 6.5. Shown here are the three gates previously discussed. The difference in gate metal colour is due to the aluminium oxide between the gates. It is not clear from this image, but only the plunger gate covers the whole of the square, as depicted in Fig. 6.4b. The image also contains numbers labelling the four corners, referred to later when discussing various measurements.

Basic Hall effect characterisation of such a device can be seen in Fig. 6.6. In Fig. 6.6a the Hall resistance is plotted against perpendicular magnetic field. A 50

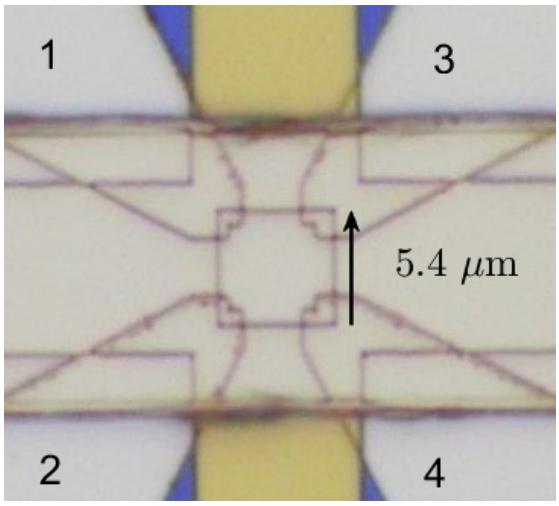

Figure 6.5: Gate defined van der Pauw square.

μV excitation, at 33.33 Hz, was applied between two diagonally opposite corners of the square. Specifically corners 1 and 4 of Fig. 6.5. The resultant current was measured. The Hall voltage between the other two corners was measured. This was done with the enhancer gate at 0 V, the definer gate at -0.9 V and the plunger gate at -0.6 V. A 16-bit DAC was used to apply these gate voltages. The measuring set up is as depicted in Fig. 5.4. From the slope of the plot the carrier denisty of the square, at this plunger gate voltage, is found to be 2.34×10^{10} cm^{-2}. The same measurement was repeated at other plunger gate voltages. The resultant plot of carrier denisty against plunger gate voltage is seen in Fig. 6.6b. As expected, the plot is linear. The rate of change of carrier density with gate voltage can simply be found from the slope of the plot. This value is expected to depend simply on the capacitance between the 2DEG of the square and the plunger gate. The rate of change is 2.26×10^{11} $\text{cm}^{-2}\text{V}^{-1}$. This agrees well with the theoretical value expected for a 130 nm aluminium oxide layer and a 90 nm layer of semiconductor material, which is 2.33×10^{11} $\text{cm}^{-2}\text{V}^{-1}$.

Finally, with respect to device characterisation, the high mobility nature of the wafer was used to confirm that the squares were being defined as intended.

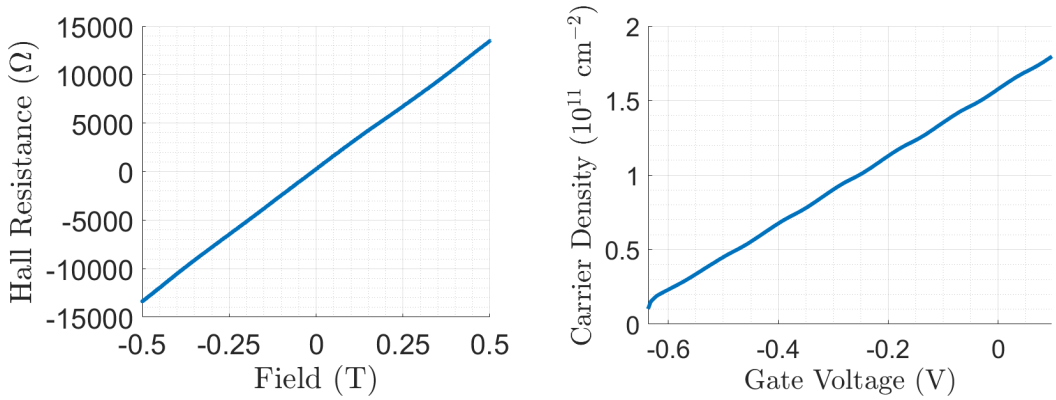

(a) (b)

Figure 6.6: a) Hall resistance of the 5 μm square against magnetic field with the enhancer gate at 0 V, the definer gate at -0.9 V and the plunger gate at -0.6 V. The associated carrier density is 2.34×10^{10} cm^{-2}. b) Carrier density against plunger gate voltage.

The mobility of the as grown wafer was 2.23×10^6 cm^{2}V^{-1}s^{-1}. Combined with a carrier density of 1.57×10^{11} cm^{-2}, the mean free path is therefore 15.3 μm. Thus electrons can travel a significant distance ballistically within the 5 μm squares. A measurement similar to a focusing measurement was therefore possible. An excitation voltage of 50 μ V, at 33.33 Hz, was applied between two corners on the same side of the square. Specifically corners 1 and 2 of Fig. 6.5. The voltage was measured between the corners of the square along the opposite edge, corners 3 and 4. The enhancer and plunger gates were at 0 V with the definer gate voltage at -0.9 V. The longitudinal voltage measured is plotted against perpendicular magnetic field in Fig. 6.7. At zero magnetic field the voltage is negative. That is, when the applied excitation is such that $V_1 - V_2 > 0$ then $V_3 - V_4 < 0$. Here V_i is the potential at corner i. Only as field increases does the voltage become positive. This is due to the ballistic nature of the transport. Upon entering the square, electrons travel ballistically for an average distance equal to the mean free path before significantly changing momentum. When entering the square, the average angle the incoming electrons will have is assumed to be 45^o with respect to the

sides of the square. Thus, with zero magnetic field, when entering via corner 1 and travelling without deflection, the majority of electrons will come into contact with corner 4 before corner 3. The chemical potential of corner 4 will therefore be higher than that of corner 3. This is opposite to the usual case in which device size is much larger than mean free path. However, when a field is applied the paths of the electrons are curved by the Lorentz force. One of the maxima in Fig. 6.7 is associated with the field at which electrons entering the square from corner 1 are focused directly to corner 3. As the excitation voltage is AC, the field of opposite sign is associated with electrons from corner 2 being focused directly to corner 4. As the electrons are assumed to exit and leave with an average angle of 45^o, the focused paths which are bent by the Lorentz force can be thought of as quarter circles. Thus once the cyclotron radius, $r = \hbar k_F/Be$, associated with this focusing is known, the effective square edge can be given by $\sqrt{2}r$. The field associated with the voltage maximum is 0.022 T. Thus with a carrier density of 1.57×10^{11} cm^{-2} it follows that $r = 2.98$ μm and the effective square side length is 4.2 μm. As this length is close to that of the lithographic length, the conclusion of this analysis, essentially, is that the square is defined as intended.

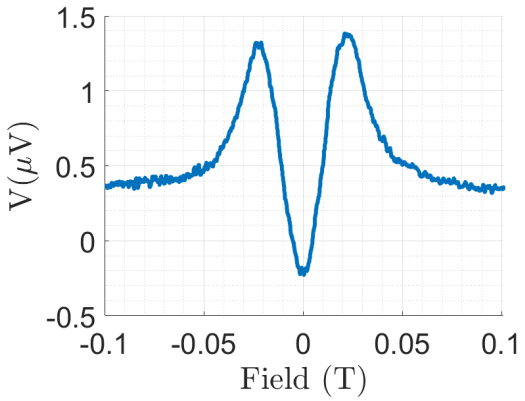

Figure 6.7: Focusing style measurement demonstrating the effective square side length to be 4.2 μm. An excitation voltage of 50 μV at 33.33 Hz was applied between corners 1 and 2 of Fig. 6.5. The resultant voltage between corners 3 and 4 was measured as perpendicular magnetic field was swept.

6.2 Localised Transport Measurements

Four terminal measurements of longitudinal resistivity and Hall resistance were made as a function of temperature. Just as with the high mobility characterisation, the set-up was as depicted in Fig. 5.4. However this time a lower excitation frequency was used, to reduce the impact of any parasitic capacitance. A 100 μV AC excitation was applied at 2 Hz. A 16-bit DAC was again used to vary gate voltages and, in turn, manipulate the Fermi level below the mobility edge. Naturally, devices became highly resistive. Resistances were measurable below 500 MΩ. At higher resistances, at 2 Hz, the parasitic capacitances of the coaxial cables and cryostat wiring became an issue. The current noise floor was $\sim 10^{-13}$ A. Magnetic fields of ± 0.5 T were applied when making Hall resistance measurements. The measured Hall resistances were anti-symmetrised in order to remove the mixing of the longitudinal signal. Longitudinal resistance measurements were also made at ± 0.5 T so as to compare with Hall resistances at the same field magnitude. This is necessary as applied magnetic field will affect the nature of the localised states and resultant transport.

6.2.1 300 μm Samples

Activated Carrier Density Results

Figure 6.8a displays resistivity, ρ, against the reciprocal of temperature, T^{-1}, for various gate voltages. On a semi-log plot, the data falls onto straight lines, indicating that the transport is an Arrhenius process. That is to say, the conductivity fits to (6.1) with $\gamma = 1$. At the lowest gate voltages, the fitted straight lines converge to the same infinite temperature intercept, $\sigma_0 = 3e^2/h$. This is indicative of a minimum metallic conductivity and is in keeping with the values previously reported in the literature, [14,16,122]. In general, as V_g decreases, the Fermi level

is pushed even further below the mobility edge. This increases the characteristic temperature, T_0, which varies between 43 K - 90K. A plot of $W = -d\log\rho/d\log T$ against T for $V_g = -0.213$ V is shown in Fig. 6.8b. If conductivity is of the form (6.1), $W = \gamma T_0^{\gamma} T^{-\gamma}$ and such a plot on a log-log scale should be a straight line with slope equal to $-\gamma$. This is the case and the slope is -1.07 ± 0.15, again indicating an Arrhenius transport mechanism.

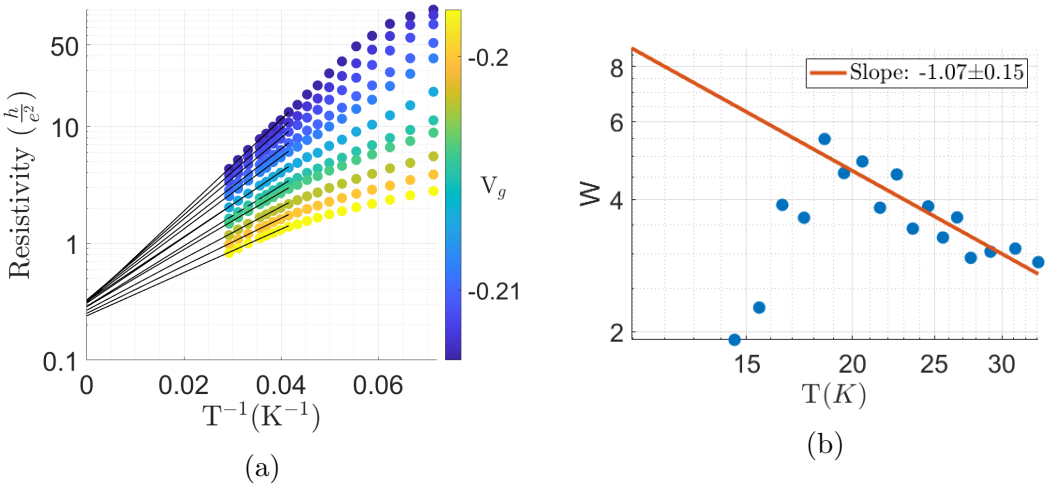

Figure 6.8: a) Arrhenius resistivity of 300 μm device demonstrated by plotting against T^{-1} on a semi-log scale. b) Plot of $W = -d\log\rho/d\log T$ against T for $V_g = -0.213$ V, again demonstrating Arrhenius behaviour.

So far, the Arrhenius behaviour presented is not original and, as discussed, similar findings have been reported numerous times in the literature. Although the convergence of the infinite temperature conductivity intercept, σ_0, is particularly interesting in the context of activation to a mobility edge, this too, as noted, has been observed previously. What is novel, however, is the behaviour of the Hall carrier density and Hall mobility. As shall be seen, their behaviour provide clear evidence of activation to a mobility edge. Such observations have not been reported in the literature.

The variation of Hall carrier density with the reciprocal of temperature, T^{-1}, is shown in Fig. 6.9a. The gate voltages are the same as in Fig. 6.8a. The carrier

densities, on a semi-log plot, fall onto straight lines. They thus appear to take an Arrhenius form, just like the conductivity. This observation, of an activated carrier density above a mobility edge, has not been reported before. Furthermore the mobility, shown in Fig. 6.9b, is gate independent. This is striking; the position of the Fermi level has no bearing on the mobility. This can be explained if all transport takes place at the mobility edge. Note that the mobility has a temperature dependence. In the context of transport via activation to a mobility edge, this may initially seem surprising. If σ and n are assumed to have the same characteristic temperature, then $\mu = \sigma/ne$ is expected to be a temperature independent constant. However, given that the very presence of a mobility edge in two dimensions is due to finite temperature effects, it is not unreasonable to claim that the states just above the mobility edge are highly temperature dependent. This would allow for both the mobility to have a temperature dependence and the inequality of carrier density characteristic temperature and conductivity characteristic temperature. A significant claim of this thesis is that due to an Arrhenius conductivity, Arrhenius carrier density and a gate independent mobility, clear evidence of transport via activation to a mobility edge has been observed for the first time.

The Arrhenius characteristic temperatures of the resistivity and carrier density are plotted against gate voltage in Fig. 6.10a. These temperatures are the slopes of the straight line fits in Fig. 6.8a and Fig. 6.9a. As the Fermi level is pushed further below the mobility edge, these characteristic temperatures increase. In the case of the carrier density, $k_B T_0$ is simply the energy separation between the Fermi level and the mobility edge. The difference between the resistivity and carrier density characteristic temperatures is also plotted and is seen to be approximately constant. Given that $\mu = \sigma/ne$, the difference is responsible for the temperature dependence of the mobility. The mobility is determined by the extended states

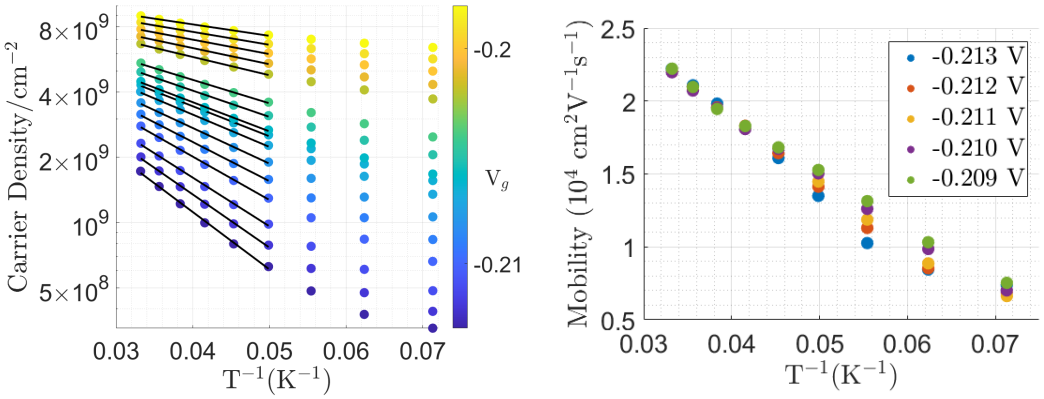

(a) (b)

Figure 6.9: a) Arrhenius Hall carrier density of 300 μm device demonstrated by plotting against T^{-1} on a semi-log scale. b) Mobility against T^{-1}, showing mobility is gate independent and thus independent of Fermi level.

just above the mobility edge, as previously discussed. Therefore, the temperature difference is the characteristic temperature of the extended state mobility. This explains its lack of dependence on Fermi level. Significantly, Fig. 6.10a appears to show a continuous transition between an activated carrier density, claimed for the first time in this work, and the supposed activated mobility regime of previous works in the literature. However, it is argued here that the transport is always via activation to mobility edge; what varies between the two regimes is whether carrier density or mobility dominates the resistivity temperature dependence. At the lowest gate voltages, and therefore lowest Fermi levels, it is the carrier density that dominates the resistivity temperature dependence. As Fermi level increases, the carrier density characteristic temperature decreases until it is the mobility that dominates the resistivity temperature dependence. In this later regime, it is the temperature dependence of the extended states that has the most influence of the resistivity temperature dependence and not the gap between Fermi level and mobility edge. In both regimes, the transport is consistently via activation to a mobility edge.

The ratio of the localised density of states, N, to the the constant extended density of states, $N_{ext} = m^*/\pi\hbar^2$, is plotted against V_g in Fig. 6.10b. The localised density of states were determined using $N = (C_g/k_B)dV_g/dT_0$, as first demonstrated in [26]. Here T_0 is the carrier density characteristic temperature and C_g is the change in 2DEG density per unit gate voltage. The derivative, dV_g/dT_0, was evaluated after first fitting to T_0 against V_g. As the Fermi level is pushed further into the band tail the density of states reduces, as expected. The value of N/N_{ext} can be seen to vary between 0.05-0.2. Values in the literature typically have $N \approx N_{ext}$ when making similar measurements of localised transport, as first seen in [26]. It is possible that the lower values of N/N_{ext} accessed in this work have allowed the Arrhenius carrier density and the previously discussed transition to be observed.

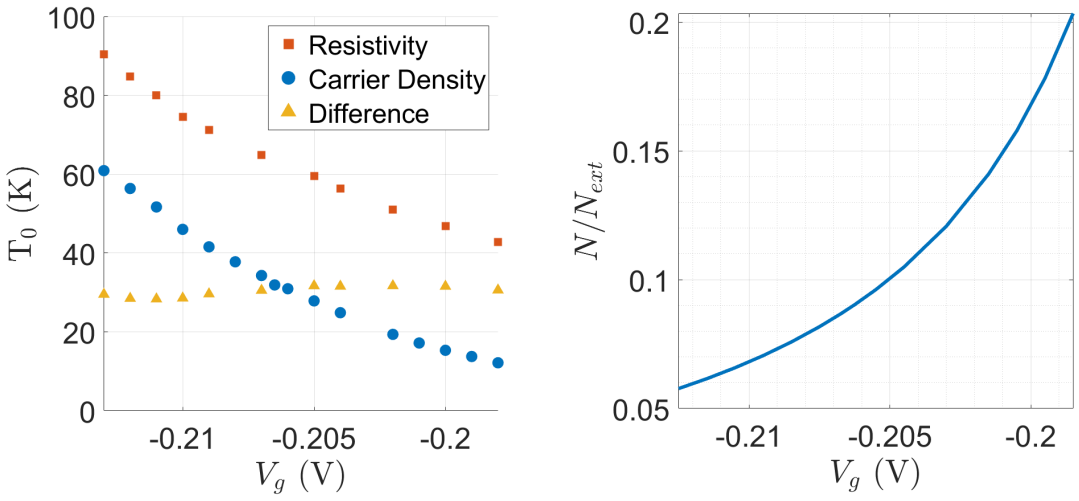

Figure 6.10: a) Arrhenius characteristic temperatures of the resistivity, carrier density and the difference against gate voltage. The difference is effectively the mobility characteristic temperature. It is strikingly constant and thus independent of Fermi level. b) The ratio of the density of states, N, to the extended state denisty of states, $N_{ext} = m^*/\pi\hbar^2$, against gate voltage. The ratio was calculated using $N = (C_g/k_B)dV_g/dT_0$ where T_0 is the carrier density characteristic temperature and C_g is the change in 2DEG density per unit gate voltage.

The lifetime at the mobility edge, τ_{edge}, is expected to depend exponentially on the separation between mobility edge and Fermi level. That is to say, $\tau_{edge} \propto \exp[-(E_\mu - E_F)/k_B T]$. Here E_F is the Fermi energy and E_μ is the mobility edge. In this work, the mobility temperature dependence was found to be independent of the Fermi level. Thus, edge lifetime does not appear to affect transport in the extended states just above the mobility edge. It is therefore expected that the elastic scattering lifetime is less than the edge lifetime; the edge lifetime is irrelevant with respect to transport. This is seen to be true regardless of whether carrier density or mobility dominate the resistivity temperature dependence.

Efros Shklovskii Hopping Results

At lower temperatures, the transport was observed to be via Efros-Shklovskii hopping, as shown in Fig. 6.11. To achieve these lower temperatures, measurements were made in a dilution refrigerator as opposed to the 1.5 K system used to take the data in Fig. 6.8 and Fig. 6.9. Both of these cryogenic systems are discussed in section 5.1. This means that the results are associated with different cool-downs. Different cool-downs result in different 2DEG populations. The main consequence of this is that gate voltages cannot necessarily be compared between different cool-downs.

Figure 6.11a shows resistivity against $T^{-1/2}$ for various gate voltages, on a semi-log plot. The data falls onto straight lines indicating the conductivity has the form of (6.1) with $\gamma = 1/2$. This is indicative of Efros-Shklovski hopping. The characteristic temperature, T_0, varies between 1.5 K - 8.8 K. Figure 6.11b shows W plotted against T, for $V_g = -0.19$. The straight line of slope -0.49 ± 0.09 is again indicative of Efros-Shklovski hopping.

Figure 6.12a shows the variation of the Hall constant, R_H, with temperature. The gate voltages are the same as in Fig. 6.11a. The temperature dependence

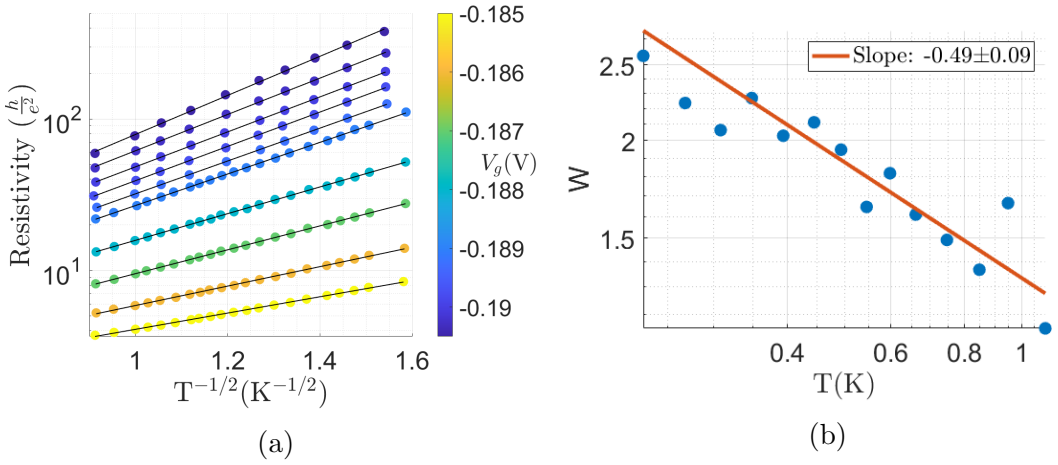

Figure 6.11: a) Efros-Shklovskii hopping resistivity demonstrated by plotting resistivity against $T^{-1/2}$ on a semi-log scale. b) Plot of $W = -d\log\rho/d\log T$ against T for $V_g = -0.19$ V, again demonstrating Efros-Shklovskii hopping behaviour.

becomes more significant as V_g decreases. The corresponding Hall mobilities are plotted against $T^{-1/2}$ in Fig. 6.12b. Straight lines thus indicate the mobility has the same general form as the conductivity. This is the case for the highest gate voltages plotted. The temperature dependence of the Hall mobility for the lowest gate voltages is not as clear. As discussed in section 2.8.1, there is no accepted model explaining the Hall effect in the hopping transport regime. The results presented here, it could be argued, support theoretical and experimental works that propose a mobility of the same form as the conductivity but with a different characteristic temperature. As shown in Fig. 6.12b, the ratio of mobility characteristic temperature to conductivity characteristic temperature, T_0^{μ}/T_0^{σ}, varies between 0.41 - 0.73. As previously discussed, the corresponding values in Ge/Si quantum dots and reduced graphene oxide are 0.31 and 0.49 respectively [89, 90]. The theoretical prediction is a ratio of 0.09 [89]. The ratios reported here are thus closer to other experimental values in the literature than to theoretical predictions.

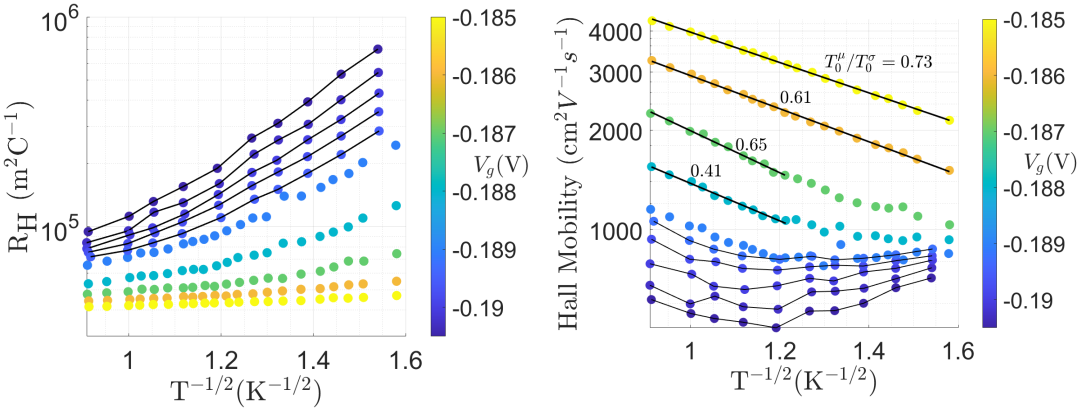

Figure 6.12: a) Hall constant plotted against $T^{1/2}$. Lines used for clarity, to indicate same data series. b) Hall mobility plotted against $T^{1/2}$. The ratios of mobility characteristic temperature to conductivity characteristic temperature, T_0^μ/T_0^σ, are shown.

6.2.2 5 μm Samples

The 5 μm samples were studied in order to investigate potential effects related to sample size. Prior to measuring the 300 μm samples it was hypothesised that the unusual, yet consistent, results in the literature reporting an activated mobility as opposed to an activated carrier density could be related to the finite lifetime at the mobility edge. If the edge lifetime is smaller than the elastic scattering time, $\tau_{edge} < \tau$, it is the former that determines the mobility which is thus given by $\mu = e\tau_{edge}/m^*$. In this case, it would be interesting to observe how transport properties such as Hall mobility and Hall carrier density are affected when sample size is similar to or less than the lengthscale associated with the edge lifetime. Notwithstanding this reasoning, the 300 μm results presented in section 6.2.1 demonstrated transport via activation to a mobility edge in which the edge lifetime is irrelevant. It was the elastic scattering time, τ, which determined the mobility. Furthermore, the unusual results from the literature were shown to be potentially explained by a transition in which carrier density and extended state mobility

compete to dominate the resistivity temperature dependence. Regardless of this, the investigation of sample size was still deemed worthwhile, hence the 5 μm sample study.

Carrier density against the reciprocal of temperature, T^{-1}, is shown in Fig. 6.13a. Straight lines indicate Arrhenius behaviour. Various data series associated with different plunger gate voltages are plotted. Regardless of plunger gate voltage, the enhancer gate voltage was 0 V and the definer gate voltage was -0.9 V; the enhancer and definer gate voltages were the same as in Fig. 6.7. Below 5 K the carrier density appears activated with characteristic temperature increasing as V_g, and thus Fermi level, is reduced. The characteristic temperature varies between 1.2 K - 5.9 K.

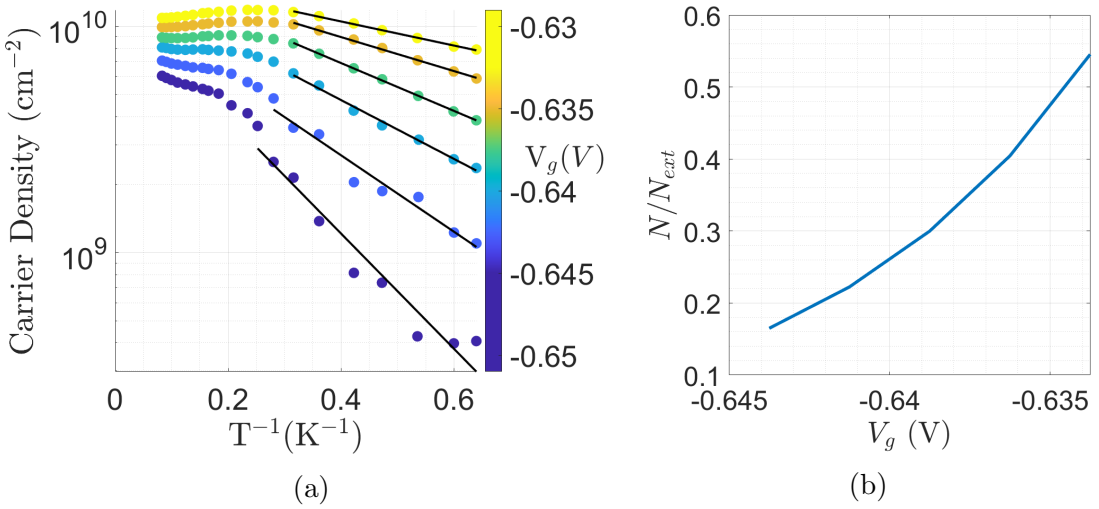

Figure 6.13: a) Carrier density against T^{-1}. b) Ratio of the density of states, N, to the extended state denisty of states, $N_{ext} = m^*/\pi\hbar^2$, against gate voltage.

The ratio of the density of states, N, to the extended state density of states, $N_{ext} = m^*/\pi\hbar^2$, is shown in Fig. 6.13b. The density of states were calculated in the same way as described in section 6.2.1. Measurement issues, seemingly related to the contacts to the central square, meant that lower gate voltages were unable to be investigated. Thus it was not possible to probe further into the band tail.

Below the displayed gate voltages it was not possible to pass a current though the device. It is possible that this was due to the plunger gate pinching off the contacts to the square regardless of the screening provided by the enhancer gate. Because the device stopped conducting below the gate voltages shown, it was not possible to achieve the values of N seen in Fig. 6.10b. Due to a temperature dependent carrier density being observed, the initial results presented here are promising. However, further work is required to allow one to probe further into the band tail in these small devices.

Chapter 7

Electron-Phonon Decoupling in GaAs

In this chapter the breakdown of the quantum Hall effect, in the context of electron overheating, is investigated. As discussed in section 2.8.3 there appears to be a, perhaps trivial, issue of semantics in the literature regarding the breakdown of the quantum Hall effect. This terminology is often used to refer to a sudden increase in longitudinal resistance, using a standard Hall bar geometry, as applied current increases past a critical point. This occurs in the quantum Hall regime meaning the filling factor, ν, is an integer. The Hall resistance also deviates from its quantised value of $h/\nu e^2$. This is an edge state effect; for some reason, that is yet to be agreed upon, the ballistic edge state transport is suddenly lost. However, the same terminology is also used in the case of a Corbino geometry. In this instance the breakdown refers to a sudden increase in conductivity as applied bias increases, again with integer filling factor. In such a geometry, the transport is independent of edge states and the effect is instead associated with the localised states of the disorder broadened Landau levels. In this work, it is this later effect which is investigated. It will be argued that the same phenomenolog-

ical heat-balance equation, which has been successfully used to explain electron overheating and hysteretic current jumps in disordered thin films, can also be applied to transport between the localised states of disorder broadened Landau levels. In turn, it will argued that the breakdown of the quantum Hall effect, in a Corbino geometry, is due to electron-phonon decoupling. See section 2.7.3 for a discussion regarding electron overheating and hysteretic current jumps. Specifically, by measuring current-voltage characteristics, the model described by (2.67) will be tested. Overheating explanations of the breakdown of the quantum Hall effect have been attempted previously. However, as discussed in section 2.8.3, standard Hall bar geometries were used and the explanations were not successful. The work presented here is, to the author's knowledge, the first that systematically tests an overheating model in a quantum Hall system using a Corbino type geometry.

Typically, when investigating the integer quantum Hall effect, it is even filling factors that are studied. That is, $\nu = 2i$ where i is an integer. In this way, the energy gap to the next Landau level is given by the cyclotron energy, $\hbar eB/m^*$, and not the Zeeman energy. In GaAs two-dimensional electron gases the ratio of the cyclotron energy to the Zeeman energy is ~ 70 [123]. Having a larger energy gap typically means that effects are more pronounced at finite temperature. In this work, a breakdown was not observed at even filling factors. However, as shall be shown, the corresponding temperature dependence of the resistance, R, took on a power law form when $\nu = 2i$. That is, $R = AT^{-\alpha}$ with $\alpha > 0$. Using the same analysis discussed in section 2.7.3, such a temperature dependence is predicted not to lead to current jumps as applied bias is swept. The lack of a breakdown, with this temperature dependence, therefore strengthens the case for the applicability of the overheating model. The majority of this chapter focuses on odd filling factors, meaning $\nu = 2i+1$. At such values of ν, breakdown was observed; current-

voltage characteristics did show large hysteretic current jumps. The observed transport was that of Efros-Shklovskii hopping with odd filling factor. This means the gap to the next Landau level is irrelevant. Fittings to the overheating model described by (2.67) will be presented. They will be shown to strongly support both the model and therefore electron-phonon decoupling. Secondary current jumps will also be discussed in the context of many-body localisation (MBL).

Figure 7.1 can be used to potentially explain why even filling factors displayed qualitatively different transport to that of the odd filling factors. As discussed, they displayed power law resistances as opposed to Efros-Shklovskii hopping. They also displayed higher resistances than their adjacent odd counterparts. This could be do to the Zeeman split disorder broadened Landau levels overlapping. In this case, the density of states at the Fermi level will be greater with odd filling factor compared to even filling factor, as depicted in Fig. 7.1. A lower density of states is expected to lead to a lower conductivity and could explain the different transport mechanism.

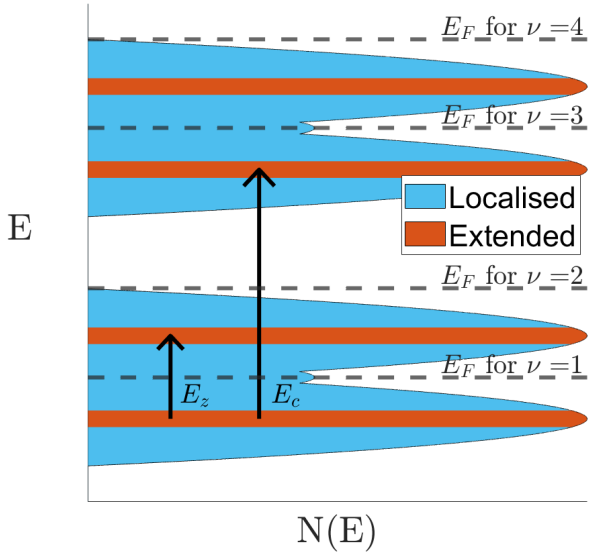

Figure 7.1: Landau level density of states depicted if spin split levels overlap. This leads to a greater density of states for odd values of ν compared to even ν. Fermi levels, E_F, at different values of ν are labelled.

7.1 Device Fabrication and Basic Characterisation

The material used in this work was an $Al_{0.33}Ga_{0.67}As$ heterostructure, with the 2DEG residing at the $GaAs/Al_{0.33}Ga_{0.67}As$ boundary, 90 nm below the wafer surface. The wafer structure is shown in Fig. 3.3a. The density of the silicon dopants in the 40 nm doped layer is 9×10^{17} cm^{-3}. The device used is shown in Fig. 7.2. The mesa and ohmics were fabricated as detailed in section 4.6. Contacts were arranged both in the centre and around the edges of the device. The structure allowed for basic magnetotransport measurements, to confirm the suitability of the wafer, as well as Corbino-esque measurements to probe the localised states of the disorder broadened Landau levels. Specifically, with respect to basic characterisation, a four-terminal longitudinal resistance was measured in order to demonstrate the well behaved nature of the Shubnikov-de Haas oscillations and determine the carrier density.

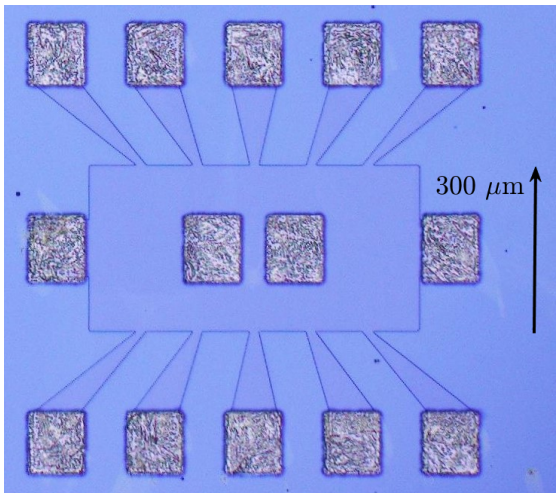

Figure 7.2: Device to carry out both measurements of Shubnikov-de Haas oscillations as well as measurements of transport within disorder broadened Landau levels.

Longitudinal resistance against magnetic field is plotted in Fig. 7.3a. The

minima of the Shubnikov-de Haas oscillations fall to zero, indicating the absence of any parallel conduction. The set up was as depicted in Fig. 5.4, with a constant current of 50 nA being applied at 33.33 Hz. The Fourier transform of the longitudinal resistance, using data between magnetic fields of 0.001 T - 0.7 T, is shown in Fig. 7.3b. The carrier density, n, is shown to be 1.64×10^{11} cm^{-2}. The magnetic field associated with filling factor ν is therefore given by $nh/e\nu = (6.80/\nu)$ T.

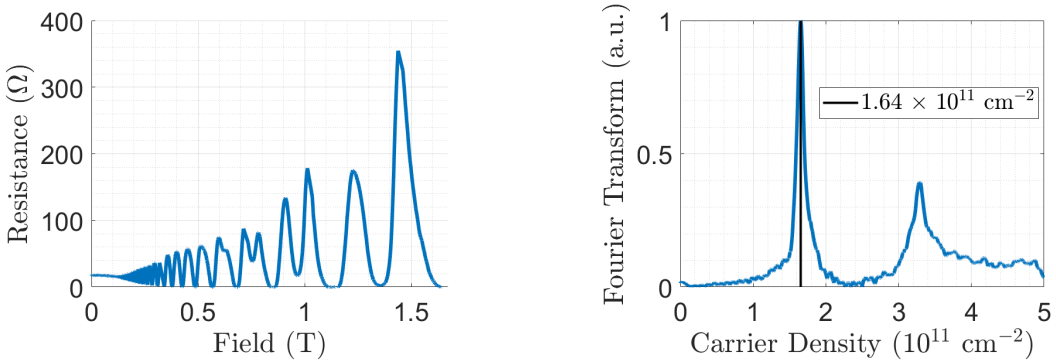

(a) (b)

Figure 7.3: a) Longitudinal resistance against magnetic field demonstrating the minima of the Shubnikov-de Haas oscillations going to zero and therefore a lack of parallel conduction. b) The associated Fourier transform, demonstrating a carrier density of 1.64×10^{11} cm^{-2}. Data between 0.001 T - 0.7 T was used to produce the Fourier transform.

7.2 Localised Transport

In the remainder of this chapter, measurements of the localised transport within the disorder broadened Landau levels at different filling factors will be presented. Fittings will be made to the heat-balance model, (2.67), to justify the claim that electron-phonon decoupling explains the breakdown of the quantum Hall effect. Critical temperatures will also be compared to theoretical values given by (2.70).

To avoid the ballistic edge states, the transport between a central contact and an edge contact was measured. The measurements were necessarily two terminal.

The parasitic contact resistances, ~ 1 kΩ, were negligible compared to the overall resistances. Current-voltage characteristics were measured using a Zurich MFLI to apply a DC bias and a Keithley 6514 electrometer to measure current. The current noise floor was ~ 0.1 pA. In the linear regimes of the characteristics, close to zero bias, the electron temperature, T_{el}, is considered equal to the lattice temperature, T_{ph}. The resistances, taken from the linear regimes, were then used to produce resistivity temperature dependences. These dependences were then used to determine both the mechanism of transport and the associated characteristic temperature. A typical characteristic at low biases is shown in Fig. 7.4. This was measured with $\nu = 5$ at 110 mK. The polynomial fitting used to determine the slope of the linear regime is also shown. The corresponding ohmic resistance is 8.4 GΩ. Note the DC voltage offset. It is common for there to be a non-zero current when applied bias is meant to be zero. This current is known as the input bias current of the measuring instrument. This is another advantage of measuring current-voltage characteristics; the offset can be taken into account by shifting the point of zero DC bias.

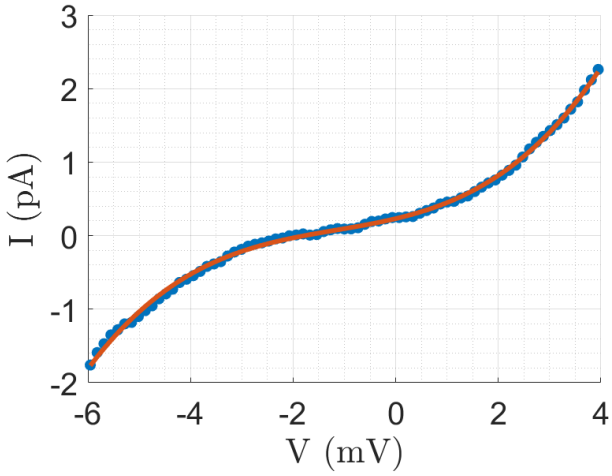

Figure 7.4: Typical current-voltage characteristic measured with $\nu = 5$ at 110 mK.

7.2.1 Filling Factor Eight

As discussed in the introduction to this chapter, when studying the quantum Hall effect it is the even filling factors that are typically studied. This is so that the gap to the next Landau level will be the cyclotron energy gap, as opposed to the Zeeman energy gap. In this work, even filling factors did not display jumps in their current-voltage characteristics. However, this can be explained, in the context of electron overheating, using the resistivity temperature dependences. Such a dependence, with resistivities taken from the linear regime of current-voltage characteristics, is shown in Fig. 7.5, for $\nu = 8$. At lower even values of ν (6, 4 and 2) the resistances were too large to be measured in the dilution refrigerator, meaning they were larger than 100 GΩ. In Fig. 7.5, resistivity is plotted against temperature on a log-log scale. The data falls onto a straight line; the resistivity has a power law dependence on temperature. That is, $\rho = AT^{-\alpha}$ with $A = 725\ h/e^2$ and $\alpha = 5.52$.

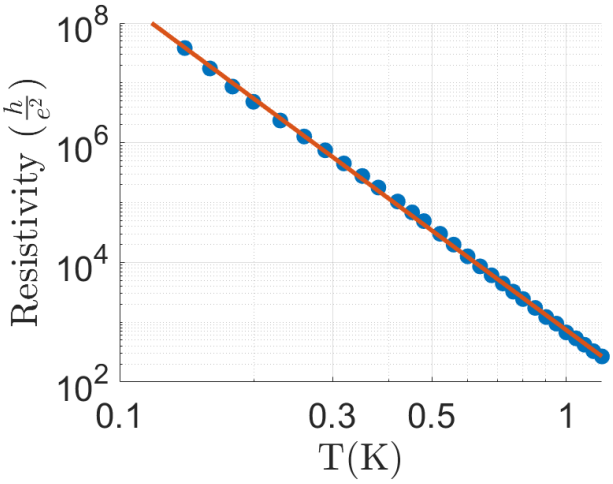

Figure 7.5: Resistivity plotted against temperature on a log-log scale at $\nu = 8$. The fitted line is a power law dependence which takes the form $\rho = AT^{-\alpha}$ with $A = 725\ h/e^2$ and $\alpha = 5.52$

Such a temperature dependence, using the heat-balance model, will not lead

to current jumps in the current-voltage characteristics. To show this, (2.67) is applied in the case of such a dependence resulting in,

$$V^2 = A\Gamma\Omega(T_{el}^{\beta} - T_{ph}^{\beta})T_{el}^{-\alpha}. \tag{7.1}$$

If a current jump is to exist, V^2 as a function of T_{el} should have a form similar to the yellow trace in Fig. 7.6. In this case, as applied bias, V, is swept there will be a discontinuity in T_{el} and a resultant jump in current. For V^2 to have such a form, there must necessarily be at least two local extrema in the right hand side of (7.1), as a function of T_{el}. It can be shown that with a power-law resistivity temperature dependence, this will not be the case. To find the extrema of the right hand side of 7.1, its derivitive with respect to T_{el} is set to zero resulting in,

$$(\beta - \alpha)T_{el}^{\beta-\alpha-1} + \alpha T_{ph}^{\beta} T_{el}^{-\alpha-1} = 0. \tag{7.2}$$

Rearranging (7.2) results in,

$$T_{ph}^{\beta} = (1 - \beta/\alpha)T_{el}^{\beta}. \tag{7.3}$$

If $\beta > \alpha$, (7.3) will never be satisfied due to the physical constraints that $T_{ph} > 0$, $\beta > 0$ and $\alpha > 0$. If $\alpha > \beta$, for a given value of T_{ph}, there is only one value of T_{el} for which (7.3) holds. Regardless, therefore, of the values of β and α, there are never two local extrema in the right hand side of 7.1 as a function of T_{el}. The general dependence of V^2 on T_{el}, in both cases, is shown in Fig. 7.6. The general power law dependence, $\rho = AT^{-\alpha}$, will never lead to current jumps in the current-voltage characteristics. In conclusion, the lack of current jumps while filling factor is even, can be explained by the phenomenological heat-balance equation, (2.67), and the measured power law resistivity temperature dependence. Because of this,

odd filling factors are the focus of this chapter.

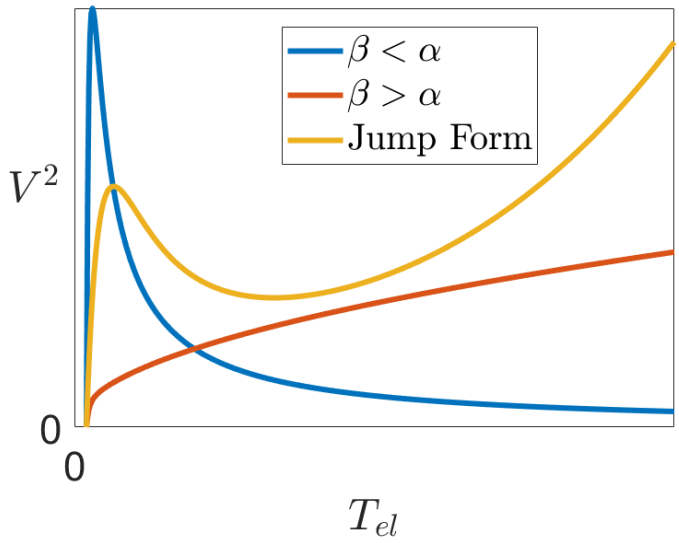

Figure 7.6: Demonstration that $\rho = AT^{-\alpha}$ will never lead to current jumps in current-voltage characteristics. The necessary form of V^2 against T_{el} is shown in yellow. Here there exists a region of bias in which there are three possible electron temperatures. This is not the case with a power law resistivity dependence, shown in blue and red.

7.2.2 Filling Factor Five

Current voltage characteristics with $\nu = 5$, meaning the perpendicular magnetic field was 1.36 T, are displayed in Fig. 7.7a at various lattice temperatures, T_{ph} . In all of the characteristics shown, the bias was swept from negative to positive values. Primary current jumps of over three order of magnitude are present. There is also clear hysteresis. The qualitative form of the characteristics is similar to those measured in disordered thin films, which were ascribed to electron phonon decoupling. They also appear similar to theoretically predicted current-voltage characteristics, produced using (2.67). See section 2.7.3 and [21, 22, 81, 83]. The dependence on T_{ph} is much stronger at the currents below the jumps, as opposed to above. That measurements can be made below the jumps is crucial in allowing a systematic analysis of the heat-balance model described by (2.67). At lower

values of ν, resistances were too large below the jumps, resulting in current being drowned out by the ~ 0.1 pA noise floor. Figure 7.7b shows current-voltage characteristics taken by sweeping in both directions, at 65 mK. This plot is included to demonstrate the clear hysteresis and emphasise the clean nature of the jumps.

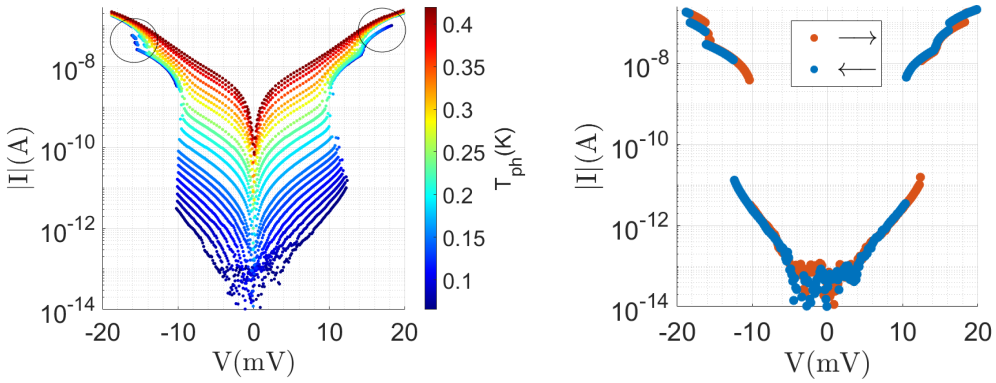

Figure 7.7: Current-voltage characteristics with $\nu = 5$. a) Bias voltage was swept from negative to positive values. Sweeps at different lattice temperatures are shown. Secondary jumps are circled. b) Bias voltage swept in both directions at 65 mK.

The reasoning behind the secondary jumps, which are circled in Fig. 7.7a, is unclear. They are reminiscent of the secondary jumps observed experimentally in a quantum dot array [124]. Theoretical work, which used an array of metallic islands to model the insulating side of a superconductor-insulator transition, produced qualitatively similar secondary jumps [125]. Alternatively, the secondary jumps could be due to a non-uniform spatial distribution of electron temperature which persists at currents above the primary jump. The secondary jumps, in this instance, would be associated with the areas of lower electron temperature being heated to the temperature of the hottest areas. This would be significant with respect to many-body localisation. As discussed in section 2.7.3, one of the proposed signatures of such a phase of matter is a bistability in electron temperature [21]. Further work involving samples of different sizes could provide more

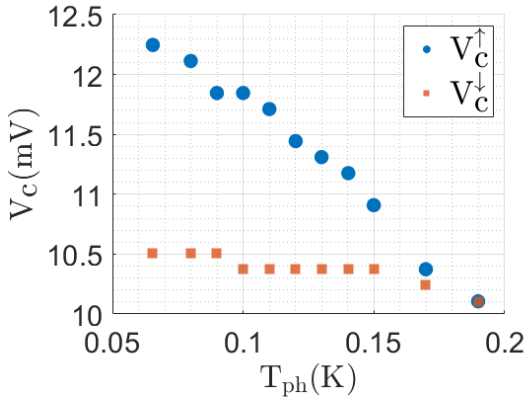

Figure 7.8: The primary critical jump voltages are plotted against lattice temperature.

insight. Assuming a non-uniform temperature distribution, larger samples should lead to even more areas that resist the overheating associated with the primary jump, leading to either more secondary jumps, larger secondary jumps or both.

The critical voltages at which the primary downward current jumps occur, $V_c^{\downarrow}$, are seemingly invariant with temperature. This is not true for the upward critical voltages, $V_c^{\uparrow}$. This is demonstrated in Fig. 7.8. This in keeping with the overheating model, (2.67). See Fig. 2.10 for a theoretical example of a critical voltage dependence on T_{ph}. In the low current state the electron system temperature is very close to the lattice temperature and the electron system and the phonon system are described as being coupled. The upward jump out of this state, therefore, depends strongly on T_{ph}. However, above the primary jump, the two systems are considered decoupled. The electron system has been overheated. In this case, the downward jump out of this state is almost independent of T_{ph}.

Before fitting to the heat-balance equation, (2.67), it is necessary to determine the resistivity temperature dependence. As previously discussed, it is assumed that $T_{el} = T_{ph}$ in the linear regime of the characteristics, close to zero bias. In this regime, the electron temperature and lattice temperature do not need to be differentiated and temperature, T, can be considered. The temperature depen-

dence of these linear regime resistivities is shown in Fig. 7.9a. Here resistivity is plotted against $T^{-1/2}$ on a semi-log plot. The straight line means a good fit to $\rho = \rho_0 \exp\left[(T_0/T)^{1/2}\right]$ indicating Efros-Shklovskii hopping. From the slope and intercept, $T_0 = 39$ K and $\rho_0 = 0.022\ h/e^2$. The same data and same fit is shown in Fig. 7.9b. Here resistivity is plotted against T.

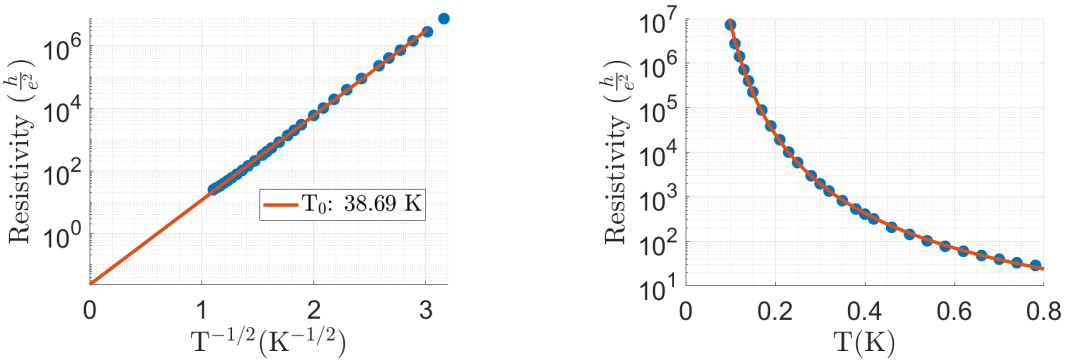

Figure 7.9: Resistivity temperature dependence demonstrating Efros-Shklovskii hopping at $\nu = 5$. a) Resistivity against $T^{-1/2}$ on a semi-log scale. The straight line indicates Efros-Shklovskii hopping. The straight line fit to $\rho = \rho_0 \exp\left[(T_0/T)^{1/2}\right]$ has parameters $T_0 = 39$ K and $\rho_0 = 0.022\ h/e^2$. b) the same data as in a) plotted against T.

The characteristic temperature, $T_0 = 39$ K, can be used to find the hopping length [71],

$$r_{ES} = \frac{\xi}{4} (T_0/T)^{1/2}, \tag{7.4}$$

where ξ is the localisation length given by

$$\xi = \beta_d e^2 / 4\pi\kappa\epsilon_0 T_0 k_B. \tag{7.5}$$

Here $\beta_2 \approx 6$, as discussed in section 2.6.4. Thus $\xi = 220$ nm and $r_{ES} = 1.3\ \mu$m at 65 mK, the lowest temperature measured at. The hopping distance can be taken as the electron-phonon length as this distance is simply the spatial separation between electron-phonon interaction events. To be able to apply the concept of

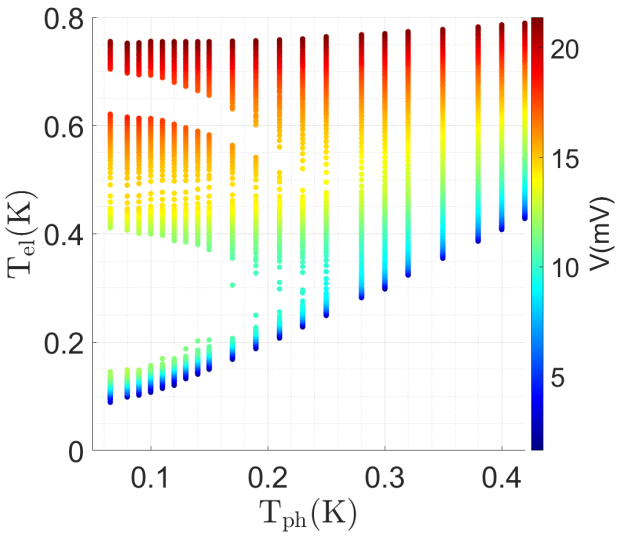

Figure 7.10: Electron temperature against phonon temperature at different bias voltages. Note the excluded regions of temperature associated with both the primary jumps and the secondary jumps.

electron-phonon decoupling, the hopping distance must therefore be less than the size of the sample. This is the case.

The resistivity temperature dependence can be used to find electron temperatures as a function of V/I in the non-linear regime of the characteristics. The dependence is simply inverted, such that T_{el} is a function of $R = V/I$. That the non-linear nature of the characteristics is purely due to electron overheating is a central assumption of the heat-balance model. In Fig 7.10, the resultant values of T_{el} are shown plotted against T_{ph}, at different bias values. Below a critical lattice temperature, $T_{ph}^{c} \approx 200$mK, and centred around 300 mK in electron temperature, there exists a region of excluded electron temperatures. This region is associated with the primary current jumps. When $T_{ph} < T_{ph}^{c}$, the electron system cannot take on the electron temperatures within the excluded region. Other excluded regions, associated with the secondary jumps, are also visible. At the highest biases, T_{el} is close to being independent of T_{ph}. Close to zero bias $T_{el} \approx T_{ph}$. At such biases the characteristics are approximately linear.

The values of T_{el}, found essentially as a function of bias voltage, V, and current, I, can now be used to verify the heat balance model, (2.67). This can be rewritten as

$$P = \Gamma\Omega(T_{el}^{\beta} - T_{ph}^{\beta}), \tag{7.6}$$

where $P = IV$ is power dissipated by the sample. What follows is essentially the main point of this chapter; the data fits well to (7.6) resulting in the current-voltage characteristics being ascribed to electron-overheating. Crucially, the data spans the current jumps, meaning that they are ascribed to overheating and, in this case, electron-phonon decoupling.

Figure 7.11a shows power plotted against T_{el}, at numerous lattice temperatures, T_{ph}. At the highest values of T_{el} included in this plot it should hold that $T_{el}^{\beta} \gg T_{ph}^{\beta}$, assuming a value of β similar to those seen in the literature. Values of 4, 5 and 6 have been reported [22, 81, 126, 127]. In this case $P \approx \Gamma\Omega T_{el}^{\beta}$ and power plotted against T_{el} should be a straight line with slope β. This can be seen in Fig. 7.11a. A straight line of slope 6 is included for reference. Another way of determining model suitability, which is not restricted to $T_{el}^{\beta} \gg T_{ph}^{\beta}$, is to plot power against $T_{el}^{\beta} - T_{ph}^{\beta}$. Such a plot is seen in Fig. 7.11b, where multiple values of β are tested. Note that each series is the same data, just plotted with a different value of β. The data itself is the same as in Fig. 7.11a. If (7.6) is satisfied, the data should fall onto a straight line of slope unity on a log-log scale. This is indeed the case for $\beta = 6$, here the slope of the fitted straight line is 0.98 ± 0.01. The value of $\Gamma\Omega$ is given by the intercept. As discussed in section 2.7.3, Γ is the , the phenomenological electron-phonon coupling constant and Ω is the area of the sample. When $\beta = 6$ the value of Γ is equal to 0.14 $\mathrm{Wm^{-2}K^{-6}}$.

This intercept can then be used to plot $IV + \Gamma\Omega T_{ph}^{\beta}$ against T_{el}. Such plots are seen in Fig. 7.12. If the data fits to (7.6), the plot should be a straight line

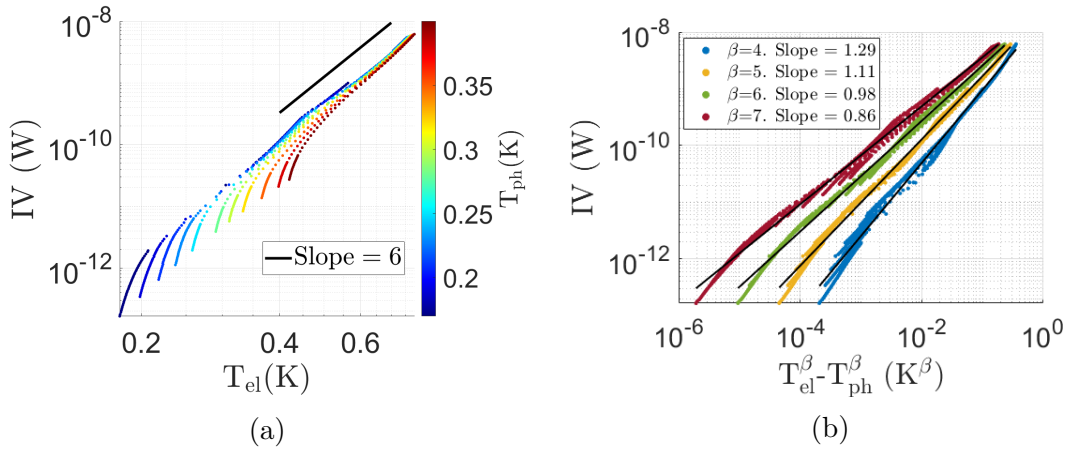

Figure 7.11: a) Power against electron temperature on a log-log scale. When $T_{el} \gg T_{ph}$, this should be a straight line of slope β. A line with slope 6 is also shown for comparison. b) Power against $T_{el}^{\beta} - T_{ph}^{\beta}$. Each series is the same data, just with a different β. If the overheating model of (7.6) is satisfied, this should be a straight line of slope 1. When $\beta = 6$, the slope is 0.98. Note that the data spans the current jumps.

with slope β. This is the case for $\beta = 6$, see Fig. 7.12c. The slope of the fitted straight line is 5.95 ± 0.01.

The data in Fig. 7.11 and Fig. 7.12 spans the large current jumps seen in Fig. 7.7. This is quite striking; the success of the fittings with $\beta = 6$ is strong evidence that the phenomenological heat-balance model is able to accurately explain the highly non-linear current voltage characteristics. Most significantly, the model is able to explain the large hysteretic current jumps. As a result, these jumps are ascribed to electron-phonon decoupling.

Another method employed to verify the model is to compare the predicted critical lattice temperatures, T_{ph}^{c}, with the experimentally observed values. At lattice temperatures below T_{ph}^{c}, current jumps are observed. The predicted values are given by (2.70). They depend on β, the characteristic temperature T_0 and γ, which depends on the transport mechanism. Applying (2.70) with the observed parameters $\beta = 6$ and $\gamma = 1/2$ leads to $T_{ph}^{c}/T_0 = 3.9 \times 10^{-3}$. Current-voltage characteristics were measured and the previous analysis was repeated at other

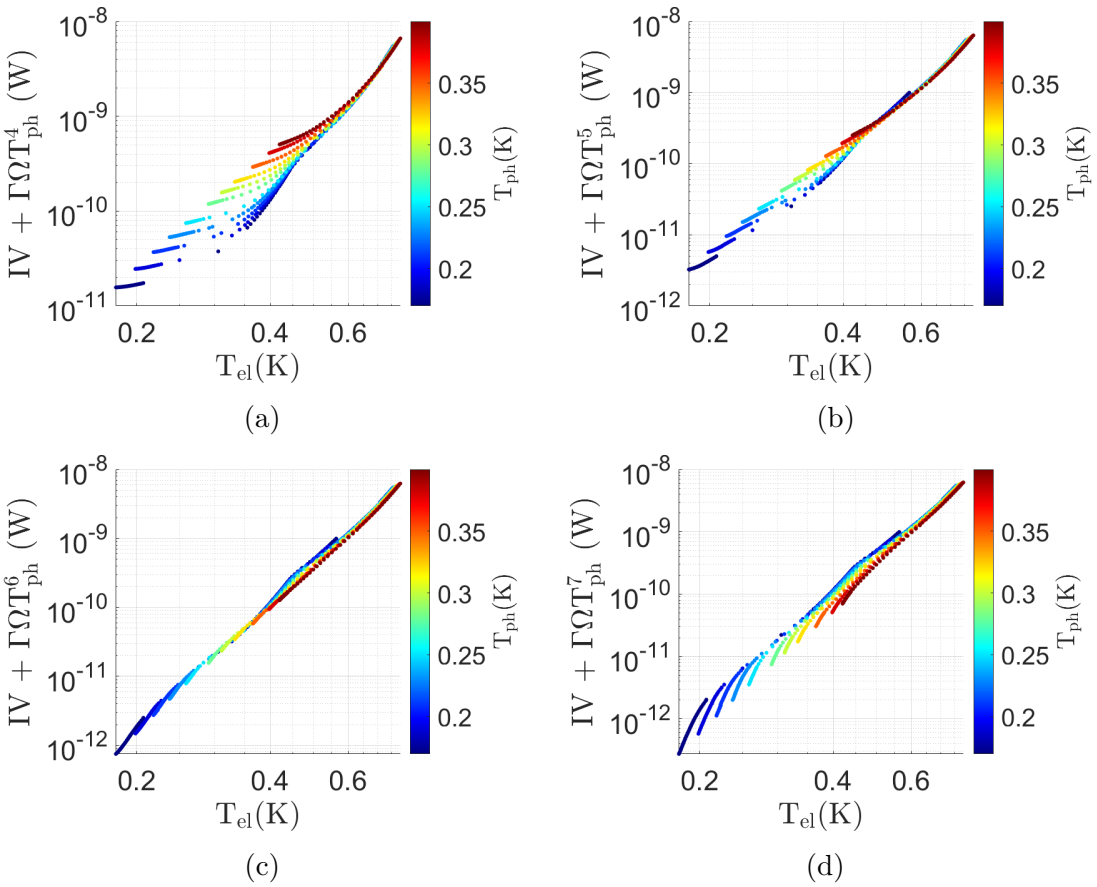

Figure 7.12: $IV + \Gamma\Omega T_{ph}^{\beta}$ against T_{el} for β values of a) 4, b) 5, c) 6, d) 7. If the data fits to (7.6) the data should fall onto a straight line with slope equal to β. This is the case for c). The slope is 5.95 with $\beta = 6$. Note that the data spans the current jumps.

magnetic fields, close to $\nu = 5$. Transport was consistently via Efros-Shklovskii hopping. Both T_{ph}^c and T_0 are plotted against ν in Fig. 7.13a. The value of T_0 can be seen to decrease away from integer filling factor, possibly due to an increasing density of states either side of this point. This is depicted schematically in Fig. 7.1. The ratio of the two temperatures, T_{ph}^c/T_0, alongside the theoretical value of 3.9×10^{-3}, is plotted against ν in Fig. 7.13b. The comparison of the observed values with the predicted value is taken as further verification of the phenomenological electron-phonon decoupling theory.

Finally, current-voltage characteristics can be generated numerically using

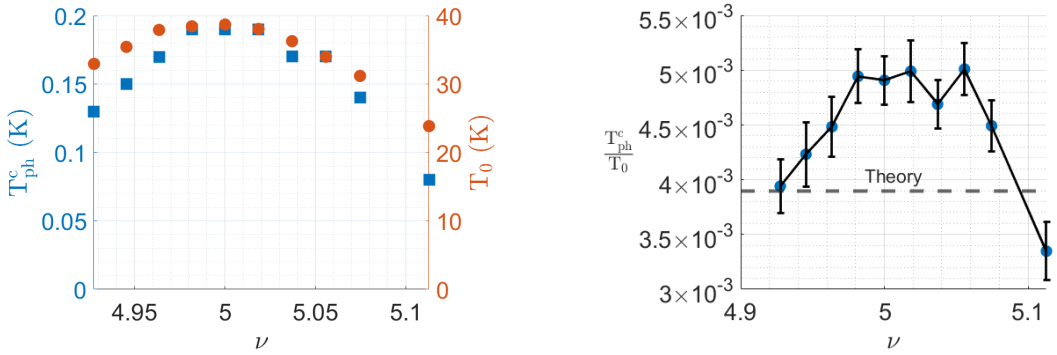

(a) (b)

Figure 7.13: a) Both T^c_{ph} and T_0 plotted against ν. b) T^c_{ph}/T_0 plotted against ν. Using (2.70) with $\gamma = 1/2$ and $\beta = 6$, the theoretical value is 3.9×10^{-3}.

(2.69) and compared with the observed characteristics. The parameters needed are ρ_0, γ, T_0, β and Γ. As previously discussed, the values of ρ_0, γ and T_0 are taken from fittings to the temperature dependence of the ohmic resistivities. The values of β and Γ are taken from the power fittings. Such a numerical characteristic is seen in Fig. 7.14. Here $T_{ph} = 0.9T^c_{ph}$. The downward critical voltage predicted in this plot, $V^c_{\downarrow} = 10$ mV, is in good agreement with the measured values shown in Fig. 7.8.

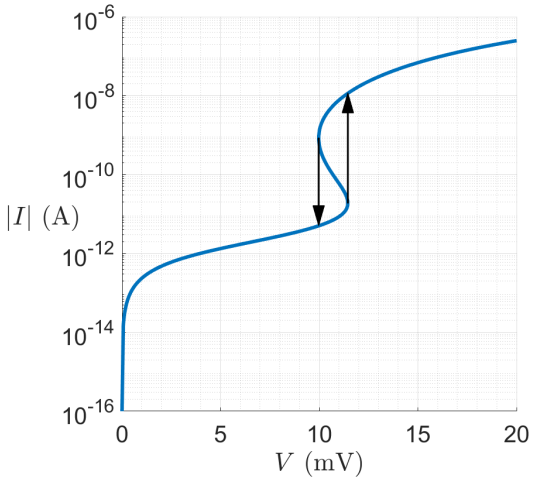

Figure 7.14: Numerically calculated current-voltage characteristic with $T_{ph} = 0.9T^c_{ph}$. The downward critical voltage, $V^c_{\downarrow} = 10$ mV, agrees with the measured values seen in Fig. 7.8.

7.2.3 Filling Factor Three

Current-voltage characteristics at $\nu = 3$ are seen in Fig. 7.15. The bias is swept from negative to positive values in Fig. 7.15a, with the opposite direction being shown in Fig. 7.15b. Jumps of five orders of magnitude in current can be seen as well as clear hysteresis. The bias values associated with downward jumps, $V_{\downarrow}^{c}$, are again seemingly independent of T_{ph}, unlike the values of $V_{\uparrow}^{c}$. Overall, the characteristics are qualitatively similar to those of $\nu = 5$ and those in the literature which have been ascribed to electron-phonon decoupling [21, 22, 81, 83]. Secondary jumps are also present. As is the case with the $\nu = 5$ secondary jumps, this warrants further investigation. If they can be shown to be due to a non-uniform spatial temperature distribution, this would be highly significant with respect to many-body localisation. In the low bias regime with $T_{ph} < T_{ph}^{c}$, the current was generally below the current noise floor. This prevented the detailed analysis which was possible for $\nu = 5$.

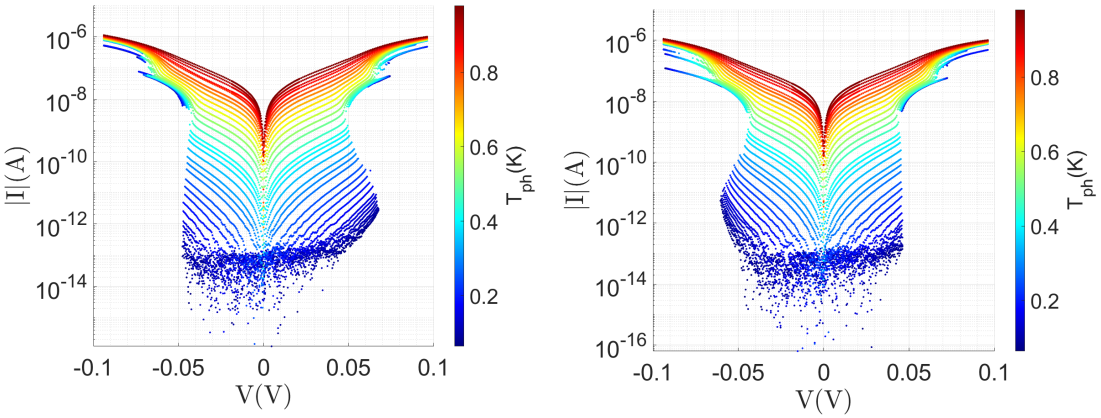

Figure 7.15: Current-voltage characteristics with $\nu = 3$. a) Bias voltage was swept from negative to positive values. Sweeps at different lattice temperatures are shown. b) Bias voltage was swept from positive to negative values. The asymmetry is due to the hysteretic nature of the characteristics.

Chapter 8

Localised Transport in Graphene

In this chapter, results regarding localised transport in focused ion beam (FIB) damaged graphene are presented. The initial aim of this work was to investigate the effect of electron-electron interactions on localised transport. This was to be achieved using a graphene double layer device. Specifically, the device was composed of a layer of monolayer graphene and a layer of trilayer graphene, separated by a thin layer, 66 nm, of hexagonal boron nitride (h-BN). Electrical contacts were fabricated in such a way so that the two layers were electrically isolated. Only the monolayer graphene was FIB damaged. Both a top gate and back gate were fabricated. How the carrier density of the pristine trilayer affected the transport within the damaged monolayer was investigated. The screening layer was chosen to be trilayer, as opposed to monolayer, due to its higher density of states and increased screening ability. As shall be shown, no systematic dependence was found between the trilayer carrier density and the transport within the damaged monolayer. However, an unusual transition between Efros-Shklovskii hopping and Arrhenius transport was observed within the damaged monolayer. Significantly, the Efros-Shklovskii hopping regime was present at lower temperatures than the Arrhenius regime. This is unusual; typically it is variable range hopping, includ-

ing Efros-Shklovskii hopping, that is expected at the lowest temperatures. This is due to larger hops becoming more favourable in order to allow carriers to hop to sites of matching energy. One explanation for this atypical behaviour is that the soft Coulomb gap, necessary for Efros-Shklovskii hopping, hardens. That is, the density of states becomes equal to zero over a range of energies and not just exactly at the Fermi level. This will be discussed in more detail.

8.1 Double Layer Transport in Two-Dimensional Systems

Double layered structures, such as double quantum wells, have historically been of interest due to the possibility of observing novel states as a result of interlayer interactions. Notable examples include indirect excitons, so-named due to the spatial separation of the fermionic components, charge density waves and coupled Wigner crystals [128–131]. Such phenomena, typically, rely upon attractive interlayer interactions meaning one layer is commonly an electron layer and the other a hole layer. However, exciton condensation has been observed in electron-electron double layers and hole-hole double layers with large perpendicular magnetic fields. Such systems are referred to as quantum Hall bilayers [129]. Regardless of carrier types, the interactions between the layers can be probed by means of the Coulomb drag technique. By applying a current, I, through one layer, an open-circuit voltage, V_{drag}, is induced in the second layer. The drag resistance, $R_{\text{drag}} = V_{\text{drag}}/I$, provides an insight into the nature of the interlayer interactions. See [132] for the first experimental demonstration and [133–136] for more recent works.

GaAs/Al_xGa_{1-x}As heterostructures were the first systems used to host such double layers. Specifically, double quantum well heterostructures. When making transport measurements of such structures, one has to be careful to ensure that

the two layers remain electrically isolated; separate electrical contacts to each layer are necessary. One way of achieving this is by using gates to deplete one layer in the vicinity of the contacts used to contact the other layer. Such a device requires both top gates and patterned back gates [135]. In recent years, double layer structures in graphene have become more commonplace [137]. Work has also been carried out in combined GaAs/$Al_xGa_{1-x}As$ and graphene systems [138].

In this work, unlike the high mobility systems discussed here, one layer hosted localised transport. As shall be discussed, disorder was achieved using a focused-ion beam (FIB). The relative ease of only damaging one layer was ultimately the reason a graphene device was chosen over a GaAs/$Al_xGa_{1-x}As$ system.

8.2 Device Fabrication and Basic Characterisation

A schematic depicting the double layer structure is shown in Fig. 8.1. Three layers of insulating hexagonal boron nitride (h-BN) sandwich the two graphene layers. As discussed in section 4.7, the silicon substrate was heavily doped meaning it was essentially metallic and acted as a back gate. The substrate itself had 290 nm of silicon dioxide grown on it which, along with the h-BN, determined the back gate's capacitance. The bottom, middle and top layers of h-BN were 77 nm, 66 nm and 43nm thick respectively. Thicknesses were determined via atomic force microscopy (AFM).

The stacking of the h-BN and graphene flakes was carried out as discussed in section 4.7. The first three layers of the stack are shown in Fig. 8.2a. The image shown was taken midway through the stacking process, before the final graphene flake and final h-BN flake were added. Two flakes of h-BN are seen with the monolayer graphene flake visible between them. For clarity the monolayer

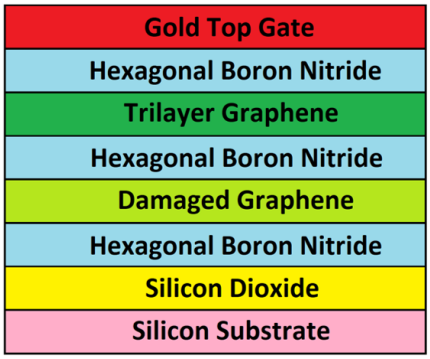

Figure 8.1: Graphene double layer schematic. Three layers of h-BN sandwich a layer of damaged graphene and a layer of pristine trilayer graphene.

graphene flake has been outlined. The region around the graphene where the h-BN flakes overlap is also labelled. Before adding the final graphene flake and h-BN flake, the monolayer graphene was damaged. This was done using a Carl Zeiss Orion NanoFab FIB, using helium ions, as discussd in section 3.3.3. 25 keV ions at a dose of 1 pCμm^{-2} were used. The 10 μm $\times$ 6 μm damaged region can clearly be seen in Fig. 8.2b. This is the same image as Fig. 8.2a, but with a different lookup table (LUT) filter. With this filter the monolayer is harder to see, but the damaged region is now visible.

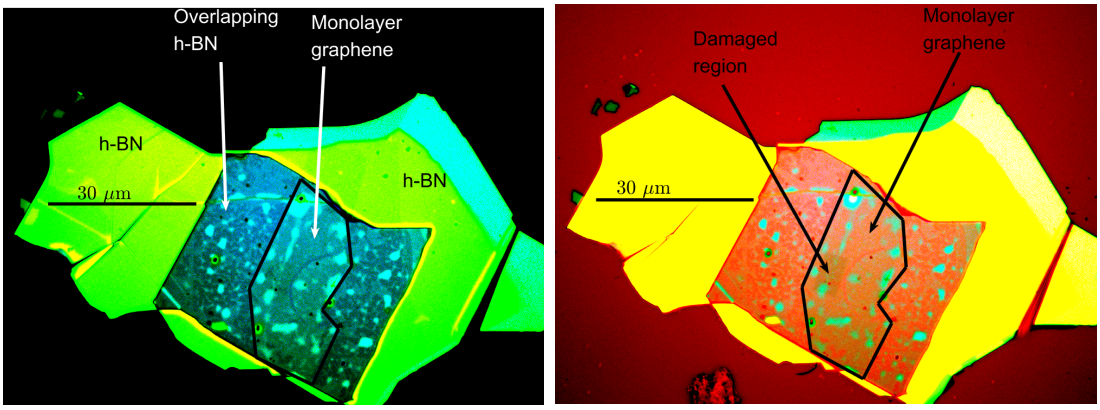

(a) (b)

Figure 8.2: The damaged monolayer graphene flake between two layers of h-BN. Both a) and b) are the same image with different lookup table filters. In a) the monolayer graphene can be seen, whereas in b) the damaged region is visible.

The final stack is shown in Fig. 8.3. The trilayer graphene flake and the final h-BN flake have been outlined for clarity. The damaged region of the monolayer is still visible. In order to create the wanted double layer device, it was essential that the trilayer overlapped this damaged region.

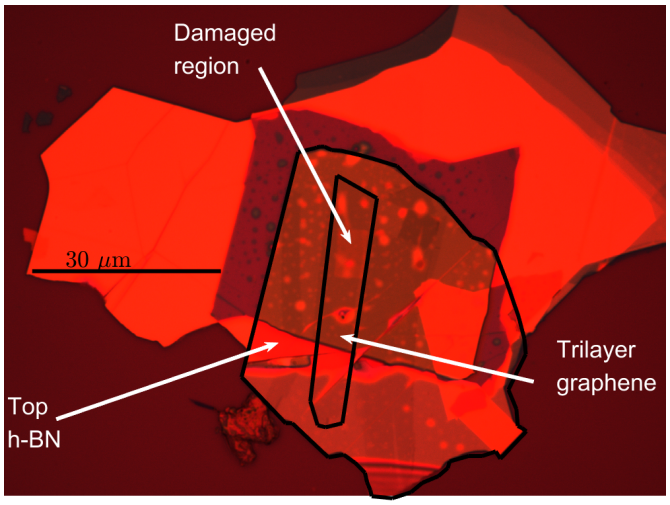

Figure 8.3: The completed stack. The trilayer graphene flake, on top of the monolayer, with h-BN in between can be seen.

Once the stack was complete, five rounds of electron beam lithography were necessary to fabricate the device. The first two were necessary to make contact to the two graphene layers. Each of these rounds involved an etch and a subsequent metal deposition. As discussed in section 4.7, h-BN was dry etched with a sulphur hexaflouride plasma and graphene with an oxygen plasma. Metal deposition of 1 nm of chromium followed by 30 nm of gold was then carried out. This was done immediately after etching, without removing the resist, so that metal was only deposited where the etch had taken place. When forming contacts to the trilayer graphene the first layer of h-BN was etched away, followed by the trilayer. Metal was then deposited into the etched space. As the trilayer within the etched space had been removed, contact was made via the edge of the flake. Thus a one dimensional contact to the trilayer was formed. It was crucial, therefore, that

the sample was placed off-centre in the evaporator and rotated so as to allow the evaporated metal to coat the side wall of the etched space. When making contact to the monolayer, the top two layers of h-BN and both graphene layers were etched away. Again, a one dimensional contact was formed following metal deposition. As well as directly contacting the relevant layers, metal was also deposited around the edges of the stack, so as to form lines which ran out to bonding pads. Importantly this metal was deposited at the same time as the aforementioned contact metal. Thus, due to the etching steps, it was anchored in the stack. Both this anchoring and the 1 nm chromium adhesion layer ensured the deposited metal stayed in place. This anchored metal can be seen in Fig. 8.4. This image was taken following the first two rounds of lithography. In the centre of the stack, the 12 contacts to the two graphene layers can be seen. Those labelled 'M' contact the monolayer, while the other 6 contact the trilayer.

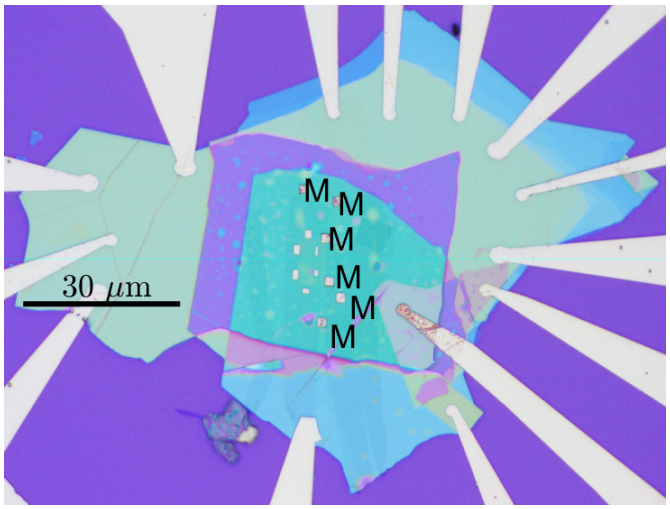

Figure 8.4: The six monolayer and six trilayer contacts can be seen in the centre of the stack. Monolayer contacts are marked by an 'M'. Contacts lines have been anchored into the surrounding h-BN.

The third round of lithography was necessary to link the graphene contacts and the anchored bonding pad lines. In this instance, no etching was necessary. This was just a further metal deposition. The top gate was also deposited at the

same time. The deposition was again 1 nm chromium followed by 30 nm gold. Figure 8.5 shows the stack following this deposition. Contacts to the monolayer, trilayer and gate are labelled 'M', 'T' and 'G' respectively.

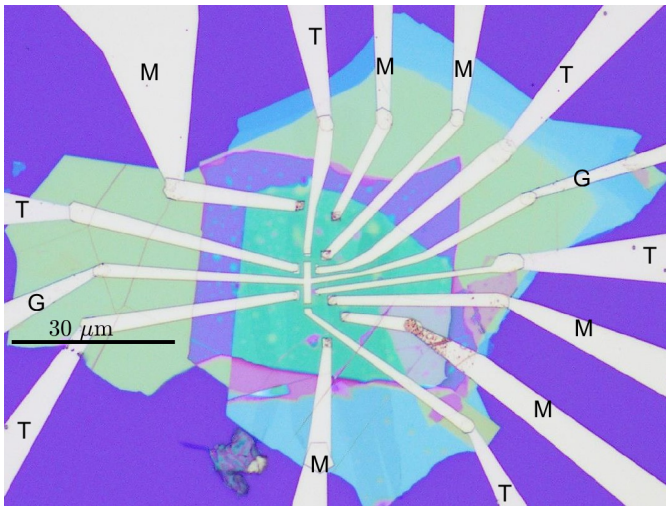

Figure 8.5: The top gate and contact bridges are shown to have been added to the stack. Contacts to the monolayer, trilayer and gate are labelled 'M', 'T' and 'G' respectively.

The final two lithography steps were two further etches. The penultimate etch was used to electrically isolate the monolayer from the trilayer. Only the trilayer was etched. This was necessary as when forming the monolayer contacts it was likely that contact was made to the trilayer too. This was due to the edge of the trilayer being exposed after etching down to the monolayer. The final etch was used to define the Hall bar. Both graphene layers were etched away. Figure 8.6 shows the device just before the final etch, after development of the PMMA resist. The six trilayer etches can be seen. They appear purple and successfully isolated the monolayer from the trilayer. One of these trilayer etches is labelled. The developed PMMA resist for the final Hall bar etch can also be seen. The resist can be seen around the outside of the device. More importantly, it can be seen to protect the paths from the contacts to the Hall bar itself. The gold top gate essentially defined the Hall bar as it is resistant to the etch too. The trilayer

etches make more sense when viewed in the context of the final device. As seen in Fig. 8.6, each of the six trilayer etches prevents shorting of trilayer contact Tx to monolayer contact Mx. The final result was a top gated and back gated Hall bar of dimenions 1.5 μm $\times$ 9 μm.

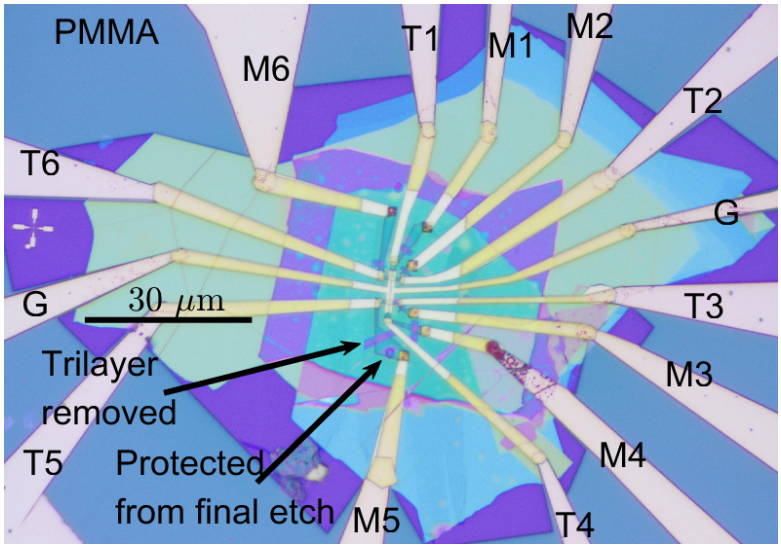

Figure 8.6: The stack before the final etch to define the Hall bar. One of the six trilayer etches to prevent shorting between the monolayer and trilayer is indicated. Each one of these etches prevents shorting of trilayer contact Tx to monolayer contact Mx.

Basic characterisation of the device can be seen in Fig. 8.7. The two terminal resistance of the trilayer graphene against top gate voltage, V_t, at 1.5 K can be seen in Fig. 8.7a. The charge neutrality point of the trilayer can be seen to be at $V_t = 1.6$ V. The two terminal resistance of the damaged monolayer graphene against back gate voltage, V_b, at 90 K can be seen in Fig. 8.7b. The reason for the observed behaviour as the Fermi level is varied within the damaged monolayer graphene is not obvious. Temperature dependences are necessary to determine the mechanism of localised transport. Regardless, Fig. 8.7 shows that device works as intended. Both layers are electrically isolated and each can be measured independently of the other.

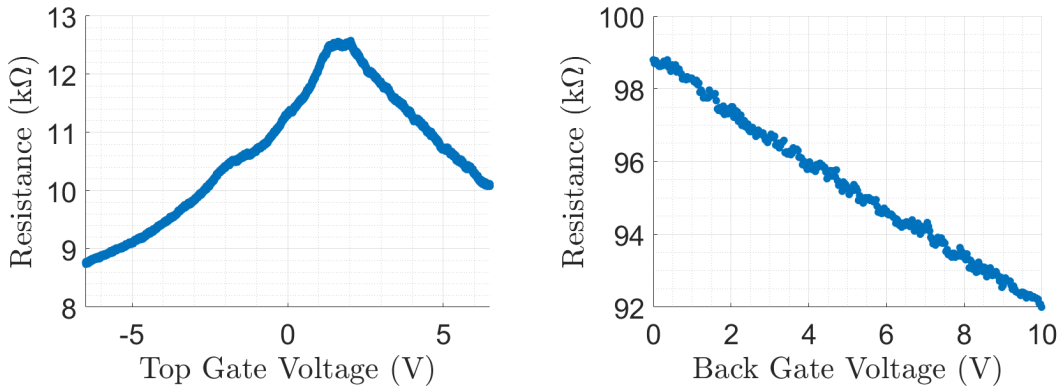

Figure 8.7: a) Trilayer resistance against top gate voltage at 1.5 K, with $V_b = 0$. The measurement was two terminal with contacts T1 and T4 being used, depicted in Fig. 8.6. The charge neutrality point is at 1.6 V. b) The resistance of the damaged monolayer against back gate voltage at 90 K with $V_t = 0$. The measurement was two terminal with contacts M1 and M4 being used.

8.3 Localised Transport Measurements

8.3.1 Arrhenius To Efros-Shklovskii Transition

The resistivity temperature dependence of the damaged monolayer graphene with $V_t = 0$ and $V_b = 0$ is shown in Fig. 8.8. Four terminal AC measurements were made with an excitation voltage of 100 μV at 4 Hz. See Fig. 5.4 for a schematic of the measurement set-up. In Fig. 8.8a the resistivity can be seen to vary by over three orders of magnitude as temperature is varied between 2.5 K and 90 K. It is clear that, post FIB damage, the monolayer graphene has been dramatically altered. The disorder caused by helium ion implantation and carbon vacancies in the graphene lattice has resulted in the material transitioning to an insulator. Fig. 8.8b shows the same data, but with resistivity plotted against T^{-1} on a semi-log scale. Below 10 K, meaning $T^{-1} > 0.1$ K^{-1}, the data falls onto a straight line. This indicates an Arrhenius temperature dependence. That is, $\rho = \rho_0 \exp(T_0/T)$. The straight line fit results in parameters of $T_0 = 15.6$

K and $\rho_0 = 2.3h/e^2$. The same data is also plotted against $T^{-1/2}$ in Fig. 8.8c.

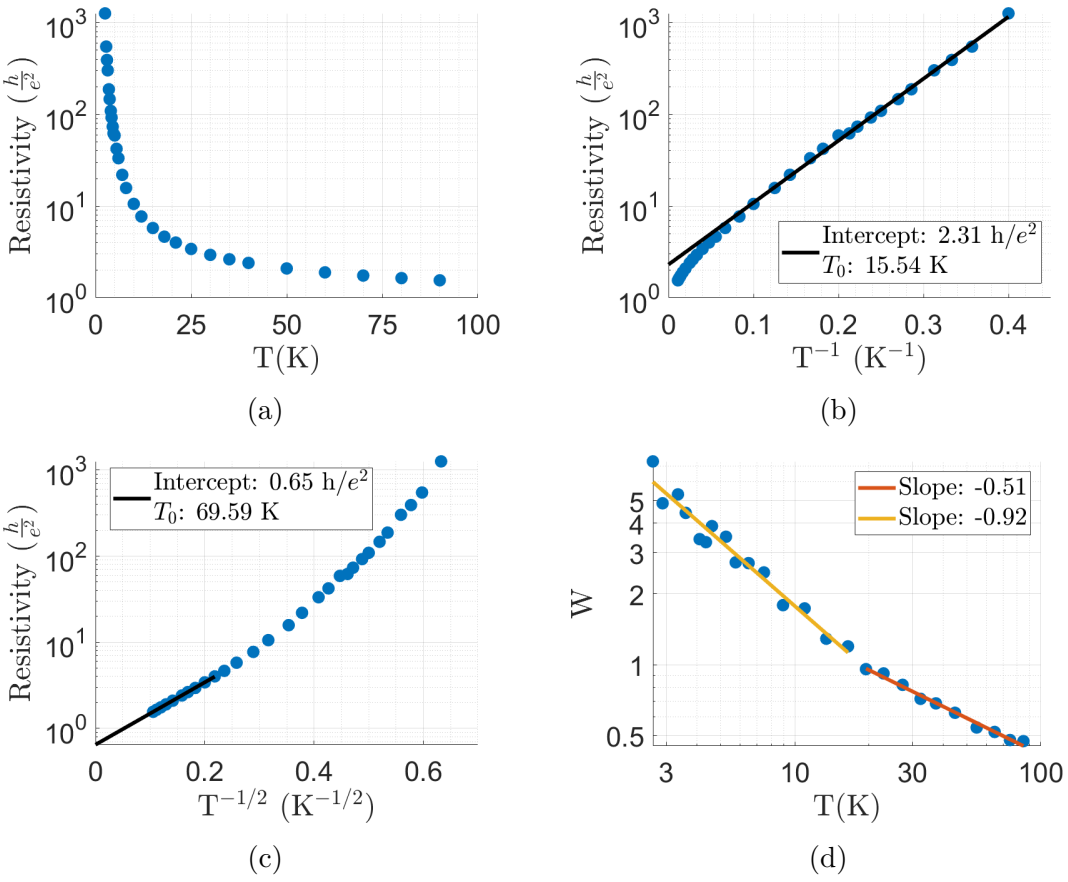

Figure 8.8: Monolayer resistivity temperature dependence with $V_t = 0$ and $V_b = 0$. a) Resistivity against T. b) Resistivity against T^{-1}, with Arrhenius behaviour indicated. c) Resistivity against $T^{-1/2}$, with Efros-Shklovskii hopping indicated. d) $W = -d\log\rho/d\log T$ is plotted against T on a log-log scale. A transition between Arrhenius behaviour and Efros-Shklovskii hopping is evident.

Above 25 K, meaning $T^{-1/2} < 0.2$ $K^{-1/2}$, the data falls onto a straight line. This indicates Efros-Shklovskii hopping. The fitted resistivity temperature dependence is $\rho = \rho_0 \exp\left[(T_0/T)^{1/2}\right]$ with $T_0 = 69.6$ K and $\rho_0 = 0.65h/e^2$. The transition between Arrhenius transport and Efros-Shklovskii hopping is illustrated clearly in Fig. 8.8d. Here, $W = -d\log\rho/d\log T$ is plotted against T on a log-log scale. If $\rho = \rho_0 \exp\left[(T_0/T)^{\gamma}\right]$, the data should fall onto a straight line of slope $-\gamma$. Below 20 K, $\gamma = 0.92$ whilst above 20 K, $\gamma = 0.51$. The conclusion, therefore, is

that there is indeed a transition between Efros-Shklovskii hopping and Arrhenius transport. What is significant is that the Efros-Shklovskii regime occurs at higher temperatures than the Arrhenius regime.

A transition from an Arrhenius transport mechanism, be this nearest neighbour hopping or activation to a mobility edge, to variable range hopping, be this Mott or Efros-Shklovskii, is expected to occur with the Arrhenius transport present at the higher temperatures. See section 2.6 for a discussion and references therein. However, in this work, the opposite has been observed; the results shown in Fig. 8.8 demonstrate an Arrhenius regime occuring at lower temperatures than the Efros-Shklovskii regime. Furthermore, the fitted Arrhenius and Efros-Shklovskii parameters from Fig. 8.8, result in the Arrhenius fit having larger resistances, at all temperatures, than the Efros-Shklovskii fit. If the Efros-Shklovskii hopping coexists with the Arrhenius transport mechanism, the Efros-Shklovskii hopping will always dominate due to its lower resistivity. This clearly is not the case.

8.3.2 Logarithmic Electron-Electron Interaction

A potential explanation for the unusual behaviour presented in section 8.3.1 is that the nature of the Coulomb gap, which itself is necessary for Efros-Shklovskii hopping, is altered. As discussed in section 2.6.4, in two dimensions a density of states of the form $N(E_F + \epsilon) \propto |\epsilon|$ results in standard Efros-Shklovskii hopping. However, with an altered Coulomb interaction, it is conceivable that the form of $N(E)$ can be quite different. In disordered materials, large localisation lengths can lead to large dielectric constants. This is due to the screening ability of electrons which occupy states of large spatial extent [139]. If a material with large dielectric constant is sandwiched between two materials of much lower dielectric constant, the electric field will be strongly confined to the region of large dielectric constant.

The electric field, within this region, will effectively appear two dimensional. The solution to Gauss's law in two dimensions is a logarithmic potential. The electron-electron interaction will therefore be approximately logarithmic in distance,

$$V(r) \approx V_0 \log\Big(\frac{r_0}{r}\Big), \tag{8.1}$$

where V_0 is a characteristic energy and r_0 characterises the length scale. Such an interaction potential can be used to potentially explain ultra-low Arrhenius resistivity temperature dependences. The explanation here is based on analysis given in [74]. See also [140–142]. As discussed in section 2.6.4, if the electron-electron interaction is to have an effect on the density of states, then the distance, r, and energy, ϵ, separating two sites close to the Fermi level, must satisfy $V(r) \approx \epsilon$, meaning

$$V_0 \log\Big(\frac{r_0}{r}\Big) \approx \epsilon. \tag{8.2}$$

In two dimensions, the average distance between sites in an energy interval ϵ around the Fermi level is

$$r \approx \left(\int_{E_F}^{E_F+\epsilon} N(E)dE\right)^{-1/2}, \tag{8.3}$$

Substituting (8.3) into (8.2) leads to,

$$\int_{E_F}^{E_F+\epsilon} N(E)dE \propto \exp(2\epsilon/V_0). \tag{8.4}$$

The density of states is approximately exponential in distance from the Fermi level. This is quite different from the $N(E_F+\epsilon) \propto |\epsilon|$ behaviour observed in two dimensions with a standard Coulomb interaction.

Using (8.2), the equivalent of (2.59) is

$$\Gamma_r = \lambda_0 \exp\left(-\frac{2r}{\xi} - \frac{V_0 \log(r_0/r)}{k_B T} \right). \tag{8.5}$$

This is the rate at which hops occur between sites separated by a distance r. As in section 2.6.3, the conductivity is found by maximising this rate with respect to r and assuming these hops dominate the conductivity. Given the exponential nature of the rate, this is not an unreasonable argument. The optimal hopping distance with the logarithmic electron-electron interaction is

$$r_{\log} = \xi \frac{V_0}{2k_B T}. \tag{8.6}$$

The associated conductivity is

$$\sigma_{\log} = \sigma_0 \exp\left\{ -\frac{V_0}{k_B T} \left[1 + \log\left(\frac{2r_0 k_B T}{\xi V_0} \right) \right] \right\}. \tag{8.7}$$

The conductivity is now close to an Arrhenius form, with a logarithmic correction to the activation temperature. It is possible that this form of conductivity could explain the unusual transition seen in Fig. 8.8. Instead of being due to nearest-neigbour hopping or activation to a mobility edge, the Arrhenius behaviour could be due to a divergence of the dielectric constant and the resultant logarithmic electron-electron interaction. A similar transition has been observed in TiN thin films on the insulating side of a disorder driven superconductor-insulator transition (SIT) [143]. Although the authors noted that the transition defies conventional wisdom, no further comment was made. See also [140, 144, 145] for further examples of ultra-low temperature Arrhenius behaviour.

As discussed, large localisation lengths are often proposed as the reason for low temperature Arrhenius behaviour. However, such low temperature behaviour is

typically observed close to a metal-insulator transition or even a superconductor-insulator transition. It is natural to expect diverging localisation lengths in the vicinity of such a transition. At the point of transition, the localisation length is essentially infinite. Furthermore, and more significantly, the proposed large localisation length theory only explains low temperature Arrhenius behaviour in general; the theory does not explain the unusual transition from Efros-Shklovskii hopping that has been observed in this work. It would appear, for the theory to explain this specific transition, that localisation length should decrease as temperature increases. However, analogous to both weak localisation and the existence of a mobility edge in two dimensions, it is anticipated that an increase in temperature should lead to an increase in localisation length. This is due to inelastic scattering events increasing and quantum coherence therefore decreasing.

Ultimately, the reason for the transition is unclear. Its existence also brings into question whether the low temperature Arrhenius behaviour can be ascribed to a large localisation length and the resultant logarithmic electron-electron interaction. This itself is significant as it indicates a different mechanism of Arrhenius transport that has not been proposed in the literature.

8.3.3 Top Gate Effect

Resistivity temperature dependences were repeated over a range of different top gate voltages, V_t. This was done in order to investigate the effect of a varying trilayer carrier density on the monolayer transport. The transition temperature between Arrhenius and Efros-Shklovskii hopping was not altered by the top gate. The only systematic effect of the top gate was to vary the parameters of the Efros-Shklovskii hopping. In Fig. 8.9 the parameters of both the Arrhenius and Efros-Shklovskii transport are shown against top gate voltage. In the Arrhenius regime, in which $\rho = \rho_0^{Ar} \exp\left(T/T_0^{Ar}\right)$, the values of T_0^{Ar} and ρ_0^{Ar} have no systematic

dependence on top gate voltage. This can be seen in Fig. 8.9a and Fig. 8.9b. In the Efros-Shklovskii regime, in which $\rho = \rho_0^{ES} \exp\left[(T/T_0^{ES})^{1/2}\right]$, both T_0^{ES} and ρ_0^{ES} are dependent on top gate voltage. This is shown in Fig. 8.9c and Fig. 8.9d. However, both parameters vary by only 10% over a 20 V range of the top gate. This corresponds to a change in charge density within the trilayer of 9.8×10^{12} cm^{-2}. Due to the change in screening capability of carriers at the Fermi level in the trilayer, it was anticipated that there may be a significant effect as the the charge neutrality point, seen in Fig. 8.7a at $V_t = 1.6$ V, is passed through. However, this was not the case.

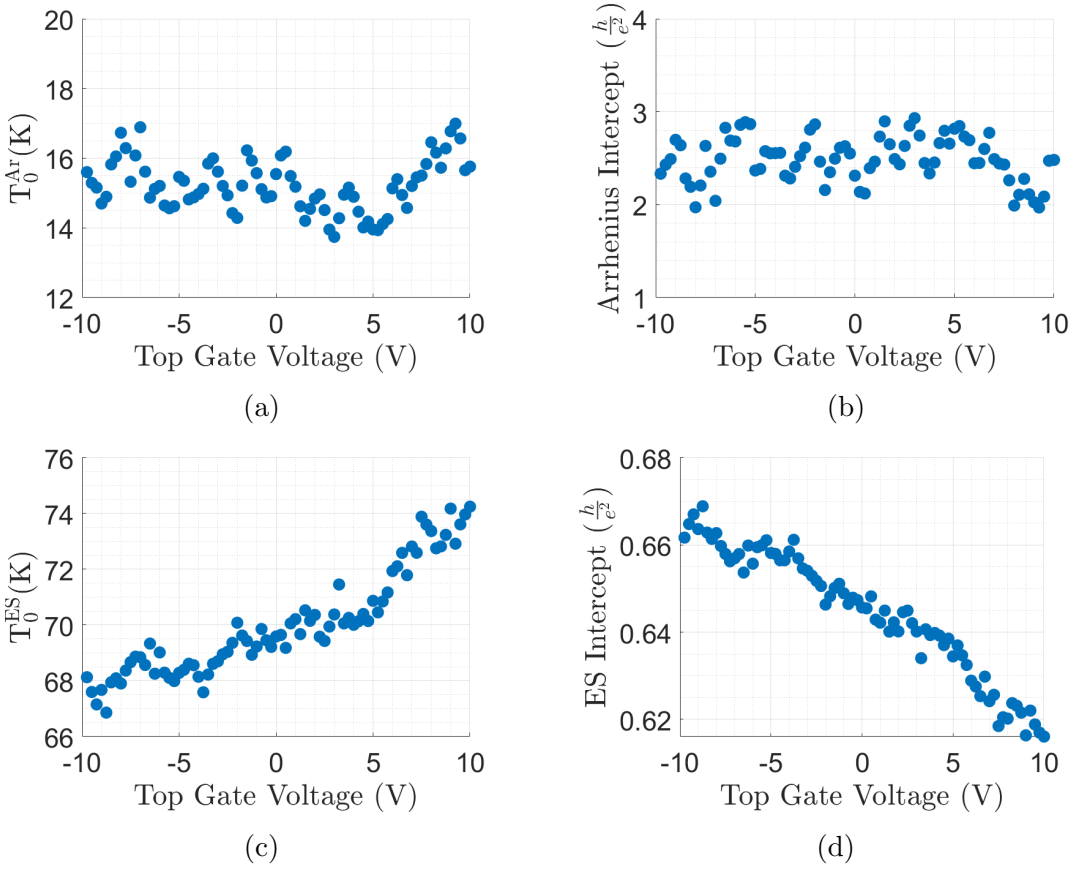

Figure 8.9: Monolayer resistivity fitting parameters taken from fittings shown in Fig. 8.8, plotted against top gate voltage. a) Arrhenius characteristic temperature, T_0^{Ar}. b) Arrhenius infinite temperature intercept, ρ_0^{Ar}. c) Efros-Shklovskii hopping characteristic temperature, T_0^{ES}. d) Efros-Shklovskii infinite temperature intercept, ρ_0^{ES}.

It is possible that the change in Efros-Shklovskii parameters is not due to the change in trilayer carrier density. It could simply be the case that the Fermi level is being altered within the monolayer itself. However it is also not clear why the Arrhenius transport is unaffected.

Chapter 9

Conclusion

9.1 Summary of Results

Results related to three different systems have been presented in this thesis. In all three the Fermi level was engineered to lie beneath a mobility edge. Transport was thus via activation to this mobility edge or via hopping between localised sites.

The first system was a gated GaAs/$Al_xGa_{1-x}As$ two-dimensional electron gas (2DEG). Squares of length 300 μm, suitable for van der Pauw measurements, were studied. The gate was used to deplete the 2DEG and push the Fermi level below the mobility edge. Striking Hall carrier density temperature dependences were observed. For the first time, in the context of electron transport in disordered systems, an Arrhenius Hall carrier density was demonstrated alongside an Arrhenius conductivity. This is the first evidence of its kind which supports a simple activation to mobility edge picture. All other results in the literature display an unexplained activated mobility and an apparent constant carrier density. Furthermore, in this thesis, the mobility is shown to be independent of gate voltage and thus Fermi level. This is in keeping with all transport taking place at the mobil-

ity edge. A transition from carrier density to mobility dominating the resistivity temperature dependence has been demonstrated. It is argued that the unusual results in the literature are all simply on one side of this transition. The ability to observe the transition has been ascribed to how deep it has been possible to probe in the band-tail. The ratio of the density of states to the extended state density of states, N/N_{ext}, was as low as 0.05. Similar investigations in the literature only exhibit $N \approx N_{ext}$.

Using the same device, at lower temperatures, the Hall effect was investigated while the transport mechanism was that of Efros-Shklovskii hopping. The physical picture was less clear compared to the Arrhenius regime. Within the literature there is no accepted model regarding the Hall effect in the hopping regime. The results presented in this thesis do offer some support to theoretical works which propose a Hall mobility of the same temperature dependence as the conductivity, but with a modified characteristic temperature.

Promising initial results were seen using gate-defined 5 μm square devices. The aim was to probe length scale dependence of the activated carrier density. Two gates were used to define the square while the third was used to deplete it. Measurements in the style of a focusing experiment were used to show that the square was defined as intended. Temperature dependent carrier densities were observed. However, contact issues prevented measurements being made as far into the band tail as was possible with the 300 μm devices.

The second system investigated was again hosted in a GaAs/Al_xGa_{1-x}As 2DEG. In this instance, disorder broadened Landau levels were studied. By using a Corbino-eqsue geometry, edge states were avoided and transport was restricted to localised states. By measuring current-voltage characteristics at different lattice temperatures, an electron overheating model was shown to fit well to the breakdown of the quantum Hall effect. The characteristics, which contained cur-

rent jumps of over three orders of magnitude, were shown to be in good agreement with the model. Furthermore, the critical lattice temperatures, below which the hysteretic current jumps occurred, were in good agreement with the theoretical values based on the low bias resistivity temperature dependences. This work is the first in which the breakdown of the quantum Hall effect is successfully compared to the discussed overheating model. The mechanism of transport was Efros-Shklovskii hopping. This itself is notable as observing current jumps due to overheating has been predicted as being difficult in such a regime [22]. Furthermore, this is the first instance of current jumps being reported in a system which displays Efros-Shklovskii hopping.

The third system was a graphene double layer device. The first layer was monolayer graphene, damaged using a helium focused ion beam (FIB). The second was pristine trilayer graphene. The fabrication itself was novel as it involved an FIB exposure midway through the stacking process. The initial aim was to investigate the effects of electron-electron interactions on localised transport. This was to be done by varying the carrier density within the trilayer while observing the behaviour of the transport within the damaged monolayer. No systematic effect was found. Instead, however, an unusual transition from an Arrhenius resistivity temperature dependence to an Efros-Shklovskii hopping regime was observed. Crucially, the Arrhenius regime occurred at the lowest temperatures. It is expected that variable range hopping, including Efros-Shklovskii hopping, will occur at lower temperatures than standard Arrhenius transport mechanisms such as nearest neighbour hopping and activation to a mobility edge. It is unlikely that the Arrhenius regime is due to large localisation lengths and a large resultant dielectric constant. This is a popular explanation for ultra-low temperature Arrhenius behaviour. It is possible that the behaviour requires an explanation not discussed in the literature.

9.2 Future Work

With respect to the activated carrier density work, arguably the most pressing unanswered issue is that of the mobility temperature dependence. That the mobility is independent of Fermi level is striking and indicates that all transport is taking place at the mobility edge. It also indicates that the edge lifetime is greater than the elastic scattering time at the edge, the latter therefore being the relevant lifetime with respect to determining mobility. However, why the mobility increases with temperature is not clear. How mobility varies with magnetic field should be measured. This will provide insight as to whether the temperature dependence is related to weak localisation. Measuring magnetic field dependences will also allow the determination of the phase coherence length. Due to the high resistances and resultant small signals that must be measured, measurements at just a single magnetic field value took a significant amount of time. Sweeping magnetic field and making accurate measurements at such resistances will be challenging, but still possible. To improve the 5 μm square work, the contacts which bridge the high mobility material and depleted central square must be improved. This should allow measurements to be made further into the band tail than is currently possible with the current 5 μm devices.

Future work regarding the breakdown of the quantum Hall effect should attempt to fit current jumps at even filling factors to the overheating model. Such jumps, with $\nu = 4$, can be seen in [103]. However, their temperature dependence was not studied. In work presented in this thesis, power-law resistivity temperature dependences at such filling factors meant that current jumps were not present in current-voltage characteristics. For completeness, material displaying these jumps should be studied. Furthermore, the secondary jumps should be further investigated. It has been suggested in this work that they could be due to

a non-uniform spatial distribution of electron temperature. This would be highly relevant to the study of many-body localisation. Measuring devices of different sizes may provide further insight. Assuming a non-uniform temperature distribution, larger devices would be expected to have more areas that resist the initial heating associated with the primary jump. It would therefore be expected that larger devices exhibit either more secondary jumps, larger secondary jumps or both. Finally, standard Corbino devices should be used. The devices in this work were used as they allowed for parallel conduction to be tested via Shubnikov-de Haas oscillations. However, this was purely for efficiency of measurements and to prevent multiple devices having to be measured.

With regard to the graphene double layer work, the Arrhenius transport regime requires further investigation. Currently, the transport mechanism is unknown. How resistance varies with magnetic field should be studied. The Hall effect may also be worthwhile measuring. More devices should be fabricated, each having a different separation between the two layers. The separation should be less than that in the device studied in this work, as the effect of interlayer interactions was deemed negligible. This should allow for a study of electron-electron interactions and their effect on localised transport. This study may also assist in the determination of the transport mechanism of the low temperature Arrhenius regime.

Appendix A

The Propagator

When considering enhanced backscattering in time reversal symmetric systems, a central quantity to consider is the probability amplitude of an electron moving from position $\mathbf{r}_0$ to $\mathbf{r}_{end}$ in time t. This is known as the propagator,

$$A(\mathbf{r}_0, \mathbf{r}_{end}, t) = \langle \mathbf{r}_{end} | \, e^{-i\hat{H}t} \, | \mathbf{r}_0 \rangle \, . \tag{A.1}$$

Inserting identity operators, $\sum_\alpha |\mathbf{r}_\alpha\rangle \langle \mathbf{r}_\alpha|$, leads to

$$A(\mathbf{r}_0, \mathbf{r}_{end}, t) = \sum_{\alpha,\beta,...\gamma} \langle \mathbf{r}_{end} | \, e^{-i\hat{H}\Delta} \, | \mathbf{r}_\gamma \rangle \langle \mathbf{r}_\gamma | \, e^{-i\hat{H}\Delta} ... \, | \mathbf{r}_\beta \rangle \langle \mathbf{r}_\beta | \, e^{-i\hat{H}\Delta} \, | \mathbf{r}_\alpha \rangle \langle \mathbf{r}_\alpha | \, e^{-i\hat{H}\Delta} \, | \mathbf{r}_0 \rangle \, . \tag{A.2}$$

Here N identity operators have been inserted while also splitting up $e^{-i\hat{H}t}$ into $N+1$ operators $e^{-i\hat{H}\Delta}$, where $\Delta = \frac{t}{N+1}$. Each term in the sum represents the probability amplitude of the particle taking the path $\mathbf{r}_0 \to \mathbf{r}_\alpha \to \mathbf{r}_\beta \to ... \to \mathbf{r}_\gamma \to \mathbf{r}_{end}$. By taking a large limit of N, the sum can be made to be over every possible path the electron can take. To find the probability that the particle moves from $\mathbf{r}_0$ to $\mathbf{r}_{end}$ in time t, the probability amplitudes for each path are summed and then the square of the magnitude is taken. When considering back scattering, an

important quantity is the probability amplitude of a particle starting at $\mathbf{r}_0$ also being at $\mathbf{r}_0$ after time t, $A(\mathbf{r}_0, \mathbf{r}_0, t)$. The probability amplitude of one possible path which contributes to $A(\mathbf{r}_0, \mathbf{r}_0, t)$ is,

$$\langle \mathbf{r}_0 | \, e^{-i\hat{H}\Delta} \, | \mathbf{r}_N \rangle \, \langle \mathbf{r}_N | \, e^{-i\hat{H}\Delta} ... \, | \mathbf{r}_2 \rangle \, \langle \mathbf{r}_2 | \, e^{-i\hat{H}\Delta} \, | \mathbf{r}_1 \rangle \, \langle \mathbf{r}_1 | \, e^{-i\hat{H}\Delta} \, | \mathbf{r}_0 \rangle \, .$$

The path here is $\mathbf{r}_0 \to \mathbf{r}_1 \to \mathbf{r}_2 \to ... \to \mathbf{r}_N \to \mathbf{r}_0$. The time evolution operator $e^{-i\hat{H}\Delta}$ can be expressed as $\sum_n |n\rangle \langle n| \, e^{-iE_n\Delta}$ where the sum is over eigenstates of $\hat{H}$. The amplitude can thus be written as,

$$\sum_{\substack{n,m... \\ ...k,l}} e^{-i(E_n+E_m+...+E_k+E_l)\Delta} \, \langle \mathbf{r}_0 | n \rangle \, \langle n | \mathbf{r}_N \rangle \, \langle \mathbf{r}_N | m \rangle \, \langle m | \, ... \, | \mathbf{r}_2 \rangle \, \langle \mathbf{r}_2 | k \rangle \, \langle k | \mathbf{r}_1 \rangle \, \langle \mathbf{r}_1 | l \rangle \, \langle l | \mathbf{r}_0 \rangle \, .$$

Replacing $\langle \mathbf{r} | \mathbf{n} \rangle$ with $\psi_n(\mathbf{r})$ this can be expressed as

$$\sum_{\substack{n,m... \\ ...k,l}} e^{-i(E_n+E_m+...+E_k+E_l)\Delta} \psi_n(\mathbf{r}_0) \psi_n^*(\mathbf{r}_N) \psi_m(\mathbf{r}_N) ... \psi_k(\mathbf{r}_2) \psi_k^*(\mathbf{r}_1) \psi_l(\mathbf{r}_1) \psi_l^*(\mathbf{r}_0).$$

The probability amplitude of the same path but in the opposite direction is,

$$\sum_{\substack{n,m... \\ ...k,l}} e^{-i(E_n+E_m+...+E_k+E_l)\Delta} \psi_l(\mathbf{r}_0) \psi_l^*(\mathbf{r}_1) \psi_k(\mathbf{r}_1) \psi_k^*(\mathbf{r}_2) ... \psi_m^*(\mathbf{r}_N) \psi_n^*(\mathbf{r}_N) \psi_n(\mathbf{r}_0).$$

Note that the dummy indices are free to be reordered, which has been done. Recall from the discussion regarding time-reversal symmetry that if $\psi_n(\mathbf{r})$ is the wavefunction associated with an eigenstate of $\hat{H}$ then so is $\psi_n^*(\mathbf{r})$, with both having the same energy. Thus it can be seen that the probability amplitudes for the two paths are equal. They will add coherently. Hence the overall probability amplitude for the particle returning to its initial position is formed of pairs of paths which have the same amplitude and, most importantly, same phase.

Appendix B

Landauer Formula

The Landauer formula relates the conductance, G, of a sample to the number of transverse modes, M [39]. In an ideal one-dimensional system, $M = 1$, when conductance is considered along the length of the ideal wire. In any given sample, M is simply equal to the number of transverse subbands which have an energy minimum below the Fermi level. Consider the conductance of such a sample in the x direction. An applied voltage is taken into account by shifting the local chemical potentials on either side of the sample. The difference in chemical potential between the two contacts is simply eV, where V is the applied voltage. This difference in local chemical potential results in one contact injecting more electrons than the other. Initially it shall be assumed that all injected electrons travel ballistically. The current due to a single, ballistic transverse mode is

$$I = \frac{e}{L_x} \sum v_x. \tag{B.1}$$

Here the sum is over all states within the energy gap between the local chemical potentials on opposite sides of the sample. It is these states that are responsible for the net current. Note that zero temperature has been assumed. The velocity

component and sample dimensions in the x direction are v_x and L_x respectively. The velocity term can be rewritten as $v_x = (1/\hbar)\partial E/\partial k_x$. The sum can also be replaced by an integral over k_x. This is done by using that the separation between states in k_x space is $2\pi/L_x$ and including a factor of 2 for spin. This results in

$$I = e \int \frac{1}{\hbar\pi} \frac{\partial E}{\partial k_x} dk_x. \tag{B.2}$$

Again the integration is over states within the energy gap between the chemical potentials of the contacts. Integrating over these limits results in $\int (\partial E/\partial k_x) dk_x = eV$. This leads to

$$I = \frac{2e^2}{h} V. \tag{B.3}$$

If, instead of assuming ballistic transport, the probability of transmission via any given mode is T, the total current due to M modes will simply be,

$$I = \frac{2e^2}{h} MTV. \tag{B.4}$$

This results in the Landauer formula for the conductance

$$G = \frac{2e^2}{h} MT. \tag{B.5}$$

Appendix C

Hopping Conductivity and Percolation Theory

Percolation theory can be used to derive the conductivity temperature dependence in the variable range hopping regime. In this section argurments from [69] are used. The analysis does not rely on any particular mechanism to facilitate the hops and is thus applicable to any inelastic scattering mechanism. It is assumed that states are localised at the Fermi level.

Let $\lambda_{ij}(R_{ij}, E_i - E_j)$ be the intrinsic hopping rate between sites i and j which have energies relative to the Fermi level of E_i and E_j respectively and are separated by a distance R_{ij}. The hopping rate from i to j is thus

$$\Gamma_{ij} = n_i(1 - n_j)\lambda_{ij}, \tag{C.1}$$

where n_i is the Fermi function for site i. Therefore,

$$\Gamma_{ij} = \frac{1}{1 + e^{E_i/k_BT}} \frac{e^{E_j/k_BT}}{1 + e^{E_j/k_BT}} \lambda_{ij}. \tag{C.2}$$

In equilibrium it is required that $\Gamma_{ij} = \Gamma_{ji}$, which leads to the detailed balance

equation

$$\lambda_{ij} e^{E_j/k_B T} = \lambda_{ji} e^{E_i/k_B T}. \tag{C.3}$$

Using this detailed balance it is asserted that,

$$\lambda_{ij} = \begin{cases} \lambda_0 e^{-2\alpha R_{ij} - (E_j - E_i)/k_B T} & \text{for} \quad E_j > E_i \\ \lambda_0 e^{-2\alpha R_{ij}} & \text{for} \quad E_i > E_j. \end{cases} \tag{C.4}$$

There are various ways of satisfying the detailed balance equation (C.3), but this particular solution has been chosen for the following reasons. The R_{ij} dependence is related to the overlap of the localised states which themselves decay exponentially with rate $\alpha = 1/\xi$, where ξ is localisation length. It is then assumed that $k_B T << |E_i - E_j|$. Thus if the state i is occupied, state j is not and $E_i > E_j$ a temperature independent transition from i to j is expected. Using this reasoning, C.4 follows. If it is assumed that $k_B T$ is much less than all energies involved it holds that,

$$\Gamma_{ij} = \lambda_0 \exp\left(-2\alpha R_{ij} - \frac{|E_i| + |E_j| + |E_i - E_j|}{2 k_B T} \right). \tag{C.5}$$

The system is now taken out of equilibrium by adding an electric field. The intrinsic hopping changes such that,

$$\lambda \left[\mathbf{E}(\mathbf{r}) \right]_{ij} = \lambda_{ij} + \Delta(\lambda_{ij}), \tag{C.6}$$

where $\mathbf{E}(\mathbf{r})$ is the applied electric field. Let $\Delta\mu_i$ be the change in chemical potential at site i. The change in Γ_{ij}, using (C.1), is

$$\Delta(\Gamma_{ij}) = \Gamma_{ij}^0 \left[\frac{\Delta(\lambda_{ij})}{\lambda_{ij}} + \frac{\Delta(n_i)}{n_i} - \frac{\Delta(n_j)}{1 - n_j} \right], \tag{C.7}$$

where Γ_{ij}^0 is the value of Γ_{ij} in equilibrium. This leads to the net current between

site i and j being,

$$e\left[\Delta(\Gamma_{ij}) - \Delta(\Gamma_{ji})\right] = e\Gamma_{ij}^{0}\left[\frac{\Delta(\lambda_{ij})}{\lambda_{ij}} - \frac{\Delta(\lambda_{ji})}{\lambda_{ji}} + \frac{\Delta(n_i)}{n_i(1-n_i)} - \frac{\Delta(n_j)}{n_j(1-n_j)}\right] \quad \text{(C.8)}$$

Using (C.3),

$$\frac{\Delta(\lambda_{ij})}{\lambda_{ij}} - \frac{\Delta(\lambda_{ji})}{\lambda_{ji}} = \frac{\Delta(\lambda_{ji}e^{(E_i-E_j)/k_BT})}{\lambda_{ji}e^{(E_i-E_j)/k_BT}} - \frac{\Delta(\lambda_{ji})}{\lambda_{ji}} = \frac{\Delta(e^{(E_i-E_j)/k_BT})}{e^{(E_i-E_j)/k_BT}}. \quad \text{(C.9)}$$

By applying the electric field, $E_i - E_j$ changes by $e\mathbf{E}\cdot R_{ij}$. Thus,

$$\frac{\Delta(\lambda_{ij})}{\lambda_{ij}} - \frac{\Delta(\lambda_{ji})}{\lambda_{ji}} = \frac{e\mathbf{E}\cdot R_{ij}}{k_BT} \quad \text{(C.10)}$$

The change in local chemical potential is responsible for $\Delta(n_i)$. It follows that,

$$\frac{\Delta(n_i)}{n_i(1-n_i)} - \frac{\Delta(n_j)}{n_j(1-n_j)} = \frac{1}{k_BT}\left[\Delta(\mu_i) - \Delta(\mu_j)\right]. \quad \text{(C.11)}$$

Thus the current between site i and j can be expressed as,

$$I_{ij} = e\left[\Delta(\Gamma_{ij}) - \Delta(\Gamma_{ji})\right] = \frac{e}{k_BT}\Gamma_{ij}^{0}\left[eE\cdot R_{ij} + \Delta(\mu_i) - \Delta(\mu_j)\right]. \quad \text{(C.12)}$$

As $eE\cdot R_{ij} + \Delta(\mu_i) - \Delta(\mu_j)$ is just the potential difference between the two sites multiplied by e, the effective conductance between the two sites is

$$G_{ij} = \frac{e^2}{k_BT}\Gamma_{ij}^{0}. \quad \text{(C.13)}$$

Knowing the conductance between any given pair of sites, the conductance of the sample as a whole is wanted. This is essentially a resistor network problem now. The critical conductance, G_c, is defined as being the smallest conductance such that when only resistors with $G_{ij} > G_c$ are considered, the network is still fully

connected. This network is the critical network. It can be argued that as the resistors vary in magnitude significantly, such a critical resistance will be close to the resistance of the whole sample. The problem now becomes a percolation problem. For a link between i and j to be part of this critical network it is required that, using C.5,

$$2\alpha R_{ij} + \frac{|E_i| + |E_j| + |E_i - E_j|}{2k_B T} < \log(\lambda_0/\Gamma_c), \tag{C.14}$$

where $\Gamma_c = k_B T G_c/e^2$. Setting

$$R_{max} = \frac{1}{2\alpha}\log(\lambda_0/\Gamma_c) \tag{C.15}$$

and

$$E_{max} = k_B T \log(\lambda_0/\Gamma_c), \tag{C.16}$$

it follows that

$$\frac{R_{ij}}{R_{max}} + \frac{|E_i| + |E_j| + |E_i - E_j|}{2E_{max}} < 1 \tag{C.17}$$

Thus, for the link between i and j to be part of the critical network, it must hold that $R_{ij} < R_{max}$, $|E_i| < E_{max}$ and $|E_j| < E_{max}$. The total number of sites matching the energy criteria, per unit volume is,

$$n = 2NE_{max} \tag{C.18}$$

where N is the density of states per unit volume and is assumed constant. These states are randomly distributed in space. In order for the critical network to span the entire sample, it is required that R_{max} is large enough so that nR_{max}^d, where d is dimension, is order unity. In this way each node of the critical network is connected to approximately one other node and the network will be fully connected

as required. Thus it follows that,

$$R_{max}^{d} n \approx 1 \tag{C.19}$$

which results in

$$2N R_{max}^{d} E_{max} \approx 1. \tag{C.20}$$

This leads to

$$R_{max}^{d} \propto \frac{1}{E_{max}}. \tag{C.21}$$

Using (C.15) and (C.16), it follows that

$$[\log(\lambda_0/\Gamma_c)]^d \propto \frac{1}{T \log(\lambda_0/\Gamma_c)} \tag{C.22}$$

Hence, as $\Gamma_c \propto G_c$,

$$G_c \propto \exp\left[-(T_0/T)^{\frac{1}{d+1}}\right]. \tag{C.23}$$

As the critical conductance is anticipated to be close to the conductance of the sample as a whole, it follows that

$$\sigma \propto \exp\left[-(T_0/T)^{\frac{1}{d+1}}\right]. \tag{C.24}$$

This is the expected temperature dependence of variable range hopping.

Appendix D

The Fractional Quantum Hall Effect

In 1982 a quantised Hall resistance of $3h/e^2$ and a local minimum of longitudinal resistance was observed at filling fraction $\nu = 1/3$ [146]. This was the first observation of the fractional quantum Hall effect, which applies to interacting electrons in a magnetic field. Laughlin [147] presented an ansatz for a many-body ground state wavefunction applicable for filling factors $\nu = 1/m$, where m is an odd integer,

$$\psi_m^{Laughlin}(z_1, z_2, ...z_N) \propto \prod_{i<j}(z_i - z_j)^m \prod_k \exp\left(-\frac{|z_k|^2}{4l_B^2}\right), \tag{D.1}$$

where $z = x + iy$ and $l_B = \sqrt{\hbar/eB}$. He claimed that it was consistent with the experimental results. This wavefunction is very similar to the exact solution for a system of non-interacting electrons in a magnetic field, the system discussed in section 2.8.2,

$$\psi_m^{IQHE}(z_1, z_2, ...z_N) \propto \prod_{i<j}(z_i - z_j) \prod_k \exp\left(-\frac{|z_k|^2}{4l_B^2}\right). \tag{D.2}$$

Note that this could have been derived in section 2.8.2, but Cartesian coordinates were chosen. All that Laughlin did was raise each $z_i - z_j$ term in the first product to the power of m. Note that as m is odd the many-body wavefunction remains antisymmetric, as is required for a system of fermions. As this is the only change, it is easy to appreciate that its effect is to push electrons further away from each other. The zeros in the wavefunction are emphasised. One way of interpreting this new wave function is to consider the effective phase change as one electron circles around another. The phase changes within the Laughlin wave function are as if each electron has had $m - 1$ flux quanta added to it, this combined entity is known as a composite fermion [148]. The effective magnetic field that each composite fermion experiences is,

$$B_{eff} = B - \frac{nh(m-1)}{e}, \tag{D.3}$$

if it is asserted that the composite fermion flux opposes the actual magnetic field. At filling factor $\nu = 1/m$ the effective filling factor of the composite fermions is,

$$\nu_{eff} = \frac{nh}{B_{eff}e} = \frac{1}{\frac{1}{\nu} - (m-1)} = 1. \tag{D.4}$$

The conclusion, therefore, is that at filling fraction $1/m$, where m is odd, there is a filled Landau level of composite fermions. Analogous arguments to those used in section 2.8.2 can be used to show that this leads to a quantised Hall resistance of mh/e^2, as observed for $m = 3$ in [146].

To observe the fractional quantum Hall effect less disorder is necessary, compared to the integer quantum Hall effect. Reduced disorder increases the significance of the electron-electron interactions and strengthens the fractional effect. Many more fractions have been observed since the initial discovery of the 1/3

state in [146]. Fractions do not have to be of the form $1/m$. Commonly observed fractions include 2/5 and 3/7, here one can consider forming composite fermion Landau levels with filling factors 2 and 3 respectively.

At filling factor 1/2, one can consider forming composite fermions by adding two flux quanta to each electon. If again it is asserted that this flux opposes the magnetic field, the effective magnetic field becomes zero. Hence at filling factor 1/2 there exists a Fermi sea of composite fermions. It is expected, therefore, that the longitudinal resistance of the system should be symmetric in field either side of this filling fraction. This is experimentally observed.

Finally, note that there is much interest in the 5/2 fractional state. Interestingly, this state has an even denominator and thus cannot be explained by traditional composite fermion theory. It has been suggested that the quasiparticles in this state form a p-wave superconductor and could thus host non-abelian anyons [149, 150]. Anyons are particles that have fractional values of exchange phase and can only exist in two dimensions. The non-abelian aspect means that the state of the system is dependent on the order of braiding operations and that each exchange leads to an observable change of state. States can thus be topologically protected as one must physically exchange particles to change the state of the system. This is of interest in the field of quantum computing, in order to limit decoherence.

Bibliography

[1] P. W. Anderson. Absence of diffusion in certain random lattices. *Phys. Rev.*, 109(5):1492, 1958.

[2] T. Schwartz, G. Bartal, S. Fishman, and M. Segev. Transport and Anderson localization in disordered two-dimensional photonic lattices. *Nature*, 446:52, 2007.

[3] Y. Lahini, A. Avidan, F. Pozzi, M. Sorel, R. Morandotti, D. N. Christodoulides, and Y. Silberberg. Anderson localization and nonlinearity in one-dimensional disordered photonic lattices. *Phys. Rev. Lett.*, 100(1):013906, 2008.

[4] J. Billy, V. Josse, Z. Zuo, A. Bernard, B. Hambrecht, P. Lugan, D. Clement, L. Sanchez-Palencia, P. Bouyer, and A. Aspect. Direct observation of Anderson localization of matter waves in a controlled disorder. *Nature*, 453:891, 2008.

[5] G. Roati1, C. D'Errico, L. Fallani1, M. Fattori, C. Fort, M. Zaccanti, M. Modugno G. Modugno1, 2, and M. Inguscio. Anderson localization of a non-interacting Bose–Einstein condensate. *Nature*, 453:895, 2008.

[6] R.L. Weaver. Anderson localization of ultrasound. *Wave Motion*, 12(2):129, 1990.

[7] G. Feher and E. A. Gere. Electron spin resonance experiments on donors in silicon. II. Electron spin relaxation effects. *Phys. Rev.*, 114(5):1245, 1959.

[8] E. Abrahams, P. W. Anderson, D. C. Licciardello, and T. V. Ramakrishnan. Scaling theory of localization: Absence of quantum diffusion in two dimensions. *Phys. Rev. Lett.*, 42(10):673, 1979.

[9] N. F. Mott. Conduction in glasses containing transition metal ions. *Journal of Non-Crystalline Solids*, 1(1):1, 1968.

[10] N. F. Mott. The mobility edge since 1967. *J. Phys. C: Solid State Phys.*, 20(21):3075, 1987.

[11] S. I. Khondaker, I. S. Shlimak, J. T. Nicholls, M. Pepper, and D. A. Ritchie. Two-dimensional hopping conductivity in a δ-doped GaAs/Al_xGa_{1-x}As heterostructure. *Phys. Rev. B*, 59(7):4580, 1999.

[12] A. Ghosh, M. Pepper, D. A. Ritchie, E. H. Linfield, R. H. Harrell, H. E. Beere, and G. A. C. Jones. Electron assisted variable range hopping in strongly correlated 2D electron systems. *Phys. Stat. Sol. B*, 230(1):211, 2002.

[13] E. Arnold. Disorder-induced carrier localization in silicon surface inversion layers. *Appl. Phys. Lett.*, 25(12):705, 1974.

[14] J. P. Thompson. Hall effect measurements on silicon inversion layers. *Phys. Lett.*, 66(1):65, 1978.

[15] F. F. Fang and A. B. Fowler. Transport properties of electrons in inverted silicon surfaces. *Phys. Rev.*, 169(3):619, 1968.

[16] Y. Gul, M. Myronov, S.N. Holmes, and M. Pepper. Activated and metallic conduction in p-type modulation-doped Ge-Sn devices. *Phys. Rev. Applied*, 14(5):054064, 2020.

[17] D. M. Basko, I. L. Aleiner, and B. L. Altshuler. Metal–insulator transition in a weakly interacting many-electron system with localized single-particle states. *Ann. Phys*, 321(5):1126, 2006.

[18] M. Schreiber, S. S. Hodgman, P. Bordia, H. P. Luschen, M. H. Fischer, R. Vosk, U. Schneider E. Altman, and I. Bloch. Observation of many-body localization of interacting fermions in a quasirandom optical lattice. *Science*, 349(6250):842, 2015.

[19] H. P. Lüschen, P. Bordia, S. S. Hodgman, M. Schreiber, S. Sarkar, A. J. Daley, M. H. Fischer, E. Altman, I. Bloch, and U. Schneider. Signatures of many-body localization in a controlled open quantum system. *Phys. Rev. X*, 7(1):011034, 2017.

[20] D. M. Basko, I. L. Aleiner, and B. L. Altshuler. Possible experimental manifestations of the many-body localization. *Phys. Rev. B*, 76(5):52203, 2007.

[21] B. L. Altshuler, V. E. Kravtsov, I. V. Lerner, and I. L. Aleiner. Jumps in current-voltage characteristics in disordered films. *Phys. Rev. Lett.*, 102(17):176803, 2009.

[22] G. McArdle and I.V. Lerner. Electron-phonon decoupling in two dimensions. *Sci. Rep.*, 11(1):24293, 2021.

[23] G. Nachtwei. Breakdown of the quantum Hall effect. *Physica E*, 4(2):79, 1999.

[24] K. v. Klitzing, G. Dorda, and M. Pepper. New method for high-accuracy determination of the fine-structure constant based on quantized Hall resistance. *Phys. Rev. Lett.*, 45(6):494, 1980.

[25] Y. Gul, S. N. Holmes, C. Cho, B. Piot, M. Myronov, and M. Pepper. Two-dimensional localization in GeSn. *J. Phys.: Condens. Matter*, 34(48):485301, 2022.

[26] M. Pepper, S. Pollitt, and C J Adkins. The spatial extent of localized state wavefunctions in silicon inversion layers. *J. Phys. C: Solid State Phys.*, 7(15), 1974.

[27] R. M. Hill. Variable range hopping. *Phys. Stat. Sol. A*, 34(2):601, 1976.

[28] M. Rudra, H.S. Tripathi, A. Dutta, and T.P. Sinha. Existence of nearest-neighbor and variable range hopping in Pr_2ZnMnO_6 oxygen-intercalated pseudocapacitor electrode. *Mat. Chem. Phys.*, 258:123907, 2021.

[29] F. Bloch. Über die quantenmechanik der elektronen in kristallgittern. *Zeitschrift fur Physik*, 52:555, 1929.

[30] S. Das Sarma and F. Stern. Single-particle relaxation time versus scattering time in an impure electron gas. *Phys. Rev. B*, 32(12):8442, 1985.

[31] A. F. Ioffe and A. R. Regel. *Progress in Semiconductors edited by A. F. Gibson*. Wiley, 1960.

[32] N. F. Mott. *Metal-Insulator Transitions*. Taylor and Francis, 1990.

[33] A. Fick. Ueber diffusion. *Annalen der Physik*, 170(1):59, 1855.

[34] P. Drude. Zur elektronentheorie der metalle. *Annalen der Physik*, 306(3):566, 1900.

[35] C. Kittel. *Introduction to Solid State Physics 8th Edition.* Wiley, 2018.

[36] B. L. Altshuler, D. Khmel'nitzkii, A. I. Larkin, and P. A. Lee. Magnetoresistance and Hall effect in a disordered two-dimensional electron gas. *Phys. Rev. B*, 22(11):5142, 1980.

[37] A. Stern, Y. Aharonov, and Y. Imry. Phase uncertainty and loss of interference: A general picture. *Phys. Rev. A*, 41(7):3436, 1990.

[38] S. Datta. *Electronic Transport in Mesoscopic Systems.* Cambridge University Press, 1995.

[39] R. Landauer. Spatial variation of currents and fields due to localized scatterers in metallic conduction. *IBM J. Res. Dev.*, 1(3):223, 1957.

[40] M. Cahay, M. McLennan, and S. Datta. Conductance of an array of elastic scatterers: A scattering-matrix approach. *Phys. Rev. B*, 37(17):10125, 1988.

[41] P. A. Lee and A. Douglass Stone. Universal conductance fluctuations in metals. *Phys. Rev. Lett.*, 55(15):1622, 1985.

[42] M.E. Gershenson. Low-temperature dephasing in disordered conductors: experimental aspects. *Ann. Phys.*, 511(7):539, 1999.

[43] S. Hikami, A. I. Larkin, and Y. Nagaoka. Spin-orbit interaction and magnetoresistance in the two dimensional random system. *Prog. Theor. Phys.*, 63(2):707, 1980.

[44] D. A. Poole, M. Pepper, and A. Hughes. Spin-orbit coupling and weak localisation in the 2D inversion layer of indium phosphide. *J. Phys. C: Solid State Phys.*, 15(32):1137, 1982.

[45] G. Bergman. Influence of spin-orbit coupling on weak localization. *Phys. Rev. Lett.*, 48(15):1046, 1982.

[46] P. A. Lee and T. V. Ramakrishnan. Disordered electronic systems. *Rev. Mod. Phys.*, 57(2):287, 1985.

[47] Y. Aharonov and D. Bohm. Significance of electromagnetic potentials in the quantum theory. *Phys. Rev. 115*, 115(3):485, 1959.

[48] A. Tonomura, N. Osakabe, T. Matsuda, T. Kawasaki, J. Endo, S. Yano, and H. Yamada. Evidence for Aharonov-Bohm effect with magnetic field completely shielded from electron wave. *Phys. Rev. Lett.*, 56(8):792, 1986.

[49] B. L. Altshuler, A. G. Aronov, and B. Z. Spivak. The Aronov-Bohm effect in disordered conductors. *JETP Lett*, 33(2):94, 1981.

[50] K. Aihara, M. Yamamoto, K. I. K. Iwadate, and T. M. T. Mizutani. Temperature dependence of the phase coherence length of high-mobility algaas/gaas quantum-wire rings. *Jpn. J. Appl. Phys. 30 L1627*, (9), 1991.

[51] K. K. Choi, D. C. Tsui, and K. Alavi. Dephasing time and one-dimensional localization of two-dimensional electrons in GaAs/Al_xGa_{1-x}As heterostructures. *Phys. Rev. B*, 36(14):7751, 1987.

[52] T. J. Thornton, M. Pepper, H. Ahmed, D. Andrews, and G. J. Davies. One-dimensional conduction in the 2d electron gas of a GaAs-Al_xGa_{1-x}As heterojunction. *Phys. Rev. Lett.*, 56(11):1198, 1986.

[53] R. A. Webb and S. Washburn. Quantum interference fluctuations in disordered metals. *Physics Today*, 41(12):46, 1988.

[54] J. H. de Boer and E. J. W. Verwey. Semi-conductors with partially and with completely filled 3d-lattice bands. *Proc. Phys. Soc.*, 49(4):59, 1937.

[55] N. F. Mott. The basis of the electron theory of metals, with special reference to the transition metals. *Proc. Phys. Soc. A*, 62(7):416, 1949.

[56] J. Hubbard. Electron correlations in narrow energy bands. *Proc. Roy. Soc A.*, 276(1365):238, 1963.

[57] R. Abou-Chacra, D. J. Thouless, and P. W. Anderson. A self consistent theory of localization. *J. Phys. C: Solid State Phys.*, 6(10):1734, 1973.

[58] N. F. Mott. Electrons in disordered structures. *Adv. Phys.*, 16(61):49, 1967.

[59] I. M. Lifshitz. The energy spectrum of disordered systems. *Adv. Phys.*, 13(52):483, 1964.

[60] M. Di Stasio and X. Zotos. Connection between low energy effective Hamiltonians and energy level statistics. *Phys. Rev. Lett.*, 74(11):2050, 1995.

[61] E. Teller. The crossing of potential surfaces. *J. Phys. Chem.*, 41(1):1, 1937.

[62] N. C. Murphy, R. Wortis, and W. A. Atkinson. Generalized inverse participation ratio as a possible measure of localization for interacting systems. *Phys. Rev. B*, 18(83):184206, 2011.

[63] D. J. Thouless. Maximum metallic resistance in thin wires. *Phys. Rev. Lett.*, 39(18):1167, 1977.

[64] R. A. Davies, M. Pepper, and M. Kaveh. An experimental test of the scaling theory of conduction in two dimensions. *J. Phys. C: Solid State Phys.*, 16(10):285, 1983.

[65] D. J. Thouless. The effect of inelastic electron scattering on the conductivity of very thin wires. *Solid State Communications*, 34(8):683, 1980.

[66] T. Ando, A. B. Fowler, and F. Stern. Electronic properties of two-dimensional systems. *Rev. Mod. Phys.*, 54(2):437, 1984.

[67] C. J. Adkins. Threshold conduction in inversion layers. *J. Phys. C: Solid State Phys.*, 11(5):851, 1978.

[68] A. Miller and E. Abrahams. Impurity conduction at low concentration. *Phys. Rev.*, 120(3):745, 1960.

[69] V. Ambegaokar, B. I. Halperin, and J. S. Langer. Hopping conductivity in disordered systems. *Phys. Rev. B*, 4(8):2612, 1971.

[70] A. Yildiz, N. Serin, T. Serin, and M. Kasap. Crossover from nearest-neighbor hopping conduction to efros–shklovskii variable-range hopping conduction in hydrogenated amorphous silicon films. *Jpn. J. Appl. Phys.*, (11), 2009.

[71] D. N. Tsigankov and A. L. Efros. Variable range hopping in two-dimensional systems of interacting electrons. *Phys. Rev. Lett.*, 88(17):176602, 2002.

[72] E. L. Efros and B. I. Shklovskii. Coulomb gap and low temperature conductivity of disordered systems. *J. Phys. C: Solid State Phys.*, 8(4):49, 1975.

[73] M. Pollak. Effect of carrier-carrier interactions on some transport properties in disordered semiconductors. *Discuss. Faraday Soc.*, 50:13, 1970.

[74] M. Pollak, M. Ortuño, and A. Frydman. *The electron glass*. Cambridge University Press, 2012.

[75] B. I. Shklovskii and A. L. Efros. *Electronic Properties of Doped Semiconductors*. Springer, 1984.

[76] D. A. Abanin, E. Altman, I. Bloch, and M. Serbyn. Colloquium: Many-body localization, thermalization, and entanglement. *Rev. Mod. Phys.*, 91(2):021001, 2019.

[77] F. Alet and N. Laflorencie. Many-body localization: An introduction and selected topics. *C. R. Physique*, 19(6):498, 2018.

[78] M. Srednicki. Chaos and quantum thermahzation. *Phys. Rev. E*, 50(2):888, 1994.

[79] J. M. Deutsch. Quantum statistical mechanics in a closed system. *Phys. Rev. A*, 43(4):2046, 1991.

[80] M. Srednicki. The approach to thermal equilibrium in quantized chaotic systems. *J. Phys. A: Math. Gen.*, 32(7):1163, 1999.

[81] M. Ovadia, B. Sacépé, and D. Shahar. Electron-phonon decoupling in disordered insulators. *Phys. Rev. Lett.*, 102(17):176802, 2009.

[82] M. Ovadia, D. Kalok, I. Tamir, S. Mitra, B. Sacépé, and D. Shahar. Evidence for a finite-temperature insulator. *Sci. Rep.*, 5(1):13503, 2015.

[83] G. Sambandamurthy, L. W. Engel, A. Johansso, E. Peled, and D. Shahar. Experimental evidence for a collective insulating state in two-dimensional superconductors. *Phys. Rev. Lett.*, 94(1):017003, 2005.

[84] M. V. Fistul, V. M. Vinokur, and T. I. Baturina. Collective cooper-pair transport in the insulating state of josephson-junction arrays. *Phys. Rev. Lett.*, 100(8):086805, 2008.

[85] V. M. Vinokur, T. I. Baturina, M. V. Fistul, A. Yu. Mironov, M. R. Baklanov, and C. Strunk. Superinsulator and quantum synchronization. *Nature*, 452:613–615, 2008.

[86] E. H. Hall. On a new action of the magnet on electric currents. *American Journal of Mathematics*, 2(3):287, 1879.

[87] T. Holstein. Hall effect in impurity conduction. *Phys. Rev.*, 124(5):1329, 1961.

[88] M. Gruenewald, H. Mueller, P. Thomas, and D. Wuertz. The hopping Hall mobility - a percolation approach. *Solid State Commun.*, 38(11):1011, 1981.

[89] A. V. Shumilin and N. P. Stepina. Hall effect in two-dimensional systems with hopping transport and strong disorder. *Phys. Rev. B*, 98(11):115303, 2018.

[90] R. Rudenko, O. Voitsihovska, A. Abakumov, I. Bychko, O. Selyshchev, D. R. T. Zahn, and V. Poroshin. The hopping Hall effect in reduced graphene oxide. *Mater. Lett.*, 326:132932, 2022.

[91] A. Avdonin, P. Skupiński, and K. Grasza. Hall effect in hopping regime. *Phys. B*, 483:13, 2016.

[92] Y. Gal'perin, E. German, and V. Karpov. Hall effect under hopping conduction conditions. *Sov. Phys. JETP*, 72(1):193, 1991.

[93] Y. B. Poyarkov, V. Y. Kontarev, I. P. Krylov, and Y. V. Sharvin. Observation of quantum oscillations of the magnetoresistance of multiply connected objects with a hopping conductivity. *JETP*, 44(6):373, 1986.

[94] H. T. Yi, Y. N. Gartstein, and V. Podzorov. Charge carrier coherence and Hall effect in organic semiconductors. *Sci. Rep.*, 6(23650), 2016.

[95] R. B. Laughlin. Quantized Hall conductivity in two dimensions. *Phys. Rev. B*, 23(10):5632, 1981.

[96] K. Yoshihiro, J. Kinoshita, K. Inagaki, C. Yamanouchi, J. Moriyama, and S. Kawaji. High precision measurements of the Hall effect for silicon MOS inversion layers in strong magnetic fields. *Surface Science*, 113:16, 1982.

[97] G. Ebert, K. von Klitzing, K. Ploog, and G. Weimann. Two-dimensional magneto-quantum transport on GaAs-$Al_xGa_{1-x}As$ heterostructures under non-ohmic conditions. *J. Phys. C.*, 16:5441, 1983.

[98] M.E. Cage, R.F. Dziuba, B.F. Field, E.R. Williams, S.M. Girvin, A.C. Gossard, D.C. Tsui, and R.J. Wagner. Dissipation and dynamic nonlinear behavior in the quantum Hall regime. *Phys. Rev. Lett.*, 51(15):1374, 1983.

[99] L. Bliek, E. Braun, G. Hein, V. Kose, J. Niemeyer, G. Weimann, and W Schlapp. Critical current density for the dissipationless quantum Hall effect. *Semicond. Sci. Technol.*, 1(2):110, 1986.

[100] C. Chen, S. N. Holmes, I. Farrer, H. E. Beere, and D. A. Ritchie. Suspended two-dimensional electron gases in $In_{0.75}Ga_{0.25}As$ quantum wells. *Appl. Phys. Lett.*, 116(23):232106, 2020.

[101] P. Streda and K. v. Klitzing. Critical non-dissipative current of quantum Hall regime. *J. Phys. C: Solid State Phys.*, 17(19):483, 1984.

[102] L. Eaves F.W. Sheard. Size-dependent quantised breakdown of the dissipationless quantum Hall effect in narrow channels. *Semicond. Sci. Technol.*, 1(6):346, 1986.

[103] M. Yokoi, T. Okamoto, S. Kawaji, T. Goto, and T. Fukase. Breakdown of the integer quantum Hall effect studied by Corbino discs. *Physica B*, 249:93, 1998.

[104] K. Chida, T. Hata, T. Arakawa, S. Matsuo, Y. Nishihara, T. Tanaka, T. Ono, and K. Kobayashi. Avalanche electron bunching in a Corbino disk in the quantum Hall effect breakdown regime. *Phys. Rev. B*, 89:235318, 2014.

[105] S. Komiyama, T. Takamasu, S. Hiyamizu, and S. Sasa. Effect of finite electric field on the quantum Hall effect. *Surface Science*, 170:202, 1986.

[106] S. Komiyama, T. Takamasu, S. Hiyamizu, and S. Sasa. Breakdown of the quantum Hall effect due to electron heating. *Solid State Com.*, 54(6):479, 1985.

[107] J. S. Blakemore. Semiconducting and other major properties of gallium arsenide. *J. Appl. Phys.*, 53(10):123, 1982.

[108] J. Davies. *The Physics of Low-dimensional Semiconductors*. Cambridge University Press, 1997.

[109] M. Rother. Aquila (1.4.0.0), 2009. `https://mathworks.com/matlabcentral/fileexchange/3344-2d-schroedinger-poisson-solver-aquila`.

[110] K. S. Novoselov, A. K. Geim, S. V. Morozov, D. Jiang, S. V. Dubonos I. V. Grigorieva Y. Zhang, and A. A. Firsov. Electric field effect in atomically thin carbon films. *Science*, 306(5696):666, 2004.

[111] C. Lee, X. Wei, J. W. Kysar, and J. Hone. Measurement of the elastic properties and intrinsic strength of monolayer graphene. *Science*, 321(5887):385, 2008.

[112] K. Cao, S. Feng, Y. Han, L. Gao, T. H. Ly, Z. Xu, and Y. Lu. Elastic straining of free-standing monolayer graphene. *Nat. Commun.*, 11:284, 2020.

[113] A. S. Mayorov, R. V. Gorbachev, S. V. Morozov, L. Britnell, R. Jalil, L. A. Ponomarenko, P. Blake, K. S. Novoselov, K. Watanabe, T. Taniguchi, and A. K. Geim. Micrometer-scale ballistic transport in encapsulated grapheneat room temperature. *Nano. Lett.*, 11(6):2396, 2011.

[114] A. A. Balandin. Thermal properties of graphene and nanostructured carbon materials. *Nat. Mater.*, 2011.

[115] K. S. Novoselov, V. I. Fal'ko, L. Colombo, P. R. Gellert, M. G. Schwab, and K . Kim. A roadmap for graphene. *Nature*, 490:192, 2012.

[116] A. H. Castro Neto, F. Guinea, N. M. R. Peres, K. S. Novoselov, and A. K. Geim. The electronic properties of graphene. *Rev. Mod. Phys.*, 81(1):109, 2009.

[117] P. R. Wallace. The band theory of graphite. *Phys. Rev.*, 71(9):622, 1947.

[118] M. J. Molaei, M. Younas, and M. Rezakazemi. A comprehensive review on recent advances in two-dimensional(2D) hexagonal boron nitride. *ACS Appl. Electron. Mater.*, 3(12):5165, 2021.

[119] S. Iida and K. Ito. Selective etching of gallium arsenide crystals in H_2SO_4-H_2O_2-H_2O system. *J. Electrochem. Soc.*, 118(5):768, 1971.

[120] Pyvisa (1.12.0), 2022. `https://pypi.org/project/PyVISA/`.

[121] L. J. van der Pauw. A method of measuring specific resistivity and Hall effect of discs of arbitrary shape. *Philips Research Reports*, 13(1):1, 1958.

[122] S. Pollitt, M. Pepper, and C.J. Adkins. The Anderson transition in silicon inversion layers. *Surf. Sci.*, 58(1):79, 1976.

[123] R. Tycko, S. E. Barrett, G. Dabbagh, L. N. Pfeiffer, and K. W. West. Electronic states in gallium arsenide quantum wells probed by optically pumped NMR. *Science*, 268(5216):1460, 1995.

[124] C. I. Duruöz, R. M. Clarke, C. M. Marcus, and J. S. Harris. Conduction threshold, switching, and hysteresis in quantum dot arrays. *Phys. Rev. Lett.*, 74(16):3237, 1995.

[125] S. Kasirer and Y. Meir. Hysteresis and jumps in the I-V curves of disordered two-dimensional materials. *Phys. Rev. B*, 105(13):134508, 2022.

[126] N. Hemsworth, F. Mahvash, P. L. Lévesque, M. Siaj, R. Martel, and T. Szkopek. Measurement of electronic heat dissipation in highly disordered graphene. *Phys. Rev. B.*, 92(24):241411, 2015.

[127] A. Savin, J. Pekola, M. Prunnila, J. Ahopelto, and P. Kivinen. Electronic cooling and hot electron effects in heavily doped silicon-on-insulator film. *Phys. Scr.*, 114:57, 2004.

[128] Y. E. Lozovik and V. I. Yudson. A new mechanism for superconductivity: pairing between spatially separated electrons and holes. *Sov. Phys. JETP*, 2(44):389, 1976.

[129] J. P. Eisenstein and A. H. MacDonald. Bose–einstein condensation of excitons in bilayer electron systems. *Nature*, 432:691, 2004.

[130] L. Swierkowski, D. Neilson, and J. Szymanski. Enhancement of wigner crystallization in multiple-quantum-well structures. *Phys. Rev. Lett.*, 67(2):240, 1991.

[131] S. De Palo, F. Rapisarda, and G. Senatore. Excitonic condensation in a symmetric electron-hole bilayer. *Phys. Rev. Lett.*, 88(20):206401, 2002.

[132] T. J. Gramila, J. P. Eisenstein, A. H. MacDonald, L. N. Pfeiffer, and K. W. West. Mutual friction between parallel two-dimensional electron systems. *Phys. Rev. Lett.*, 66(9):1216, 1991.

[133] J. A. Seamons, D. R. Tibbetts, J. L. Reno, and M. P. Lilly. Undoped electron-hole bilayers in a GaAs/AlGaAs double quantum well. *Appl. Phys. Lett.*, 90(5):052103, 2007.

[134] A. F. Croxall, K. Das Gupta, C. A. Nicoll, M. Thangaraj, H. E. Beere, I. Farrer, D. A. Ritchie, and M. Pepper. Anomalous Coulomb drag in electron-hole bilayers. *Phys. Rev. Lett.*, 101(24):246801, 2008.

[135] B. Zheng, A. F. Croxall, J. Waldie, K. Das Gupta, F. Sfigakis, I. Farrer, H. E. Beere, and D. A. Ritchie. Switching between attractive and repulsive Coulomb-interaction-mediated drag in an ambipolar gaas/algaas bilayer device. *Appl. Phys. Lett.*, 108(6):062102, 2016.

[136] U. S. de Cumis, Joanna Waldie, A. F. Croxall, D. Taneja, J. Llandro, I. Farrer, H. E. Beere, and D. A. Ritchie. A complete laboratory for transport studies of electron-hole interactions in GaAs/AlGaAs ambipolar bilayers. *Appl. Phys. Lett.*, 110(7):072105, 2017.

[137] S. Kim and E. Tutuc. Coulomb drag and magnetotransport in graphene double layers. *Solid State Commun.*, 152(15):1283, 2012.

[138] P. Simonet, S. Hennel, H. Overweg, R. Steinacher, M. Eich, R. Pisoni, Y. Lee, P. Märki, T. Ihn, K. Ensslin, M. Beck, and J. Faist. Anomalous Coulomb drag between bilayer graphene and a GaAs electron gas. *New J. Phys.*, 19:103042, 2017.

[139] H. F. Hess, K. DeConde, T. F. Rosenbaum, and G. A. Thomas. Giant dielectric constants at the approach to the insulator-metal transition. *Phys. Rev. B*, 25(8):5578, 1982.

[140] V. Humbert, M. Ortuño, A. M. Somoza, L. Bergé, L. Dumoulin, and C. A. Marrache-Kikuchi. Overactivated transport in the localized phase of the superconductor-insulator transition. *Nat. Commun.*, 12:6733, 2021.

[141] B. I. Shklovskii. Variable range hopping in thin film with large dielectric constant. *Low Temp. Phys.*, 43(6):699, 2017.

[142] A. I. Larkin and D. E. Khmelnitskii. Activation conductivity in disordered systems with large localization length. *Sov. Phys. JETP*, 56(3):647, 1982.

[143] T. I. Baturina, A. Yu. Mironov, V. M. Vinokur, M. R. Baklanov, and C. Strunk. Localized superconductivity in the quantum-critical region of the disorder-driven superconductor-insulator transition in TiN thin films. *Phys. Rev. Lett.*, 99(25):257003, 2007.

[144] G. Sambandamurthy, L.W. Engel, A. Johansson, and D. Shahar. Superconductivity-related insulating behavior. *Phys. Rev. Lett.*, 92(10):107005, 2004.

[145] T. I. Baturina, A. Yu. Mironov, V. M. Vinokur, M. R. Baklanov, and C. Strunk. Hyperactivated resistance in TiN films on the insulating side of the disorder-driven superconductor-insulator transition. *JETP Lett.*, 88(11):752, 2008.

[146] D. C. Tsui, H. L. Stormer, and A. C. Gossard. Two-dimensional magnetotransport in the extreme quantum limit. *Phys. Rev. Lett.*, 48(22):1559, 1982.

[147] R. B. Laughlin. Anomalous quantum Hall effect: An incompressible quantum fluid with fractionally charged excitations. *Phys. Rev. Lett.*, 50(18):1395, 1983.

[148] J. K. Jain. Theory of the fractional quantum Hall effect. *Phys. Rev. B*, 41(11):7653, 1990.

[149] G. Moore and N. Read. Nonabelions in the fractional quantum Hall effect. *Nuclear Phys. B*, 360(2):362, 1991.

[150] A. Y. Kitaev. Unpaired majorana fermions in quantum wires. *Phys. Usp.*, 44(10):131, 2001.